Modelling of sympathetic Doppler cooling and analysis of probe field induced ac-Stark shifts in an $^{115}In^{+}$ optical clock

Masterarbeit

Moritz von Boehn

Modelling of sympathetic Doppler cooling and analysis of probe field induced ac-Stark shifts in an $^{115}In^{+}$ optical clock

Der Fakultät für Mathematik und Physik der
Gottfried Wilhelm Leibniz Universität Hannover
zur Erlangung des akademischen Grades

Master of Science (M. Sc.) Physik

vorgelegte Masterarbeit
von

Moritz von Boehn

Erstprüferin: Prof. Dr. rer. nat. Tanja E. Mehlstäubler
Zweitprüfer: Prof. Dr. rer. nat. Piet O. Schmidt

Eidesstattliche Erklärung

Hiermit versichere ich, die vorliegende Abschlussarbeit selbstständig und nur unter Verwendung der von mir angegebenen Quellen und Hilfsmittel verfasst zu haben. Sowohl inhaltlich als auch wörtlich entnommene Inhalte wurden als solche kenntlich gemacht. Die Arbeit hat in dieser oder vergleichbarer Form noch keinem anderem Prüfungsgremium vorgelegen.

Hannover, den 30. September 2022 Moritz von Boehn

Abstract

The thesis presents the results of the evaluation of the probe field induced ac-Stark shift and an ion temperature analysis based on a theoretical model for sympathetic Doppler cooling in the $^{115}In^+$ clock at PTB. The clock is based on a mixed-species Coulomb crystal trapped in a linear Paul trap, where the $^{115}In^+$ clock ions are sympathetically cooled by $^{172}Yb^+$.
The probe field induced ac-Stark shift consists of two contributions, the probe field ellipticity-induced shift and the ac-Stark shift by far off-resonant transitions. In an experimental analysis, the ellipticity-induced shift is determined to be $(0 \pm 4) \times 10^{-22}$. The ac-Stark shift by far off-resonant transitions is calculated to be $(-2 \pm 5) \times 10^{-22}$ in a theoretical analysis. As the sum of both investigated contributions, the total probe field induced ac-Stark shift is evaluated at $(-2 \pm 6) \times 10^{-22}$.
A theoretical model for sympathetic Doppler cooling is presented and used to analyze the cooling dynamics in all phases of the clock spectroscopy sequence. The model predicts ion temperatures $< 0.8\,\mathrm{mK}$ during the clock interrogation and, neglecting anomalous heating sources, $\leq 2.5\,\mathrm{mK}$ throughout all remaining phases in the sequence. Based on the results of the temperature analysis, possible improvements are identified and the spectroscopy sequence is optimized regarding low ion temperatures and duty cycle.

Contents

1 Introduction

The development of precise timekeeping based on atomic references is an ongoing success story. Starting with the first realization of microwave atomic clocks in 1955, which enabled fractional frequency uncertainties in the 10^{-9} region [1], modern clocks based on optical transitions in the THz to PHz regime are approaching the 10^{-19} level [2–5].
The continuous improvement over the last decades unlocked more and more application fields in science and industry. Nowadays, modern optical clocks enable height resolutions in the cm regime which makes them interesting for geodesy [6] and for the search for new physics beyond the standard model [7]. In addition, atomic clocks are essential components in telecommunication networks and global navigation satellite system (GNSS) [8].
Although optical atomic clocks possess systematic uncertainties about two orders of magnitude smaller than the most precise cesium microwave clocks [9], the definition of the SI-second based on the primary standard ^{133}Cs has not changed since its introduction in 1967 [10]. Therefore, many groups all over the world are investigating possible clock species candidates for new frequency standards and a redefinition of the SI-second based on an optical transition [11, 12].
There are two common realizations of an optical clock, namely lattice clocks, where several thousands of neutral atoms are stored in an optical lattice, and ion clocks, where a single clock ion is trapped in a radio frequency Paul trap. Both approaches have their benefits. Lattice clocks feature an intrinsically low instability (or statistical uncertainty) and therefore need less averaging time τ to reach a desired frequency resolution, while ion traps allow an exceptional level of control over external perturbations to the internal state energies [13].
A species with favorable properties for highly accurate optical clocks is $^{115}\mathrm{In}^+$ [14]. Besides a suitably narrow clock transition with a frequency on the order of 1 PHz, it features favorable properties for the realization of a multi-ion-clock, such as a nearly vanishing quadrupole moment and a transition for state readout [15]. In a multi-ion clock, multiple clock ions are trapped and simultaneously probed. The resulting increased signal to noise ratio allows to reduce the averaging time τ by a factor (at least) equal to the number of clock ions N. Therefore, a multi-ion clock combines advantages of neutral atom lattice and single ion clocks.
Our group follows this approach by trapping multiple ions in a Coulomb crystal. These Coulomb crystals allow to simultaneously trap ions of different species which then serve different purposes. The indium clock at Physikalisch-Technische Bundesanstalt (PTB) is based on a linear mixed-species Coulomb crystal, where the $^{115}\mathrm{In}^+$ ions are sympathetically cooled by $^{172}\mathrm{Yb}^+$. Sympathetic cooling relies on the Coulomb interaction between the ions and the resulting coupled motion of all ions in the trapping potential. When one species is laser cooled, the reduction of thermal energy is, as a result of the coupling, distributed to all remaining ions in the crystal.
In spring 2022, our clock attended an international clock campaign for the first time [16]. Before scaling to multiple clock ions, the clock was operated with a single indium ion. During the campaign, frequency ratios between the $^{115}\mathrm{In}^+$ clock and other contributing optical clocks were measured. Besides an accuracy improvement of the currently most accurate indium frequency ratio $^{87}\mathrm{Sr}/^{115}\mathrm{In}^+$ [17] by about two orders of magnitude, additional new ratios such as $^{171}\mathrm{Yb}^+/^{115}\mathrm{In}^+$ and $^{171}\mathrm{Yb}/^{115}\mathrm{In}^+$ could be determined on the 10^{-17} to 10^{-18} level.
To achieve high accuracies in these frequency ratio measurements, a thorough analysis of systematic frequency shifts and their uncertainties is necessary. This thesis contributes to the investigation of two contributions. After chapters 2 and 3 review the basic theoretical background of the content of this work and give an overview of the experimental setup of the $^{115}\mathrm{In}^+$ clock at PTB, a complete analysis of the probe field induced ac-Stark shift is presented in chapter 4. The shift consists of two contributions, the probe field ellipticity-induced shift as presented by V.I. Yudin [18] and the ac-Stark shift by far off-resonant transitions. The total probe field induced shift is evaluated at a fractional value of $(-2 \pm 6) \times 10^{-22}$.
One of the largest contribution to the total frequency uncertainty is the time dilation shift due

to the residual thermal motion of the ions in the trapping potential. In addition, this motion also increases the statistical uncertainty by the temperature dependent decrease of contrast. Both motivate a detailed analysis of the ion temperature and its dynamics throughout the clock spectroscopy sequence. Such an analysis is carried out in chapter 5 based on a theoretical model of sympathetic Doppler cooling [19]. The model predicts clock ion temperatures $< 0.8\,\mathrm{mK}$ during the clock interrogation and, neglecting anomalous heating by e.g. background gas collisions, $\leq 2.5\,\mathrm{mK}$ during all contributing phases of the sequence such as state preparation and readout. Based on the results of the temperature analysis, the sequence is further optimized to reach lower ion temperatures and to improve on duty cycle.

2 Theoretical Background

This chapter is structured as follows. Section 2.1 reviews the basic principle of atomic clocks, followed by an overview over the statistical uncertainty and systematic frequency shifts presented in 2.2 and 2.3. Section 2.4 introduces the linear Paul trap and a description of the ion motion in the trapping potential, 2.5 gives a brief introduction on cooling techniques. Lastly, 2.6 presents a short derivation of the quantum mechanical description of ion-light interaction and a method to evaluate ion temperatures from experimentally acquired spectroscopic data.

2.1 Principle of an optical atomic clock

The basic principle of atomic clocks is to stabilize a (clock) laser to an atomic reference. Here the reference is typically an optical electronic (clock) transition with a frequency $\nu_A \approx 10^{14} \dots 10^{15}$ Hz which is probed by the laser light field of frequency ν_L. After probing, the atom can either be in the ground $|g\rangle$ or excited state $|e\rangle$. The transition probability p depends on the frequency difference $\delta_\nu = \nu_L - \nu_A$. This detuning δ_ν is kept as small as possible via a feedback loop. Because it is not possible to completely isolate the atom from its environment, the reference frequency ν_A also depends on external influences such as unwanted magnetic or electric fields $\mathbf{B}$ and $\mathbf{E}$. These influences result in systematic frequency shifts $\delta_{\text{sys}}/(2\pi)$, which shift the unperturbed transition frequency ν_0 to the experimentally observable frequency $\nu_A = \nu_0 + \delta_{\text{sys}}/(2\pi)$. There are two measures of an atomic clock's performance. The statistical frequency uncertainty originates predominantly from the measurement noise when probing the atomic reference. The systematic frequency uncertainty describes how precise the sum of all systematic frequency shifts δ_{sys} is known. Both are discussed in the following sections.
Currently, the most precise atomic clocks are based on one of two approaches: Lattice clocks, in which large ensembles of several thousands of neutral atoms are trapped in optical lattices, and ion clocks, where one or multiple ions are trapped in a radio frequency (rf) Paul trap such as the $^{115}\text{In}^+$ clock at PTB. For a general overview on optical atomic clocks see e.g. [13].

2.2 Statistical frequency uncertainty

Information on the detuning δ_ν is acquired via repeated population measurements (probing). Since in every measurement the ion is projected into either $|g\rangle$ or $|e\rangle$, the gain in information on δ_ν depends on the number of averaged population measurements. Because every probing iteration takes a time t, the reduction of δ_ν is a function of the total averaging time $\tau = N_{\text{it}} t$ where N_{it} is the number of iterations. Therefore, $\delta_\nu(\tau)$ is the dominating contribution to the statistical frequency uncertainty of an atomic clock. The statistical frequency uncertainty is fundamentally limited by the quantum projection noise (QPN) [20]. The QPN limited fractional frequency uncertainty is given by [21]

$$\sigma_y(\tau) = \frac{\delta\nu(\tau)}{\nu_0} = \frac{1}{\kappa}\frac{\Delta\nu}{\nu_0}\frac{1}{\sqrt{N_{\text{ions}}}}\sqrt{\frac{t}{\tau}} \propto \sqrt{\frac{p(1-p)}{N_{\text{ions}}\tau}}, \tag{2.1}$$

where κ is a numerical factor on the order of 1, $\Delta\nu$ is the frequency resolution and N_{ions} is the number of probed ions. Since the unperturbed clock transition frequency ν_0 is an intrinsic feature of the clock species, the statistical uncertainty is usually given as fractional frequency uncertainty $\delta_\nu(\tau)/\nu_0$ and denoted as $\sigma_y(\tau)$.
Usually, the QPN limit is not reached in the experiment. The time t needs to be seen as lower limit for the time $t_m = t + t_d$ of each iteration. Here t_d is the dead time, in which the atoms/ions are e.g. cooled or the clock states are read out. Therefore, to decrease the statistical uncertainty and hence the instability of the clock, it is advantageous to maximize the duty cycle, which is defined as the fraction $t/t_m \leq 1$. Phases in clock operation which contribute to the dead

time will be presented in section 3.3. In addition, due to a finite temperature of the atoms/ions during the interrogation, the maximum excitation probability p is limited, as will be shown in section 2.6.

2.3 Systematic frequency shifts

As mentioned in section 2.1, the experimentally observed clock frequency ν_A is shifted relative to the unperturbed frequency ν_0 due to systematic frequency shifts δ_{sys}. There are multiple contributions to δ_{sys} which need to be evaluated for an atomic clock (see e.g. [13]), three of which are discussed in this thesis: The Doppler shift, the ac-Stark shift and the 1st order Zeeman shift.

2.3.1 Doppler Shift

The Doppler shift originates from the motion of the clock ion in the trapping potential (see section 2.4) relative to the clock laser and can be separated into two contributions, the 1st order Doppler shift δ_{1D} and the 2nd order Doppler shift (also called time dilation shift) δ_{2D}. The 1st order Doppler shift results from the motion of the ions along the direction of the clock laser $k-$vector $\mathbf{k}_L$ with $|\mathbf{k}_L| = k_L = 2\pi/\lambda_L$ and the respective wavelength λ_L. δ_{1D} is given by

$$\delta_{\text{1D}} = -\mathbf{k}_L\mathbf{v} = -\frac{2\pi v_{\parallel}}{\lambda_L} = -\frac{2\pi v_{\parallel}\nu_L}{c} \tag{2.2}$$

where c is the speed of light, $\mathbf{v}$ the ion's velocity vector and $v_{\parallel}$ the projection of $\mathbf{v}$ onto $\mathbf{k}_L$ (see e.g. [13, 22]). When the ion is cooled sufficiently into the Lamb-Dicke regime, the 1st order Doppler shift becomes negligible [23].
The 2nd order Doppler shift is caused by time dilation due to the motion of the ion in the trapping potential and is therefore of relativistic nature. It is given by [13]

$$\delta_{\text{2D}} = -\frac{\langle E_{\text{kin}}\rangle}{mc^2}, \tag{2.3}$$

where $\langle E_{\text{kin}}\rangle$ is the mean total kinetic energy, k_B the Boltzmann constant and m the mass of the clock ion. The thermal time dilation shift results from thermal motion and depends on the mean kinetic energy $\langle E_{\text{kin}}\rangle_{th}$ (see e.g. [19])

$$\delta_{\text{2D},th} = -\frac{\langle E_{\text{kin,rad1}}\rangle_{th}}{mc^2} - \frac{\langle E_{\text{kin,rad2}}\rangle_{th}}{mc^2} - \frac{\langle E_{\text{kin,ax}}\rangle_{th}}{mc^2} \tag{2.4}$$

$$= -\frac{\kappa k_B\langle T_{\text{rad1}}\rangle}{2mc^2} - \frac{\kappa k_B\langle T_{\text{rad2}}\rangle}{2mc^2} - \frac{k_B\langle T_{\text{ax}}\rangle}{2mc^2}, \tag{2.5}$$

where $\langle T\rangle$ are the mean temperatures corresponding to the motion along the three principal trap axes in the rf Paul trap and $\kappa \approx 2$ is a correction factor when intrinsic micromotion is taken into account. The thermal time dilation shift can only be decreased by a reduction of $\langle T\rangle$. This motivates the analysis and optimization of Doppler cooling in chapter 5. A second relevant contribution to the time dilation shift is caused by excess micromotion (see [24]), but will not be discussed within this work.

2.3.2 ac-Stark shift

In a system of two atomic states $|g\rangle$ and $|e\rangle$ with energies E_g and E_e, the ac-Stark shift is a consequence of the interaction of an oscillating electric field $\mathbf{E}$ with a frequency $\omega = 2\pi f$ (e.g. from a laser beam) and the electric dipole moment operator $\mathbf{d}$. In case of a large detuning

$\Delta = \omega - \omega_0$ of the electric field with respect to the transition frequency $\omega_0 = 2\pi f_0 = \Delta E/\hbar = (E_e - E_g)/\hbar$, the ground and excited state experience an energy shift [22]

$$\Delta E_{g/e,\mathrm{ac-Stark}} = \pm\frac{\hbar|\Omega|^2}{4\Delta} = \pm\frac{(d_{eg}E)^2}{4\Delta\hbar}, \tag{2.6}$$

where $d_{eg} = \langle g|\mathbf{d}|e\rangle$ is the dipole matrix element between the states $|g\rangle$ and $|e\rangle$, $\Omega = -d_{eg}E/\hbar$ the Rabi frequency (see section 2.6) of the transition $|g\rangle \rightarrow |e\rangle$ and $E = |\mathbf{E}|$ the absolute value of the electric field amplitude. A schematic of the respective energy shifts of the ground and excited state is shown in Fig. 2.1.

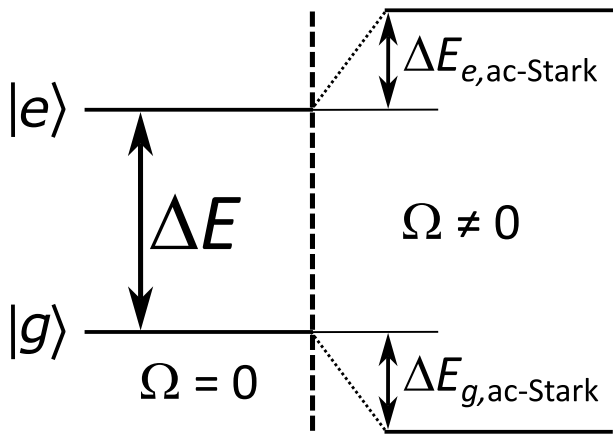

Figure 2.1 Ac-Stark shift of the ground and excited state energies assuming $\Delta < 0$. In the presence of a far detuned oscillating electric field at frequency ω, the energy levels of the ground and excited state $|g\rangle$ and $|e\rangle$ are shifted by the ac-Stark shift $\Delta E_{g/e,\mathrm{ac-Stark}}$ relative to the unperturbed energies E_g and E_e. The shifts are opposite in sign for the ground and excited state and inversely proportional to the detuning $\Delta = \omega - \omega_0$ with respect to the unperturbed transition frequency $\omega_0 = (E_e - E_g)/\hbar$.

Eq. 2.6 holds for $|\Delta| \gg |\Omega|$ and in the rotating wave approximation, where terms oscillating at $(\omega + \omega_0) \gg \Delta$ are neglected. For a detailed derivation see e.g. [22, 25].
The impact of this energy shift originating from the probe electric field on the clock transition frequency will be investigated in chapter 4.

2.3.3 1st order Zeeman shift

The 1st order Zeeman shift originates from the interaction of each clock state magnetic dipole moment μ with a magnetic field $\mathbf{B}$. For hyperfine states, the energy levels are shifted by [25]

$$\Delta E_{1\mathrm{Z}} = \mu_B g_F m_F B, \tag{2.7}$$

where μ_B is the Bohr magneton, g_F the $g-$factor, m_F the magnetic quantum number and $|\mathbf{B}| = B$ the absolute value of the magnetic field. Since each clock state $|g\rangle$, $|e\rangle$ has a different $g-$factor value $g_{F,g}$ and $g_{F,e}$, both energy shifts differ from each other. The changed energy difference then leads to a frequency shift of the clock transitions. A scheme to cancel the shift is presented in 4.1.1.

2.4 Trapping of ions

The $^{115}\mathrm{In}^+$ clock at PTB is based on trapped ions. This section presents a brief introduction on the linear Paul trap and gives a derivation of the description of the ion motion.

To trap ions, it is necessary to produce a 3D confining potential. 3D confinement cannot be produced by a combination of static electric fields, since the corresponding potential Φ needs to fulfill Laplace's equation $\Delta\Phi = 0$. Such a combination would always lead to an anti-confinement in at least 1 direction, as shown in e.g. [26, 27]. To solve this problem, there are two common approaches to trap charged particles. The first is to combine a static electric quadrupole field with a homogeneous magnetic field, known as Penning trap (see e.g. [28]). Since this type of ion trap is not important for this thesis, it will not be further discussed. The second approach uses an oscillating electric quadrupole field. This approach called Paul trap [29] is also used to trap ions in the indium clock setup. Its basic theoretical background is given in the following.

2.4.1 Trapping in a linear Paul trap

Confinement in the radial $xy-$plane of a linear Paul trap is provided by four electrodes, and depending on the trap setup, two or four end electrodes for the axial confinement along the $z-$axis. A schematic of a linear Paul trap in the radial plane is shown in Fig. 2.2.

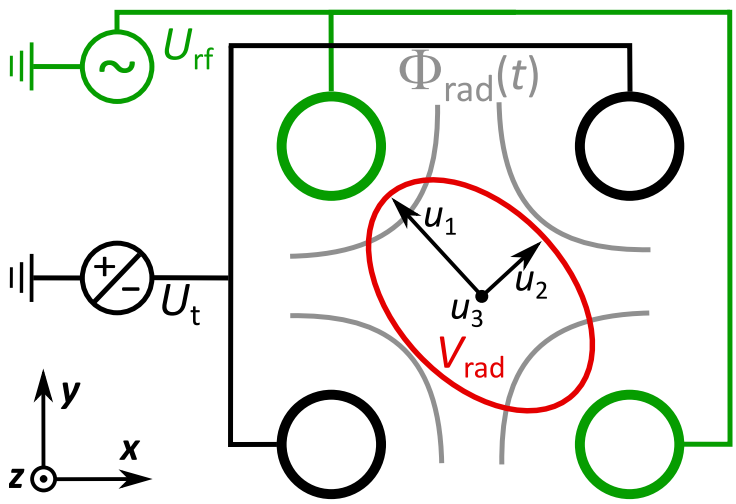

Figure 2.2 Radial plane of a linear Paul trap. For the radial confinement, an oscillating voltage $U_{rf} \times \cos(\Omega_{rf}t)$ in the radio frequency (rf) regime is applied between the green and the black electrodes, resulting in an oscillating electric quadrupole potential $\Phi_{rad}(t)$, schematically shown by grey lines. The difference between the radial potentials $V_{rad1/2}$ along the two radial trap axes u_1 and u_2 can be set by the dc voltage U_t. The combination results in a harmonic confining radial potential V_{rad} shown by the red equipotential surface (red ellipse).

To produce the radial confinement, an oscillating voltage $U_{rf} \times \cos(\Omega_{rf}t)$ with a frequency Ω_{rf} in the radio frequency (rf) regime is applied to two electrodes shown as green circles in Fig. 2.2. The setup of all four electrodes then produces an oscillating electric quadrupole potential $\Phi_{rad}(t)$ in the radial plane (shown schematically as grey lines). Due to the oscillating sign of U_{rf}, the trapped ions experience a continuous change between a confining and anti-confining potential, leading to a harmonic radial confinement described by V_{rad}, shown schematically by the red equipotential surface. The force resulting from this potential pushes the trapped ions towards the center of the ellipse which is the center of the trap. The ellipticity of V_{rad} can be set by the applied dc voltage U_t, where the main axes of the ellipse are the radial trap axes u_1 and u_2. To create an axial confinement, the dc electrodes are segmented and a voltage U_{dc} is applied between the grey end electrodes and the black electrodes in Fig. 2.3.

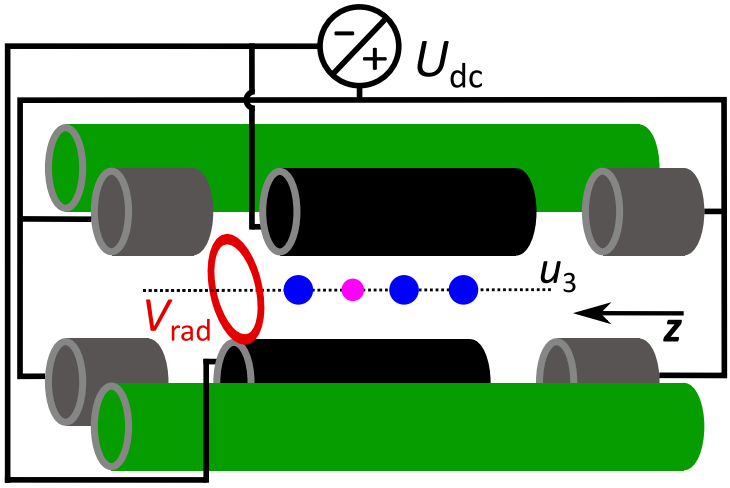

Figure 2.3 3D schematic of a linear Paul trap. To produce the axial confinement, a dc voltage U_{dc} is applied between the grey and black electrodes, resulting in a harmonic trapping potential V_{ax} along the trap axis $u_3 \parallel z$. Depending on the chosen trapping voltages U_{rf}, U_t and U_{dc}, multiple ions of different species can be trapped in a linear chain as shown by blue and pink circles.

The applied voltage U_{dc} produces a harmonic trapping potential with a trap frequency $\omega_{ax} = 2\pi\nu_{ax}$ along the trap axis $u_3 \parallel z$. Depending on the chosen radial and axial confinement, multiple ions of different species can be trapped in a linear chain along u_3 as a Coulomb crystal (blue and pink circles).

2.4.2 Motion of a single trapped ion in a linear Paul trap

Before a description of the motion of multiple ions is presented in 2.4.3, this subsection gives a short derivation of the equations of motion of a single trapped ion in a linear Paul trap which follows [21]. For a more detailed derivation see [30, 31].
The radial potential Φ_{rad} close to the center of the Paul trap is given by

$$\Phi_{rad1} = (\kappa_{rf} U_{rf} \cos(\Omega_{rf} t) - \kappa_{dc} U_t) \frac{u_1^2}{2d} \tag{2.8}$$

$$\Phi_{rad2} = -(\kappa_{rf} U_{rf} \cos(\Omega_{rf} t) - \kappa_{dc} U_t) \frac{u_2^2}{2d} \tag{2.9}$$

$$\Phi_{rad} = \Phi_{rad1} + \Phi_{rad2}. \tag{2.10}$$

Here u_1,u_2 are the coordinates along the two radial trap axes, κ_{rf} and κ_{dc} are geometric corrections on the order of 1 and d is the radial distance from the center to the electrodes.
It is common to continue with the dimensionless q parameters

$$q_1 = -q_2 = \frac{2e\kappa_{rf} U_{rf}}{md^2 \Omega_{rf}^2} \tag{2.11}$$

$$q_3 = 0, \tag{2.12}$$

and a parameters

$$a_{1/2} = -\frac{2\omega_{ax}^2}{\Omega_{rf}^2} \pm \frac{4e\kappa_{dc} U_t}{md^2 \Omega_{rf}^2} \tag{2.13}$$

$$a_3 = \frac{4\omega_{ax}^2}{\Omega_{rf}^2}, \tag{2.14}$$

where e and m are the charge and the mass of the trapped ion. Using the q and a parameters, the equations of motion are given by

$$\ddot{u}_k + (a_k + 2q_k\cos(\Omega_{\mathrm{rf}})t)\frac{\Omega_{\mathrm{rf}}^2}{4}u_k = 0, \tag{2.15}$$

with $k = \{1, 2, 3\}$, known as the homogeneous Mathieu differential equations. An inhomogeneity $\propto E_{\mathrm{dc}} = |\mathbf{E}_{\mathrm{dc}}|$ needs to be added on the right hand side when external electric stray fields $\mathbf{E}_{\mathrm{dc}}$ are present. As the influence of stray fields on the ion motion is not of major interest in this thesis, the inhomogeneity is neglected in the following. It can be shown that under the condition $|a_i|, |q_i| \ll 1$, the solution to the set of differential equations in 2.15 can be approximated by

$$u_{1/2}(t) \approx u_{(1),1/2}\cos(\omega_{\mathrm{rad}1/2}t)(1 + \frac{q_{1/2}}{2}\cos(\Omega_{\mathrm{rf}}\mathrm{t} + \phi_{1/2})) \tag{2.16}$$

$$u_3(t) \approx u_{(1),3}\cos(\omega_{\mathrm{ax}}t + \phi_3), \tag{2.17}$$

with motional amplitudes $u_{(1),k}$ and radial trap frequencies

$$\omega_{\mathrm{rad}1/2} = 2\pi\nu_{\mathrm{rad}1/2} = \frac{\Omega_{\mathrm{rf}}}{2}\sqrt{a_{1/2} + \frac{q_{1/2}^2}{2}}. \tag{2.18}$$

The fast oscillation at Ω_{rf} in Eq. 2.16 is called intrinsic mircomotion, while the oscillation at the trap (or secular) frequencies $\omega_{\mathrm{rad}1/2}$ and ω_{ax} is called secular motion. As can be seen from Eq. 2.16, the micromotion amplitude is a factor of $q_{1/2}/2$ smaller than the secular motion. In the stability regime considered here ($|a_i|, |q_i| \ll 1$), the secular motion can be treated as the harmonic motion in a static potential

$$V_{\mathrm{trap}} = \underbrace{\frac{m}{2}\omega_{\mathrm{rad}1}^2 u_1^2 + \omega_{\mathrm{rad}2}^2 u_2^2}_{V_{\mathrm{rad}}} + \underbrace{\frac{m}{2}\omega_{\mathrm{ax}}^2 u_3^2}_{V_{\mathrm{ax}}}. \tag{2.19}$$

2.4.3 Normal modes of a Coulomb crystal

When multiple ions are trapped in a Coulomb crystal, they do not only interact with the trapping potential, but also with each other by means of the Coulomb interaction. As a result, each ion motion depends on the motion of all remaining ions in the crystal. In a mixed species crystal, this coupling can be used to sympathetically cool a species without a suitable cooling transition by another which can be sufficiently cooled. Such a (linear) crystal is shown schematically in Fig. 2.3 (clock ion (pink) and cooling ions (blue)). Besides a convenient way to cool ions, the (coherent) manipulation of the coupled motion is the basis of the field of trapped-ion quantum logic (see e.g. [32, 33]). The collective motion can be described by a set of normal modes. A derivation of the normal mode structure following [34] is presented in this section.
Due to the Coulomb interaction, the trapping potential in Eq. 2.19 needs to be modified. Including the Coulomb potential V_{Coulomb} and assuming N ions of masses m_i, the total potential is given by

$$V = \sum_{i=1}^{N} V_{\mathrm{trap}}(\mathbf{u}_i, m_i) + \underbrace{\frac{1}{2}\sum_{i=1}^{N}\sum_{j=1, i\neq j}^{N}\frac{e^2}{4\pi\epsilon_0}\frac{1}{|\mathbf{u}_i - \mathbf{u}_j|}}_{V_{\mathrm{Coulomb}}}, \tag{2.20}$$

where ϵ_0 is the vacuum permittivity and $\mathbf{u}_i = (u_{1i}, u_{2i}, u_{3i})^T$ the position of the ith ion in the coordinate system defined by the three principal trap axes. It is assumed that the trapping parameters are chosen such that the ions are arranged in a linear chain (linear Coulomb crystal) [35], as it is the case in the indium clock setup. Under the assumption of small deviations

from the equilibrium position vector of each ion $\mathbf{u}_i^{(0)} = (u_{1i}^{(0)}, u_{2i}^{(0)}, u_{3i}^{(0)})^T$, the coordinates can be replaced by $\mathbf{u}_i(t) = \mathbf{u}_i^{(0)} + \mathbf{q}_i(t)$ with the time dependent motion $\mathbf{q}_i(t) = (q_{1i}(t), q_{2i}(t), q_{3i}(t))^T$. Now, the potential V given in Eq. 2.20 is expanded to second order around the equilibrium positions $\mathbf{u}_i^{(0)}$

$$V \approx \frac{1}{2} \sum_{k=1}^{3} \sum_{i,j=1}^{N} q_{ki} q_{kj} \underbrace{\left[\frac{\partial^2 V}{\partial u_{ki} \partial u_{kj}} \right]_{u_{ki}^{(0)}}}_{V_{kij}}, \tag{2.21}$$

where $\partial / \partial u_{ki}$ is the partial derivative with respect to the ith ion coordinate u_k. For every $k = \{1, 2, 3\}$ and hence for every trap axis, a set of N eigenvalue equation can be found

$$\sum_{j=1}^{N} V_{kij} \beta_{k\alpha,j} = \lambda_{k\alpha} m_i \beta_{k\alpha,i}. \tag{2.22}$$

Here $\alpha = 1, \ldots, N$ is the mode index, $\beta_{k\alpha,i}$ is the ith component of the mode eigenvector $\beta_{k\alpha}$ and $\omega_{k\alpha} = 2\pi\nu_{k\alpha} = \sqrt{\lambda_{k\alpha}}$ is the mode frequency. To solve the eigenvalue equations in Eq. 2.22, code written by J. Keller is used throughout this thesis. Once the mode eigenvectors $\beta_{k\alpha}$ are found, any motion of the ions in the Coulomb crystal can be expressed as a superposition of normal mode excitations

$$\pi_{k\alpha} = \sum_{i=1}^{N} \beta_{k\alpha,i} q_{ki}. \tag{2.23}$$

To describe the $3N$ normal mode excitations, there are in total $3N$ mode frequencies $\omega_{k\alpha}$ and 3 sets of N basis vectors $\{\beta_\alpha\}_k$.
Due to the different masses m_i of the ions, the mode eigenvectors $\beta_{k\alpha}$ are not orthogonal. To obtain orthogonal sets of eigenvectors, the above derivation needs to be repeated using the transformation $q_{ki} \to q'_{ki} = \sqrt{m_i} q_{ki}$ and $V_{kij} \to V'_{kij} = V_{kij}/\sqrt{m_i m_j}$ (see [34]). From this transformation in the mass-weighted space, normalized eigenvectors $\beta'_{k\alpha}$ are obtained

$$|\beta'_{k\alpha}| = \sqrt{\sum_{i}^{N} \beta_{k\alpha,i}^2} = 1. \tag{2.24}$$

These eigenvectors can be transformed back to real space via

$$\beta'_{k\alpha,i} \to \beta_{k\alpha,i} = \frac{\beta'_{k\alpha,i}}{\sqrt{m_i}}. \tag{2.25}$$

To give an example of the set of normal modes of a (mixed-species) linear Coulomb crystal consisting of three Yb^+ (blue) and a single In^+ (pink), the radial and axial real space mode eigenvectors $\beta_{k\alpha}$ are calculated and shown in Fig. 5.3. For the calculation it is assumed that the secular frequencies corresponding[1] to the mass $m_{\mathrm{Yb}} = 172\,(\mathrm{amu})$ of the ytterbium ions are $\nu_{\mathrm{rad}} = 825\,\mathrm{kHz}$ and $\nu_{\mathrm{ax}} = 275\,\mathrm{kHz}$.

[1] Note the mass dependence in Eqs. 2.13 and 2.18.

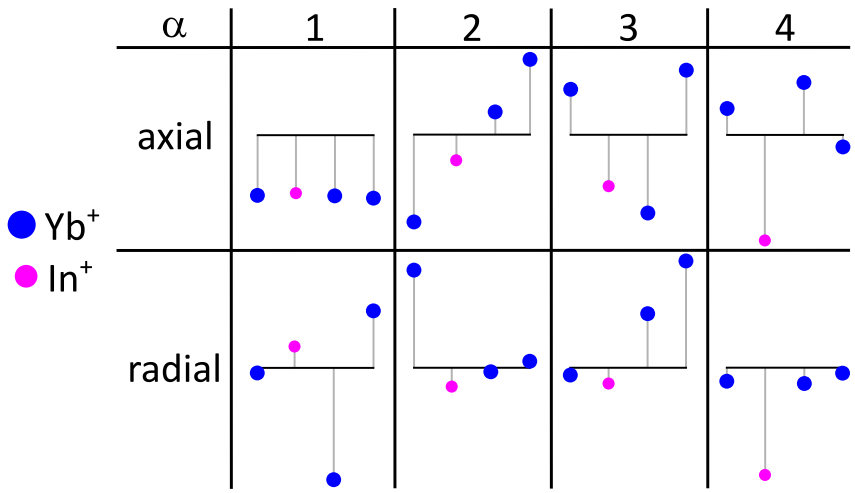

Figure 2.4 Radial and axial normal mode vectors of a linear mixed species Coulomb crystal. Assuming a four ion crystal consisting of three Yb^+ (blue) and one In^+ (pink), there are 4 axial modes and 2×4 radial modes. The ion displacements from their equilibrium positions (horizontal lines) are proportional to the real space eigenvector components $\beta_{k\alpha,i}$.

Each ion displacement relative to its equilibrium position (shown as horizontal lines) represents an eigenvector component $\beta_{k\alpha,i}$ in a radial or axial normal mode α.
In case of small kinetic energies, the normal mode excitations π_α need to be treated quantum mechanically. This is done by introducing the annihilation operators $a_{k\alpha}$ of the modes $k\alpha$ such that the normal mode excitations are given by

$$\pi_{k\alpha} = \sqrt{\frac{\hbar}{2\omega_{k\alpha}}} \left(a_{k\alpha} + a_{k\alpha}^\dagger \right). \tag{2.26}$$

Each mode can then be treated as a quantum mechanical harmonic oscillator with eigenstates $|n_{k\alpha}\rangle$ of the number operator $(a_{k\alpha})^\dagger a_{k\alpha}$ and discrete energy levels $E_{k\alpha}(n_{k\alpha})$

$$E_{k\alpha}(n_{k\alpha}) = \left(n_{k\alpha} + \frac{1}{2} \right) \hbar\omega_{k\alpha}. \tag{2.27}$$

Here $n_{k\alpha}$ is the occupation number and the energy offset $\hbar\omega_{k\alpha}/2$ is the ground state energy.
This quantum mechanical treatment will be important to describe the influence of the ion motion on the time evolution of the two states $|g\rangle$ and $|e\rangle$ in the interaction with light (see section 2.6).

2.5 Doppler cooling and sympathetic cooling

To keep the trapped ions in the crystallized phase and to reduce temperature related frequency shifts such as the thermal time dilation shift (see 2.3.1), it is necessary to apply laser cooling. A commonly used technique is Doppler cooling. It relies on deceleration in the process of photon scattering on a cooling transition. Assuming a single trapped ion and a cooling laser parallel to the ion velocity vector $\mathbf{v}$, each absorbed photon changes the ion momentum $|\mathbf{p}| = m|\mathbf{v}|$ by $\Delta p = \hbar k$. Here $k = 2\pi/\lambda_{\text{cool}} = |\mathbf{k}|$ with the wavelength of the cooling transition λ_{cool} and the cooling laser wave vector $\mathbf{k}$. While the photon absorption is always along the direction of $\mathbf{k}$, the emission is randomly directed. Therefore, the random direction of the emitted photons results in a random walk and vanishing average momentum transfer [22].
To effectively cool the ion in the process of photon absorption, it is necessary to have a dependence of the absorption process on the ion velocity $|\mathbf{v}|$ and its direction. Since the ion is oscillating back and forth along the direction of the laser beam, without such a dependence, the photon's absorbed momenta would average out. Here the 1st order Doppler shift comes into

play. Following [31], the average force on the ion due to the photon absorption is proportional to the scattering rate Γ_{sc} given by

$$F = \hbar k \Gamma_{\text{sc}} = \hbar k \frac{\Gamma}{2} \frac{s}{1 + s + (\frac{2\delta_{\text{eff}}}{\Gamma})^2}, \tag{2.28}$$

with the saturation coefficient of the cooling transition $s = 2|\Omega|^2/\Gamma^2$, the corresponding Rabi frequency Ω and the natural linewidth Γ. In addition, the scattering rate also depends on $\delta_{\text{eff}} = \Delta_0 - \mathbf{kv}$, with the detuning $\Delta_0 = \omega_L - \omega_{\text{cool}}$ of the cooling laser field (frequency ω_L) with respect to the cooling transition frequency ω_{cool} and the 1st order Doppler shift $-\mathbf{kv}$. When choosing a fixed $\Delta_0 < 0$, usually $\approx -\Gamma/2$, the force is larger for motion towards the laser beam. The imbalance of the scattering force acting on the ion while moving towards or with the laser beam then leads to cooling.
This scheme is limited by the aforementioned momentum random walk due to the process of photon emission. The minimum reachable temperature is the well-known Doppler limit obtained for $s \to 0$ and for $\Delta_0 = -\Gamma/2$. It is given by (see e.g. [22])

$$T_{\text{D}} = \frac{\hbar\Gamma}{2k_B}, \tag{2.29}$$

where k_B is the Boltzmann constant. $T_{\text{D,Yb}} \approx 0.47\,\text{mK}$ for the $^2\text{S}_{1/2} \to {}^2\text{P}_{1/2}$ transition of $^{172}\text{Yb}^+$ with $\Gamma = 2\pi \times 19.6\,\text{MHz}$ (see section 3.1).
A model describing sympathetic Doppler cooling of the normal modes of a linear mixed species Coulomb crystal will be presented in section 5.1.

2.6 Rabi flopping and thermometry

Atomic clocks are based on excitation of the clock transition via interaction with the clock laser field. In the interaction, the population is transferred from the ground state $|g\rangle$ to the excited state $|e\rangle$ in a coherent way. This process is called Rabi flopping. A short derivation following [22] is presented in the following.
At first, a free two-level atom at rest interacting with an oscillation electric field is assumed. The corresponding Hamiltonian consists of two parts

$$H = H_0 + H_I(t), \tag{2.30}$$

where H_0 refers to the unperturbed atomic two level system and $H_I(t)$ to the time dependent interaction with the oscillating electric field. $H_I(t)$ introduces a perturbation of the eigenstates $|g\rangle$, $|e\rangle$ of H_0 whose eigenvalues are the corresponding energies E_g and E_e

$$H_0|g\rangle = E_g|g\rangle \tag{2.31}$$
$$H_0|e\rangle = E_e|e\rangle. \tag{2.32}$$

The general solution is given by

$$\Psi(\mathbf{r}, t) \approx \Psi(t) = c_g(t)|g\rangle e^{-i\omega_g t} + c_e(t)|e\rangle e^{-i\omega_e t}, \tag{2.33}$$

with $\omega_{g/e} = E_{g/e}/\hbar$, while the dependence on the electron position $\mathbf{r}$ is dropped in the dipole approximation. The approximation is justified by the fact that the spread of the atomic wave function is small compared to the wavelength of the laser. Since $\Psi(t)$ is normalized, the conditions $|c_g(t)|^2 + |c_e(t)|^2 = 1$ holds for the amplitudes $c_{g/e}$. The squared amplitudes $|c_{g/e}(t)|^2$ are the populations and describe the probability to find the atom in the state $|g\rangle$ or $|e\rangle$ at time t. Note that $|c_e|^2 \equiv p$ is equivalent to the excitation probability p in an atomic clock experiment (as used in Eq. 2.1).

Assuming a linearly polarized electric field $\mathbf{E}(t) = E_0\mathbf{a}\cos(\omega_L t)$ with the polarization vector $\mathbf{a}$, $H_I(t)$ is given by

$$H_I(t) = e\mathbf{r}\mathbf{E} = -\mathbf{d}\mathbf{E}. \tag{2.34}$$

Here e is the elementary charge and $\mathbf{d} = -e\mathbf{r}$ the electric dipole operator. H_I results in a time dependence of the populations of $|g\rangle$ and $|e\rangle$, which can be described by two coupled differential equations for the amplitudes $c_{g/e}(t)$

$$i\dot{c}_g = \Omega\cos(\omega_L t)e^{-i\omega_0 t}c_e \tag{2.35}$$

$$i\dot{c}_e = \Omega^*\cos(\omega_L t)e^{i\omega_0 t}c_g, \tag{2.36}$$

where $\omega_0 = (E_e - E_g)/\hbar$ is the transition frequency of the transition $|g\rangle \rightarrow |e\rangle$ and Ω is the (free atom) Rabi frequency defined by

$$\Omega = -\frac{\langle g|\mathbf{d}_a|e\rangle E_0}{\hbar} = -\frac{d_{eg,a}E_0}{\hbar}. \tag{2.37}$$

$d_{eg,a}$ is the dipole matrix element between the two states $|g\rangle$ and $|e\rangle$ for the component $\mathbf{d}_a$ of the dipole operator $\mathbf{d}$ parallel to the polarization vector $\mathbf{a}$. In the next step, the rotating wave approximation is applied, where fast rotating terms oscillating at $(\omega_L + \omega_0) \gg (\omega_L - \omega_0)$ are neglected. Assuming initial conditions $c_g(t = 0) = 1$ and $c_e(t = 0) = 0$, the time dependent populations $|\mathrm{c_g}|^2$ and $|\mathrm{c_e}|^2$ can be determined by solving the set of differential equations in Eqs. 2.35 and 2.36, such that

$$|c_e(t)|^2 = \frac{\Omega^2}{\Omega^2 + \Delta^2}\sin^2\left(\frac{\sqrt{\Omega^2 + \Delta^2}}{2}t\right) \tag{2.38}$$

$$|c_g(t)|^2 = 1 - |c_e(t)|^2 = \frac{\Omega^2}{\Omega^2 + \Delta^2}\cos^2\left(\frac{\sqrt{\Omega^2 + \Delta^2}}{2}t\right). \tag{2.39}$$

In case of resonant excitation, e.g. $\Delta \approx 0$, both equations simplify to

$$|c_e(t)|^2 = \sin^2\left(\frac{\Omega}{2}t\right) \tag{2.40}$$

$$|c_g(t)|^2 = \cos^2\left(\frac{\Omega}{2}t\right). \tag{2.41}$$

$$\tag{2.42}$$

As can be seen in the interaction of the two level system with the resonant electric field, the populations are oscillating as a function of the interrogation time t. These oscillations are known as Rabi oscillations (also denoted as Rabi flopping). When the interrogation time t is chosen to be $\tau_\pi = \pi/\Omega$, $|c_e(\tau_\pi)|^2 = 1$ and in a state measurement, the atom will be found in the excited state $|e\rangle$ (as can be seen from Eq. 2.33). Here τ_π is called $\pi-$pulse time.
Until now, the only considered influence on the populations $|c_{g/e}|^2$ was the oscillating electric field. Since the excited state $|e\rangle$ has has a limited lifetime τ_{life}, it is possible that the Rabi oscillation is damped by the decoherent process of spontaneous emission from $|e\rangle$ to $|g\rangle$. In case of resonant excitation and including spontaneous emission, the population $|c_e|^2$ can be described by [25]

$$|c_e(t)|^2 = \frac{1}{2}\frac{\Omega^2}{\Omega^2 + \Gamma^2/2}\left[1 - e^{-(3\Gamma/4)t}\left(\cos(\Omega_\Gamma t) + \frac{3\Gamma}{4\Omega_\Gamma}\sin(\Omega_\Gamma t)\right)\right], \tag{2.43}$$

with the damped Rabi frequency $\Omega_\Gamma = \sqrt{\Omega^2 - (\Gamma/4)^2}$ and the natural linewidth $\Gamma = 1/\tau_{\mathrm{life}}$ of the transition $|g\rangle \rightarrow |e\rangle$. The process of spontaneous emission leads to damping of the Rabi oscillation (proportionality $e^{-(3\Gamma/4)t}$). For large free atom Rabi frequencies $|\Omega| \gg \Gamma$ and short

interrogation times $t \ll \tau_{\text{life}}$, the Rabi oscillations are approximately described by Eqs. 2.40 and 2.41. In case of small Rabi frequencies Ω and interrogation times t on the order of the excited state lifetime τ_{life}, which are both desirable in atomic clocks, spontaneous decay has a considerable effect on the maximum measured excitation probability $p = |c_e(t)|^2$.
So far, the atom was assumed free (without confinement) and at rest. In case of trapped ions in real experiments, both assumptions are not valid due to the confining potential and the finite end temperature of the cooling process. Here the excited state time evolution also depends on the residual motion which is in general described a superposition of Fock states $\bigotimes_{k\alpha}|n_{k\alpha}\rangle$. The excited state time evolution in the absence of spontaneous emission (cf. Eq. 2.43) of the ith probed ion is given by (see [21, 31])

$$|c_{e,i}(t)|^2 = \sum_{k=1}^{3} \sum_{n_{k1},\ldots,n_{kN}=0}^{\infty} \left(\prod_{\alpha=1}^{N} P_{k\alpha}(n_{k\alpha}) \right) \sin^2 \left(\frac{\Omega}{2} \prod_{\alpha=1}^{N} \mu_{n_{k\alpha},n'_{k\alpha}} t \right), \tag{2.44}$$

where $P_{k\alpha}(n_{k\alpha})$ is the thermal occupation of the state $|n_{k\alpha}\rangle$ and

$$\mu_{n_{k\alpha},n'_{k\alpha},i} = \langle n'_{k\alpha}| e^{i\eta_{k\alpha,i}(a_{k\alpha}+a^\dagger_{k\alpha})} |n_{k\alpha}\rangle \tag{2.45}$$

$$= e^{-\frac{1}{2}\eta^2_{k\alpha,i}} \sqrt{\frac{n_{k\alpha<}!}{(n_{k\alpha<}+\Delta n_{k\alpha})!}} (i\eta_{k\alpha,i})^{\Delta n_{k\alpha}} L^{\Delta n_{k\alpha}}_{n_{k\alpha<}}(\eta^2_{k\alpha,i}). \tag{2.46}$$

Here $\Delta n_{k\alpha} = |n'_{k\alpha} - n_{k\alpha}|$, $n_{k\alpha<} = \min\{n_{k\alpha}, n'_{k\alpha}\}$, $L^\alpha_n(x)$ is a generalized Laguerre polynomial and $\eta_{k\alpha,i}$ is the Lamb-Dicke parameter [36], defined by

$$\eta_{k\alpha,i} = \underbrace{k_L \cos(\theta)}_{k_{L,k\alpha}} \beta'_{k\alpha,i} \sqrt{\frac{\hbar}{2m_i\omega_{k\alpha}}}. \tag{2.47}$$

The Lamb-Dicke parameter describes the influence of the ion motion on the interaction with the laser field. The cosine dependence describes the projection $|\mathbf{k}_{L,k\alpha}| = k_{L,k\alpha}$ of the probe field $k-$vector $\mathbf{k}_L$ onto the mode principal axes. Following [37], in thermal equilibrium, the thermal occupation $P_{k\alpha}(n_{k\alpha})$ can be expressed in terms of the mean mode occupation number $\bar{n}_{k\alpha}$ of each mode $k\alpha$

$$P_{k\alpha}(\bar{n}_{k\alpha}, n_{k\alpha}) = \frac{1}{\bar{n}_{k\alpha}+1} \left(\frac{\bar{n}_{k\alpha}}{\bar{n}_{k\alpha}+1} \right)^{n_{k\alpha}}. \tag{2.48}$$

Since each mode is treated as an 1D harmonic oscillator whose total energy is $k_B T$, the mean occupation number can be connected to a mode temperature $T_{k\alpha}$ via

$$T_{k\alpha} = \frac{\hbar\omega_{k\alpha}\bar{n}_{k\alpha}}{k_B}. \tag{2.49}$$

By combining Eqs. 2.44, 2.48 and 2.49, an expression for the ith probed ion excited state time evolution as influenced by three sets of mode temperatures $\{T_\alpha\}_k$ is obtained.
From Eq. 2.44 one can see that in presence of motion, the excited state time evolution is a sum of (infinetly) many Rabi oscillations with different amplitudes and frequencies. This behavior is called thermal dephasing and results in a mode temperature dependent decrease of the maximum excitation probability. The higher the mode temperatures $T_{k\alpha}$, the broader the distributions $P_{k\alpha}$ and the faster the dephasing of all oscillations. Therefore, low temperatures are desirable to reduce the effect of thermal dephasing and to keep a high maximum excitation probability.
The temperature dependence allows to estimate the ion temperature by comparison of experimentally observed Rabi flops with calculated oscillations assuming an excited state population given by Eq. 2.44. This method is used throughout this thesis to determine mode temperatures

$T_{k\alpha}$ as well as free atom Rabi frequencies Ω from experimental data. The calculation of theoretical thermally dephasing on resonance Rabi oscillations is done using a modification of a python script written by J. Keller. Besides the effect of thermal dephasing, the script also takes into account the effect of decoherence by spontaneous emission decribed in Eq. 2.43. The script assumes projections $k_{L,k\alpha}$ onto the two radial axes and no projection onto the modes of the trap axis, as it is the case for the probe beam in the indium setup (see section 3.2). Moreover, for simplicity, it is assumed that all modes of a radial trap axis are at the same temperature. Since there are two radial trap axes, two radial temperatures T_{rad1} and T_{rad2} can be entered.
To give an example, three Rabi flops for different radial temperatures and a fixed free atom rabi frequency $\Omega/(2\pi) = 50\,\mathrm{Hz}$ are plotted in Fig. 2.5. For the calculation, the crystal configuration as well as mode frequencies corresponding to the mode structure shown in Fig. 5.3 are assumed. Moreover, it is assumed that the probe beam is at the indium clock transition wavelength $\lambda_{\mathrm{clock}} \approx 236.5\,\mathrm{nm}$ and has an equal projection onto both radial trap axes, leading to $\theta = 45°$ in the calculation of the Lamb-Dicke parameters (see Eq. 2.47).

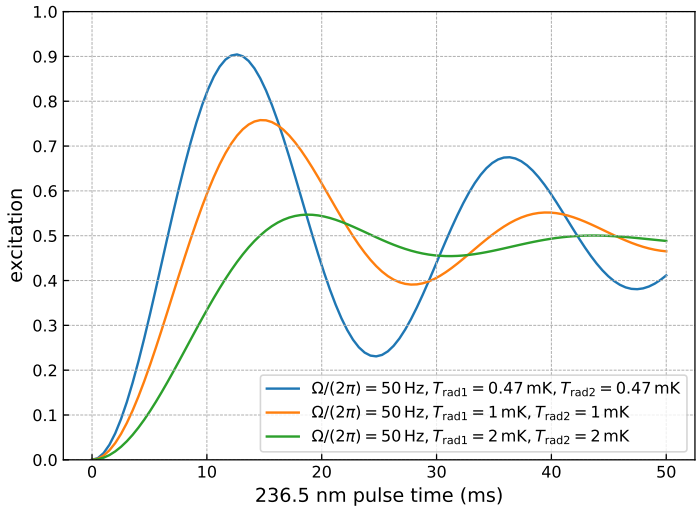

Figure 2.5 Thermally dephasing Rabi oscillations. Three theoretical Rabi flops (solid lines) are calculated assuming an equal projection of the probe beam onto the modes of both radial trap axes and no projection onto the axial modes. The resulting maximum excitation decreases with increasing radial temperatures. The peak excitations are reached for pulse times $\tau_{\mathrm{pulse}} > \tau_\pi = 10\,\mathrm{ms}$.

As can be seen, higher assumed radial temperatures reduce the maximum excitation. In addition, a free atom would reach its maximum excitation probability after the $\pi-$time $\tau_\pi = \pi/\Omega = \pi/(2\pi \times 50\mathrm{Hz}) = 10\,\mathrm{ms}$. The oscillations resulting from the considered radial temperature sets reach their maximum excitations for pulse times $\tau_{\mathrm{pulse}} > \tau_\pi$, which is a result of the different thermal distributions $P_{k\alpha}(\bar{n}_{k\alpha})$.
Due to a missing projection of the probe beam onto the axial modes in the indium clock setup, it is not possible to deduce corresponding temperatures from experimentally acquired Rabi flops. This motivates the theoretical temperature analysis of the axial and radial temperatures in chapter 5.

3 Experimental Setup

This chapter presents the relevant parts of the experimental setup of the $^{115}\mathrm{In}^+$ clock at PTB. Section 3.1 gives an overview over the atomic systems of the used species. Afterwards, the ion trap setup is presented in section 3.2 followed by the clock spectroscopy sequence used in the spring 2022 clock campaign.

3.1 Atomic systems

The clock is based on $^{115}\mathrm{In}^+$, trapped together with $^{172}\mathrm{Yb}^+$ sympathetic cooling ions in a linear Coulomb crystal. Reduced level schemes with all relevant transitions are shown in Fig. 3.1.

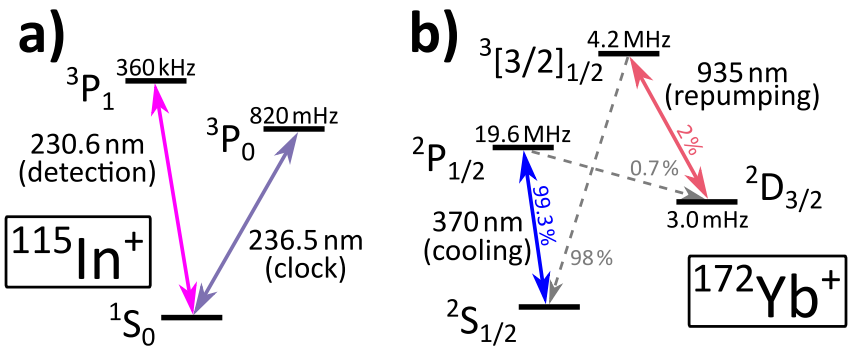

Figure 3.1 Reduced level schemes of $^{115}\mathrm{In}^+$ (a) and $^{175}\mathrm{Yb}^+$ (b) with branching ratios. Spectroscopic data taken from [21].

3.1.1 $^{172}\mathrm{Yb}^+$

The transition $^1\mathrm{S}_{1/2} \rightarrow {}^2\mathrm{P}_{1/2}$ at $\lambda_{370} \approx 370\,\mathrm{nm}$ in $^{172}\mathrm{Yb}^+$ is used for sympathetic Doppler cooling (see Fig. 3.1 b)). It has a natural linewidth of $\Gamma_{370}/(2\pi) = 19.6\,\mathrm{MHz}$ and is addressed by 3 beams named H1, H2 and V as shown in Fig. 3.2 of the next section. Since the $^2\mathrm{P}_{1/2}$ excited state decays with a probability of $\approx 0.7\%$ to the long lived $^2\mathrm{D}_{3/2}$ state, it is necessary to create an alternative decay channel. This is done by a repumping beam at $\lambda_{\mathrm{repump}} \approx 935\mathrm{nm}$ which drives the $^2\mathrm{D}_{3/2} \rightarrow {}^3[3/2]_{1/2}$ transition, whose excited state then decays with a probability of 98% back to the ground state.

3.1.2 $^{115}\mathrm{In}^+$

A reduced level scheme is shown in Fig. 3.1 a). The clock transition is the highly forbidden $^1\mathrm{S}_0 \rightarrow {}^3\mathrm{P}_0$ transition at $\lambda_{\mathrm{clock}} \approx 236.5\,\mathrm{nm}$ with a narrow natural linewidth of $\Gamma_{\mathrm{clock}}/(2\pi) = 820\,\mathrm{mHz}$. In principle, the clock transition is forbidden in all multipole orders. But since $^{115}\mathrm{In}$ has a nuclear spin $I = 9/2$, there is weak magnetic dipole hyperfine coupling between the excited state $^3\mathrm{P}_0$ and neighboring states $^3\mathrm{P}_1$ and $^1\mathrm{P}_1$. This coupling leads to a non-vanishing electric dipole moment between the two clock states $^1\mathrm{S}_0$ and $^3\mathrm{P}_0$ and an excited state lifetime $\tau_{\mathrm{life}}(^3\mathrm{P}_0) = 0.195(8)\,\mathrm{s}$ [38, 39]. The half integer nuclear spin also introduces a 1st order Zeeman shift sensitivity (see subsection 2.3.3) of the clock transitions. As the ground and excited state are $J = 0$ states, there will be one $F = J + I = 9/2$ hyperfine state for each clock state and hence no insensitive $m_F = 0$ Zeeman substates. To cancel the 1st order Zeeman shift, both stretched state (clock) $\pi-$transitions $|^1\mathrm{S}_0, m_{F,g} = \pm 9/2\rangle \rightarrow |^3\mathrm{P}_0, m_{F,e} = \pm 9/2\rangle$ are probed in the presence of a bias magnetic field $\mathbf{B}$ and the corresponding transition frequencies are averaged. This scheme is presented in 4.1.1.
To detect whether the indium ion is in the ground or excited state of the clock transition and also to prepare it in the extremal substates $|^1\mathrm{S}_0, m_{F,g} = \pm 9/2\rangle$ before the clock interrogation,

the detection transition $^1\mathrm{S}_0 \rightarrow {}^3\mathrm{P}_1$ at $\lambda_{230} \approx 230.6\,\mathrm{nm}$ with $\Gamma_{230}/(2\pi) = 360\,\mathrm{kHz}$ is used. The detection is done with the electron shelving technique [40]. When the ion is in either of the $|^1\mathrm{S}_0, m_{F,g} = \pm 9/2\rangle$ states, fluorescence is observable on the closed $|^1\mathrm{S}_0, m_{F,g} = \pm 9/2\rangle \rightarrow |^3\mathrm{P}_1, m_{F,e} = \pm 11/2\rangle$ stretched state transition. When the ion is in the excited state, it remains dark. To drive these $\Delta m_F = \pm 1$ $\sigma^{\pm}-$transitions, the detection light needs do be circularly polarized with respect to $\mathbf{B}$, using an electro optical modulator (EOM). By switching between right and left handed circular polarization, the ion can be optically pumped from one extremal $m_{F,g} = \pm 9/2$ state to the other $m_{F,g} = \mp 9/2$.

3.2 Ion trap setup

Since the experimental setup is well documented in e.g. [21, 41–45], this section only gives a short overview over selected parts of relevance for this thesis. A reduced schematic of the ion trap setup including all relevant components is shown in Fig. 3.2.

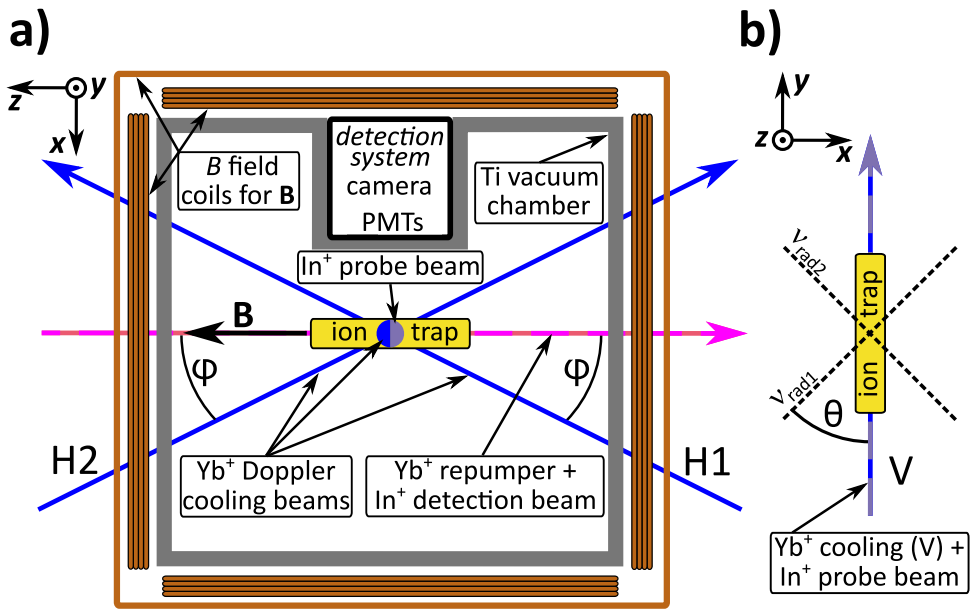

Figure 3.2 Reduced experimental ion trap setup. a) $xz-$plane and b) $xy-$plane.

3.2.1 Ion trap

To trap both indium and ytterbium ions in a linear Coulomb crystal, a segmented linear Paul trap is used [41]. The trap is designed especially for clock operation and features e.g. low heating rates as presented in section 5.1.3. It consists of four stacked gold coated aluminium nitride chips and has eight trapping segments. The trap axis is aligned parallel to the $z-$axis, as is the bias magnetic field $\mathbf{B}$, see Fig. 3.2 a), the radial trap axes thus lie in the $xy-$plane (Fig. 3.2 b)). Besides the electrodes for the axial and radial confinement shown schematically in Fig. 2.3, there are two additional dc-electrodes in each segment which allow to manipulate the orientation of the radial trap axes with respect to the $y-$axis [41]. The orientation is described by the angle θ. The influence of θ on sympathetic cooling will be analyzed in chapter 5.

3.2.2 Chamber and magnetic field coils

To isolate the ions from the environment and to reduce collisions with background gas molecules which result in unwanted heating, the ion trap is mounted inside a vacuum chamber in ultra high vacuum (UHV) at a pressure $p_{\mathrm{vac}} \approx 10^{-11}\,\mathrm{mbar}$. The chamber is made of titanium to avoid magnetization and hence to reduce unwanted magnetic stray fields. To produce the bias

magnetic field **B** and to compensate for residual magnetic stray fields, three orthogonal pairs of Helmholtz coils are used (see Fig. 3.2 a)).

3.2.3 Laser setup

The clock laser used to probe the indium ion is a Nd:YAG solid state laser at $4\lambda_{\text{clock}} \approx 946\,\text{nm}$. The laser beam is frequency quadrupled by two second harmonic generation (SHG) stages to produce resonant probe light at $\lambda_{\text{clock}} \approx 236.5\,\text{nm}$ [46]. To ensure long coherent interrogation times, the laser is stabilized to a 30 cm ultra low expansion (ULE) cavity at room temperature and can optionally be transfer locked to the cryogenic silicon cavity at PTB [47]. The probe beam is aligned parallel to the $y-$axis (see 3.2 b)) and has no projection onto the trap axis (and the corresponding normal modes). The resulting orthogonality to **B** is necessary to address both stretched state clock ($\pi-$)transitions.
To produce the indium detection light at $\lambda_{230} \approx 230.6\,\text{nm}$, light of an external cavity diode laser (ECDL) at $4\lambda_{230} \approx 922\,\text{nm}$ is frequency quadrupled by two SHG stages. As the clock laser, the ECDL is stabilized to a (second) 30 cm ULE cavity. To create left or right handed circularly polarized light with respect to **B**, an EOM is used. The EOM allows to switch the polarization within short times as required for clock operation. The resulting circularly polarized indium detection beam is aligned anti parallel to **B** (see Fig. 3.2 a)) as required to address $\sigma^{\pm}-$transitions. For further detailed information on the detection laser setup, see [43].
The ytterbium Doppler cooling laser at $\lambda_{370} \approx 370\,\text{nm}$ and the repumping laser at $\lambda_{\text{repump}} \approx$ 935nm are commercial systems and stabilized using a wavemeter lock.
While there is a single rempumping beam parallel to the $z-$axis, there are three ytterbium Doppler cooling beams. Two of these beams, named horizontal 1 (H1) and horizontal 2 (H2), lie in the $xz-$plane and have an angle of $\varphi \approx \pm 23°$ relative to the $z-$axis (see Fig. 3.2 a)). The third, vertical, beam (V) is directed parallel to the $y-$axis. As it is relevant for section 3.3 and chapter 5, H1 and V have a fixed power ratio $P_{\text{H1}}/P_{\text{V}} = 0.1$. Both beams are sampled from a single beam using a polarizing beam splitter (PBS), the power ratio is set by a $\lambda/2-$wave plate. Furthermore, both beams have a fixed ratio $s_{\text{H1}}/s_{\text{V}} \approx 0.3$ between the saturation coefficients s_{H1} and s_{V}. When both beams are switched on simultaneously, the total saturation coefficient of the ytterbium ions $s_{\text{eff}} = s_{\text{H1}} + s_{\text{V}}$.[2] The fixed saturation ratio results from the fixed power ratio between both beams and different saturation powers $P_{\text{sat,V/H1}}$. Here $P_{\text{sat,V/H1}}$ is the power of each laser needed to reach a saturation of $s = 1$. The saturation powers were measured to be $P_{\text{sat,V}} \approx 20.7\,\mu\text{W}$ and $P_{\text{sat,H1}} \approx 7.2\,\mu\text{W}$ [49]. Therefore, the ratio becomes

$$\frac{s_{\text{H1}}}{s_{\text{V}}} = \frac{P_{\text{H1}}}{P_{\text{V}}} \times \frac{P_{\text{sat,V}}}{P_{\text{sat,H1}}} = \frac{1}{10} \times \frac{20.7}{7.2} \approx 0.3. \tag{3.1}$$

H1 and V are the main cooling beams, H2 is solely used for specific purposes within the spectroscopic sequence as will be presented in the next section 3.3.

3.2.4 Detection system

To detect the fluorescence of indium and ytterbium, a detection system comprised of a lens system, photo multiplier tubes (PMT, one for indium, one for ytterbium) and an EMCCD camera is used (shown schematically in Fig. 3.2a)). The camera allows to analyze the crystal configuration within the spectroscopic sequence, meaning the order of species in the linear chain. The PMTs are used to analyze the amount of scattered photons on the ytterbium Doppler cooling and indium detection transition. The EMCCD camera is the key element of the indium state detection, because it allows to evaluate individual scattering rates of all ions in the crystal. This is a necessary feature for multi-ion clock operation. By setting a threshold count rate, the indium

[2] Since the saturation coefficient $s \propto I$, individual saturation coefficients add up [48].

ion is detected dark (in the $^3P_0$ excited state, measured camera count rate below threshold) or bright (in the $^1S_0$ ground state, count rate above threshold). The detection system is presented by T. Nordmann et al. in [44].

3.3 Clock sequence for the spring 2022 clock campaign

During the 2022 spring campaign, a single indium ion was trapped together with three ytterbium ions in the configuration (Yb-In-Yb-Yb/Yb-Yb-In-Yb) (mirror images of a configuration yield the same mode structure and are therefore equivalent). Since every interrogation of the indium ion and following detection yields a binary information ($|e\rangle$, ion appears dark or $|g\rangle$, observable fluorescence on the detection transition), the measurement needs to be repeated multiple times to evaluate an excitation probability $p \equiv |c_e|^2$. p is approximated by the fraction

$$p \approx \frac{n_{\text{dark}}}{N_{\text{total}}}, \tag{3.2}$$

where n_{dark} is the number of measurements the indium ion is found in $|e\rangle$ and N_{total} is the total number of measurements. N_{total} is usually on the order of 10 (locking) or 100 (transition scans and Rabi flops).

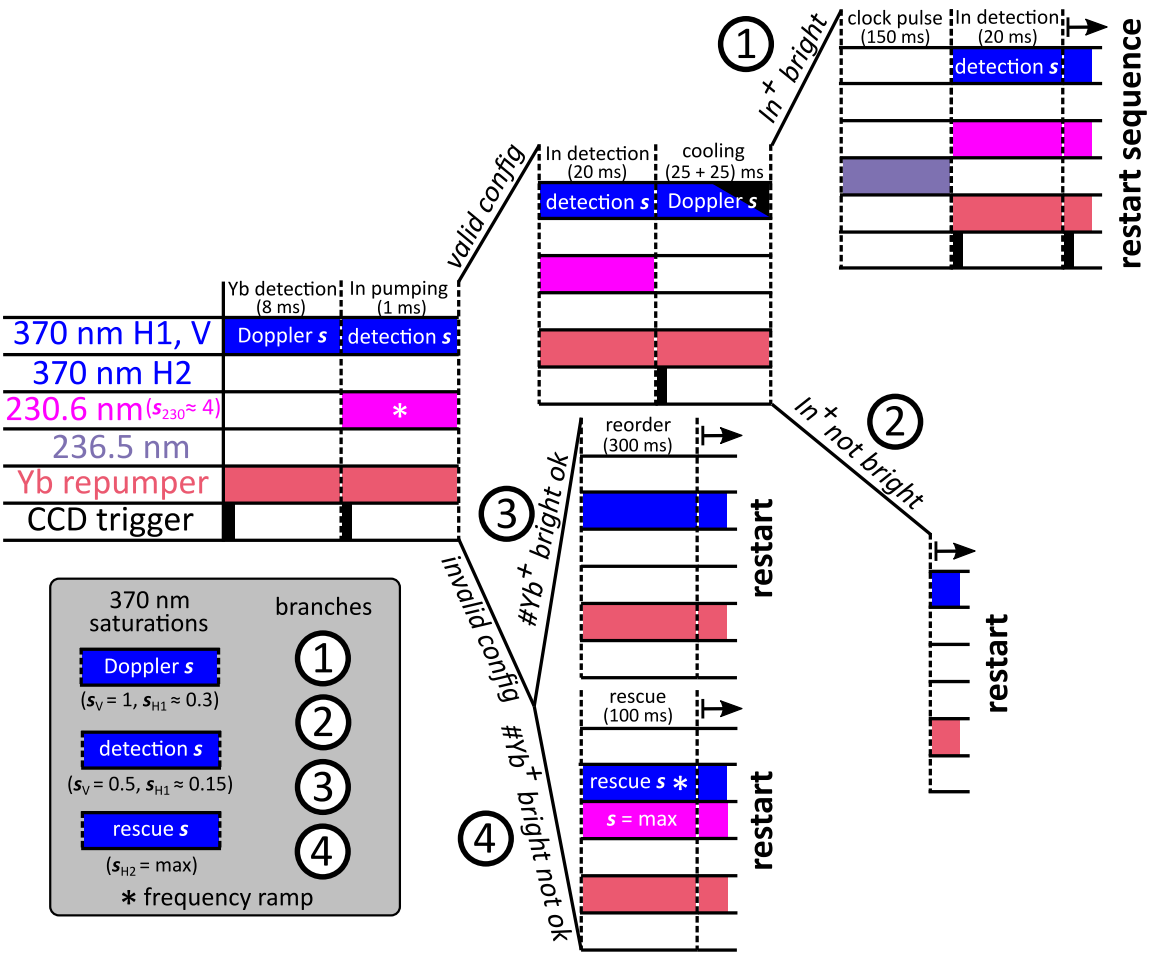

Figure 3.3 Clock spectroscopy sequence used in the spring 2022 clock campaign.

This section presents the Clock spectroscopy sequence used during the spring clock campaign to probe the clock ion and to evaluate p. The clock sequence consists of four branches as shown in Fig. 3.3. Which branch is used depends on specific decisions which are made during the sequence. Since every phase requires exact timing, the complete sequence is controlled by an

FPGA. Each branch and the corresponding phases are explained in the following.

Independent of the branch, the sequence starts with an 8 ms ytterbium detection. In this phase, the Doppler cooling beams H1 and V are switched on simultaneously at saturations $s_{\mathrm{V}} = 1$ and $s_{\mathrm{H1}} \approx 0.3 s_{\mathrm{V}}$. Due to the fixed ratio $s_{\mathrm{H1}}/s_{\mathrm{V}}$, only the saturation s_{V} is mentioned in the following. Along with the Doppler cooling beams, the repumping beam is always switched on. In this detection phase, a reference image of the whole Coulomb crystal is taken using the EMCCD camera for the following reason: Collisions with background gas molecules can lead to heating of the crystal. As a result, the configuration can change (wrong order within the linear chain), molecular ions can form (e.g. YbH^+) which appear dark, the crystal melts (not crystallized in a linear chain, appears dark) or ions are "kicked" out of the trapping potential. These cases need to be detected as they require special actions which are described below. In the next phase, the indium ion is optically pumped for 1 ms in either of the extremal Zeeman states $m_{F,g} = \pm 9/2$ using the indium detection transition and circularly polarized light at λ_{230}. The saturation coefficient of the indium detection beam is $s_{230} \approx 4$, s_{V} is lowered to $s_{\mathrm{V}} = 0.5$. To account for the Zeeman shift of the $m_{F,g/e}$ substates of the detection transition, the laser frequency is ramped. In parallel to the optical pumping phase, the ytterbium reference image is evaluated. If the configuration is valid, e.g. in Yb-In-Yb-Yb or its mirror image, the next phase is a 20 ms indium detection. In this phase, an image of the indium ion is taken. This phase ensures that the indium ion appears bright and is hence in the ground state. If it appears dark, the ion is either in the excited state (not decayed back into $|g\rangle$ after the last clock interrogation) or a collision happened. After the indium detection, the 50 ms sympathetic Doppler cooling phase starts with $s_{\mathrm{V}} = 1$. The phase consists of two sub-phases, 25 ms where s_{V} is held constant (named constant s phase), and afterwards 25 ms where s_{V} is ramped down linearly to 0 (named ramped s phase). The idea behind the saturation ramp is a further reduction of the temperature due to the saturation dependence of the end temperature of the cooling process (as will be subject of chapter 5). In parallel to the cooling phase, the indium reference image is evaluated. If the ion appears bright, it is prepared in $|g\rangle$ and the clock transition can be probed in the next phase. During the $\tau_{\mathrm{probe}} = 150$ ms clock pulse, all laser beams except for the probe beam at λ_{clock} are blocked by mechanical shutters. This is done to avoid additional ac-Stark shifts of the clock transition. The residual ac-Stark shift due to the probe beam will be subject of chapter 4. In addition, due to the low heating rates of the ion trap, it is not necessary to do laser cooling during the pulse. After the clock pulse, the clock states are read out in a 20 ms indium detection. This completes branch 1. The result of the indium detection is recorded (either n_{dark} or n_{bright} and N_{total} is increased by 1) and the sequence starts from the beginning.

The branch 2 accounts for the case, that in the first Indium detection, the indium ion appeared dark. Therefore, the clock transition is not probed and the sequence restarts.

Branches 3 and 4 account for the case that during the ytterbium detection phase, an invalid configuration was detected. Invalid configuration means either of the above mentioned consequences of a collision. When all ytterbium ions appear bright in the reference image, the configuration changed and the crystal is reordered to the desired configuration. In addition, since these cases indicate an increased, suboptimal clock ion temperature, the binary result of the previous clock interrogation will be neglected in the evaluation of p. In the following 300 ms reordering phase, H1 and V are switched off, H2 is switched on at maximum saturation s_{H2}. The reordering process is documented in [42] and presented by T. Nordmann et al. in [50]. This ends branch 3.

If an invalid configuration is detected and in addition, at least one ytterbium ion appears dark, the 100 ms rescue phase starts. Here H1 and V are switched off, H2 is switched on at max-

imum saturation and its frequency is ramped to account for high ion temperatures and hence high 1st order Doppler shifts (see Eq. 2.28). In addition, the indium detection beam is switched on at maximum saturation s_{230} to account for the case of molecular ion formation. Due to its high photon energies $\hbar\omega_{230}$, the indium detection beam can dissociate molecular bonds. The rescue phase ends branch 4, and hence completes the clock sequence.

From branch 1, which uses a total time of $t_{\text{branch1}} = t_{\text{d}} + \tau_{\text{probe}} = 249\,\text{ms}$ with a dead time $t_d = 99\,\text{ms}$, a duty cycle of

$$\frac{\tau_{\text{probe}}}{t_{\text{branch1}}} \approx 0.6 \tag{3.3}$$

is obtained. This duty cycle needs to be seen as a lower limit, since branches 2-4 do not lead to a clock interrogation and therefore add dead time.
The clock sequence will be modeled, analyzed and optimized regarding the ion temperatures in chapter 5.

4 Analysis of probe field induced ac-Stark shifts

The ac-Stark shift results from non-resonant interaction of the probe field with the electric dipole moment of the clock ions. This interaction then leads to energy shifts of the atomic levels and hence a frequency shift of the clock transition. Therefore, a thorough analysis is necessary for precise atomic clocks. In this chapter, the analysis of probe field induced ac-Stark shifts for the $^{115}\mathrm{In}^+$ clock at PTB are presented. The chapter is structured as follows. In 4.1, a yet unconsidered contribution to the ac-Stark shift is analyzed. The section is based on the investigation of V. I. Yudin et al. in [18]. In 4.2, the ac-Stark shift by far off-resonant transitions is determined. Finally, in 4.3 the total probe field induced ac-Stark shift is evaluated followed by a summary of the results of this chapter in 4.4.

4.1 Probe field ellipticity-induced ac-Stark Shift

This section presents the results of the analysis of the probe field ellipticity induced ac-Stark shift. At first, 4.1.1 gives a derivation of the shift as presented by Yudin et al. [18]. In 4.1.2, experimental imperfections are estimated to do a first comparative analysis of the magnitude of the shift for different clock species, which is done in 4.1.3. Lastly, in 4.1.4 and 4.1.5 the shift is determined for the $^{115}\mathrm{In}^+$ clock at PTB based on clock spectroscopy of the relevant transitions.

4.1.1 Theoretical background

In [18] V. I. Yudin et al. have presented a yet unconsidered contribution to the ac-Stark shift which occurs especially in atomic lattice and ion clocks based on the highly forbidden $^1\mathrm{S}_0 \rightarrow {}^3\mathrm{P}_0$. The authors have shown that the shift originates from the presence of an uncontrolled elliptical polarization of the probe field as well a misalignment of the applied bias magnetic field. Besides $^{115}\mathrm{In}^+$, further examples of clocks using this transition are $^{87}\mathrm{Sr}$ and $^{171}\mathrm{Yb}$ lattice clocks as well as $^{27}\mathrm{Al}^+$ ion clocks. All the mentioned clock species feature a half integer nuclear spin I, which, as mentioned in section 3.1, introduces a 1st order Zeeman shift sensitivity due to missing $|m_F = 0\rangle$ substates in the $F = I$ manifolds of the $^1\mathrm{S}_0$ ground and $^3\mathrm{P}_0$ excited state. The common solution to circumvent the 1st order Zeeman shift sensitivity is by probing both stretched state (clock) transitions $|F, m_{F,g} = \pm F\rangle \rightarrow |F, m_{F,e} = \pm F\rangle$ in the presence of a bias magnetic field $\mathbf{B}$ and averaging their respective transition frequencies ω_{-F-F} and ω_{+F+F}. Due to the magnetic field, the energies of the ground and excited Zeeman substates are shifted by

$$\Delta E_{1\mathrm{Z},g} = g_g \mu_B m_{F,g} B \tag{4.1}$$

$$\Delta E_{1\mathrm{Z},e} = g_e \mu_B m_{F,e} B \tag{4.2}$$

where μ_B is the Bohr magneton, $g_{g/e}$ the ground and excited state $g-$ factors and $B = |\mathbf{B}|$ (see e.g. [25]). The energy shift is shown schematically in Fig. 4.1 for a model species with positive g_g and g_e, which can be seen by a downwards shift of Zeeman substates with negative projection m_F.

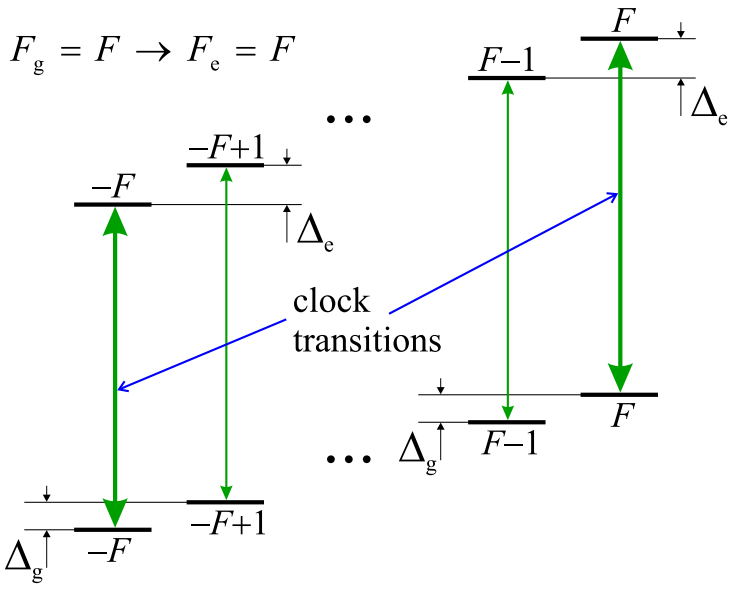

Figure 4.1 Clock transition Zeeman structure in the presence of a bias magnetic field $\mathbf{B}$. Due to the 1st order Zeeman shift, the substates with projections $m_{F,g/e} = \{-F, -F+1, ..., F-1, F\}$ are split by the energy difference $\hbar\Delta_{g/e}$. To cancel the shift, both clock transitions (i.e. $|m_{F,g} = \pm F\rangle \rightarrow |m_{F,e} = \pm F\rangle$, shown as bold green arrows) are probed and their respective frequencies ω_{+F+F} and ω_{-F-F} are averaged. Figure taken with permission of V. I. Yudin from [18].

This energy shift results in a frequency shift of both clock transition frequencies ω_{-F-F} and ω_{+F+F}

$$\omega_{-F-F} = \omega_0 - (\Delta_e - \Delta_g)F \tag{4.3}$$
$$\omega_{+F+F} = \omega_0 + (\Delta_e - \Delta_g)F, \tag{4.4}$$

where ω_0 is the unperturbed transition frequency for a vanishing magnetic field $\mathbf{B}$ and Δ_g and Δ_e are defined as

$$\Delta_g = \frac{\Delta E_{1Z,g}}{m_{F,g}\hbar} = \frac{g_g \mu_B B}{\hbar} \tag{4.5}$$
$$\Delta_e = \frac{\Delta E_{1Z,e}}{m_{F,e}\hbar} = \frac{g_e \mu_B B}{\hbar}. \tag{4.6}$$

From Eqs. 4.3 and 4.4 it can be seen that for both stretched state transitions the 1st order Zeeman shift is equal in magnitude but opposite in sign. Therefore, when taking the average of ω_{-F-F} and ω_{-F-F}

$$\frac{\omega_{-F-F} + \omega_{+F+F}}{2} = \frac{\omega_0 - (\Delta_e - \Delta_g)F + \omega_0 + (\Delta_e - \Delta_g)F}{2} = \omega_0 \tag{4.7}$$

the resulting frequency is equal to the unperturbed transition frequency and hence free of the 1st order Zeeman shift.
This picture only holds under perfect experimental conditions, where the probe field $\mathbf{E}_{\text{probe}}$ is linearly polarized and $\mathbf{B}$ is oriented parallel to $\mathbf{E}_{\text{probe}}$, such that only $\Delta m_F = 0$ $\pi-$transitions are driven. Under real experimental conditions, the electric field polarization as well as the magnetic field orientation are not perfectly controllable. As shown in Fig. 4.2 a), these experimental imperfections can lead to a certain degree of ellipticity of the probe field, described by the polarization unit vector $\mathbf{a}$. The ellipticity of $\mathbf{a}$ can be represented using the angular parameter ϵ by

$$\mathbf{a} = \cos(\epsilon)\mathbf{e}'_x + i\sin(\epsilon)\mathbf{e}'_y, \tag{4.8}$$

where $\mathbf{e}'_{x,y}$ are the unit basis vectors of the 2D Cartesian coordinate system pointing along the principal axes of the polarization ellipse (shown in red). Moreover, as shown Fig. 4.2 a) and b), the magnetic field can have a misorientation with respect to the main axis of the polarization ellipse (parallel to $\mathbf{e}'_x$) described by the angles φ and ξ. Here $\xi = \angle(\mathbf{e}'_x, \mathbf{n}_\mathrm{B}^{(\mathrm{ell})})$ with $\mathbf{n}_\mathrm{B}^{(\mathrm{ell})}$ the projection of $\mathbf{n}_\mathrm{B} = \mathbf{B}/B$ onto the $x'y'-$plane.

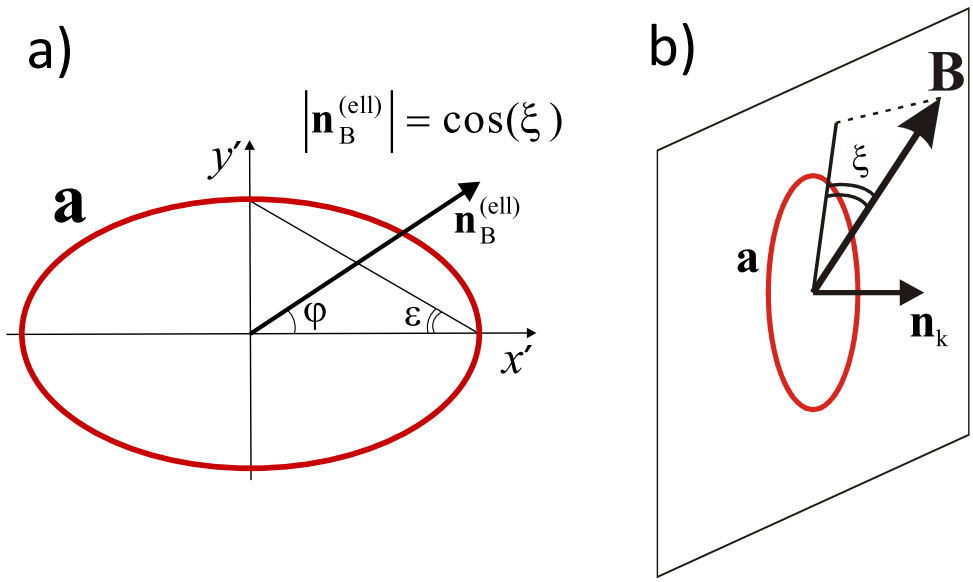

Figure 4.2 Probe field ellipticity as result of experimental imperfections. a) An elliptical polarization of the probe field $\mathbf{E}_\mathrm{probe}$ is described by the polarization unit vector $\mathbf{a}$ where the angle ϵ in the polarization ellipse (red) is a measure for the amount of ellipticity. b) Besides an elliptical polarization, experimental imperfections can result in a misorientation of the bias magnetic field $\mathbf{B}$ with respect to the $x'y'-$plane (see a)) and the $x'-$axis described by the angles ξ and φ respectively.

Assuming a certain degree of ellipticity and an arbitrary orientation of $\mathbf{B}$, $\mathbf{E}_\mathrm{probe}$ can be expressed as

$$\mathbf{E}_\mathrm{probe}(t) = \Re(E_\mathrm{probe} e^{-i\omega_\mathrm{probe}} \mathbf{a}) = \frac{E_\mathrm{probe} e^{-i\omega_\mathrm{probe}} \mathbf{a} + c.c.}{2} \tag{4.9}$$

where ω_probe is the probe field angular frequency (usually close to ω_0) and $E_\mathrm{probe} = |\mathbf{E}_\mathrm{probe}|$. Here it is convenient to define $\mathbf{a}$ in a different basis such that

$$\mathbf{a} = \sum_{q=0,\pm1} a^{(q)} \mathbf{e}_q \tag{4.10}$$

where $\mathbf{e}_0 = \mathbf{e}_z$, $\mathbf{e}_\pm = \mp(\mathbf{e}_x \pm i\mathbf{e}_y)$, with the unit basis vectors $\mathbf{e}_{x,y,z}$ of the 3D Cartesian coordinate system.
Since there is now a circular component in the probe field as well as a small projection of the magnetic field onto the direction $\mathbf{n}_\mathrm{k}$ of the probe laser $k-$vector, there is coupling between the clock transition's extremal substates ($|\,|m_F| = F\rangle$) and neighboring substates $|\,|m_F| = F-1\rangle$ as highlighted by red arrows in Fig. 4.3.

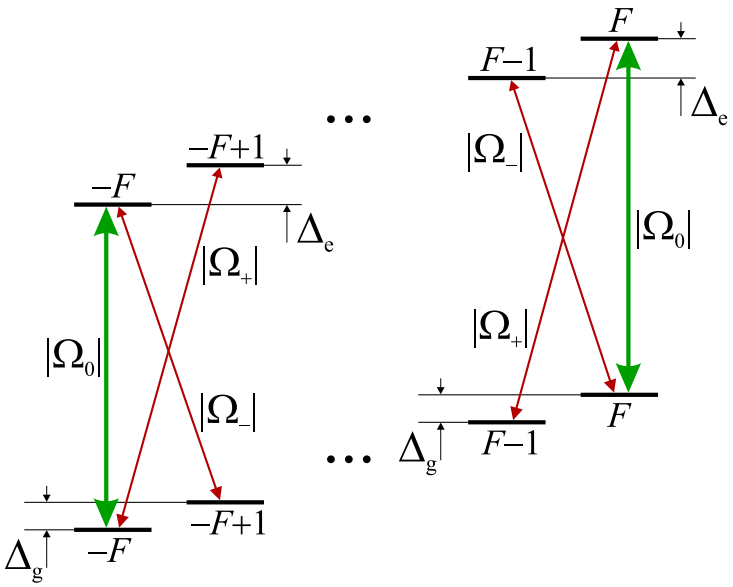

Figure 4.3 Clock transition Zeeman structure in the presence of experimental imperfections. Due to a certain degree of ellipticity of the probe field, besides the coupling between the extremal Zeeman substates $||m_{F,g/e}|= F\rangle$ described by the clock transition Rabi frequency $|\Omega_0|$, there is now coupling to the neighboring $||m_{F,g/e}|= F-1\rangle$ states described by the $\sigma^{\pm}-$transition Rabi frequencies $|\Omega_{\pm}|$. The $\sigma^{+}-$ and $\sigma^{-}-$ transitions (corresponding to $|\Omega_{+}|$ and $|\Omega_{+}|$ respectively) are shown by the thin red arrows. Figure taken with permission of V. I. Yudin from [18].

The coupling to the neighboring substates is described by the two $\sigma-$transition Rabi frequencies $|\Omega_{\pm}|$ whose absolute values are defined by

$$|\Omega_{\pm}|= \frac{|d_{eg,F}E_{\text{probe}}a^{(\pm 1)}|}{\hbar}\underbrace{\frac{1}{\sqrt{F+1}}}_{:=c_{\text{CG},\pm}}, \tag{4.11}$$

while the coupling between the extremal substates is described by the clock transition Rabi frequency $|\Omega_0|$ with

$$|\Omega_0|= \frac{|d_{eg,F}E_{\text{probe}}a^{(0)}|}{\hbar}\underbrace{\frac{\sqrt{F}}{\sqrt{F+1}}}_{:=c_{\text{CG},0}}. \tag{4.12}$$

Here $d_{eg,F} = \langle F_g||d||F_e\rangle$ is the reduced dipole matrix element of the clock transition and the factors including the total angular momentum F are the respective Clebsch-Gordan coefficients $c_{\text{CG},0/\pm}$.
Due to the coupling $|\Omega_{\pm}|$, both clock transition frequencies ω_{-F-F} and ω_{+F+F} are affected by individual ac-Stark shifts δ_{-F-F} and δ_{+F+F} according to

$$\omega_{-F-F} = \omega_0 - \overbrace{(\Delta_e - \Delta_g)F} + \overbrace{\delta_{-F-F}} \tag{4.13}$$

$$\omega_{+F+F} = \omega_0 + \underbrace{(\Delta_e - \Delta_g)F}_{\text{Zeeman}} + \underbrace{\delta_{+F+F}}_{\text{ac-Stark}} \tag{4.14}$$

where the ac-Stark shifts are given by

$$\delta_{-F-F} = \frac{|\Omega_+|^2}{4\Delta_e} - \frac{|\Omega_-|^2}{4\Delta_g} \tag{4.15}$$

$$\delta_{+F+F} = \frac{|\Omega_+|^2}{4\Delta_g} - \frac{|\Omega_-|^2}{4\Delta_e}, \tag{4.16}$$

which holds for $|\Delta_{e,g}| \gg |\Omega_\pm|$. When both transition frequencies in Eqs. 4.13 and 4.14 are again averaged

$$\frac{\omega_{-F-F} + \omega_{+F+F}}{2} = \omega_0 + \delta_{\mathrm{ac}}^{(\mathrm{el-ind})}, \tag{4.17}$$

one can see that there is an additional term $\delta_{\mathrm{ac}}^{(\mathrm{el-ind})}$ to the unperturbed transition frequency ω_0 which Yudin et al. call, due to its origin, the ellipticity induced shift. It is given by

$$\begin{aligned} \delta_{\mathrm{ac}}^{(\mathrm{el-ind})} &= \frac{\delta_{-F-F} + \delta_{+F+F}}{2} \\ &= \frac{\Delta_g + \Delta_e}{8\Delta_g\Delta_e}(|\Omega_+|^2 + |\Omega_-|^2). \end{aligned} \tag{4.18}$$

Because usually $|\Omega_\pm| \ll |\Omega_0|$ (as will be shown in section 4.1.4) and $|\Omega_0|$ typically being the more easily accessible quantity, it is convenient to express $\delta_{\mathrm{ac}}^{(\mathrm{el-ind})}$ in terms of $|\Omega_0|$. Using Eqs. 4.11 and 4.12, the right hand side of Eq. 4.18 can be rewritten as

$$\delta_{\mathrm{ac}}^{(\mathrm{el-ind})} = |\Omega_0|^2 \frac{\Delta_g + \Delta_e}{8F\Delta_g\Delta_e} \frac{|a^{(+1)}|^2 - |a^{(-1)}|^2}{|a^{(0)}|^2}. \tag{4.19}$$

Now the factor including the components $a^{(\pm 1;0)}$ can be expressed in vector notation as

$$\frac{|a^{(+1)}|^2 - |a^{(-1)}|^2}{|a^{(0)}|^2} = \frac{i([\mathbf{a} \times \mathbf{a}^*] \cdot \mathbf{n}_{\mathrm{B}})}{|\mathbf{a} \cdot \mathbf{n}_{\mathrm{B}}|^2} \tag{4.20}$$

where $\times$ and $\cdot$ denote the vector and scalar product of two vectors. It can be shown further that

$$i([\mathbf{a} \times \mathbf{a}^*] \cdot \mathbf{n}_{\mathrm{B}}) = \sin(2\epsilon)\sin(\xi) \tag{4.21}$$

such that equation Eq. 4.18 can be written as

$$\delta_{\mathrm{ac}}^{(\mathrm{el-ind})} = |\Omega_0|^2 \frac{\Delta_g + \Delta_e}{8\Delta_g\Delta_e} \frac{\sin(2\epsilon)\sin(\xi)}{|\mathbf{a} \cdot \mathbf{n}_{\mathrm{B}}|^2}. \tag{4.22}$$

Under use of Eqs. 4.5 and 4.6, the absolute of $\delta_{\mathrm{ac}}^{(\mathrm{el-ind})}$ can be expressed as

$$|\delta_{\mathrm{ac}}^{(\mathrm{el-ind})}| = \frac{|\Omega_0|^2}{\Delta_Z} \frac{|\Delta_g^2 - \Delta_e^2|}{8F|\Delta_g\Delta_e|} \frac{|\sin(2\epsilon)\sin(\xi)|}{|\mathbf{a} \cdot \mathbf{n}_{\mathrm{B}}|^2} \tag{4.23}$$

$$= \frac{|\Omega_0|^2}{\Delta_Z} \frac{|g_g^2 - g_e^2|}{8F|g_g g_e|} \frac{|\sin(2\epsilon)\sin(\xi)|}{|\mathbf{a} \cdot \mathbf{n}_{\mathrm{B}}|^2} \tag{4.24}$$

with $\Delta_Z = |\Delta_g - \Delta_e|$. Finally, under the assumption $|\epsilon, \xi, \varphi| \ll 1$ (which is usually the case in atomic clock experiments), the following small angle approximation can be used

$$\begin{aligned} \sin(2\epsilon) &\approx 2\epsilon \\ \sin(\xi) &\approx \xi \\ |\mathbf{a} \cdot \mathbf{n}_{\mathrm{B}}|^2 &\approx 1 - \epsilon^2 - \varphi^2 - \xi^2 \approx 1, \end{aligned}$$

leading to the final form of the shift presented in [18]

$$|\delta_{\mathrm{ac}}^{(\mathrm{el-ind})}| \approx A \frac{|\Omega_0|^2}{\Delta_Z} |\epsilon\xi|, \tag{4.25}$$

where the parameter A is defined as

$$A = \frac{|g_g^2 - g_e^2|}{4F|g_g g_e|}. \tag{4.26}$$

Having a closer look at Eq. 4.25, the ellipticity induced shift can be separated into two parts. On one hand, there is the parameter A depending on ground and excited state $g-$factors and the total angular momentum $F = I$. Therefore, it is completely determined by atomic properties and hence a feature of the chosen clock species. It can be seen as measure for the species' intrinsic shift sensitivity. The remaining terms $|\Omega_0|^2$, Δ_Z^{-1} and $|\epsilon\xi|$ depend on experimental conditions. While $|\Omega_0|^2$ and Δ_Z can be measured directly during clock operation, experimental imperfections described by the angles ϵ and ξ need a separate analysis. In the next subsection, estimates for ϵ and ξ found in the literature and also experimentally determined are presented.

4.1.2 Estimate of experimental imperfections ϵ and ξ

To find estimates for ϵ and ξ, it is important to understand the mechanisms from which these imperfections originate. As shown in the previous subsection, ξ describes a misorientation of the bias magnetic field $\mathbf{B}$. In most clock setups, $\mathbf{B}$ is produced by three orthogonal pairs of Helmholtz coils (see 3.2). In principle, due to the orthogonality of the coils, the orientation of $\mathbf{B}$ can be chosen freely. In the $^{115}\mathrm{In}^+$ setup, the bias magnetic field $\mathbf{B}_z$ is oriented along the experiment's $z-$axis. A schematic of the vacuum chamber in the indium setup with mounted Helmholtz coils together with the desired orientation of the bias magnetic field $\mathbf{B}_z$ is shown in Fig. 4.4.

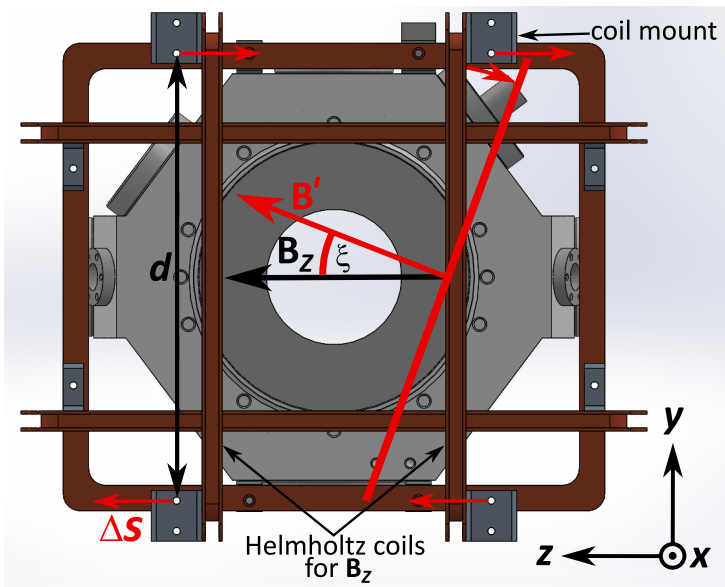

Figure 4.4 Potential magnetic field misorientation due to manufaturing tolerances of Helmholtz coil mounts in the Indium clock setup. The coils (brown) to produce the bias magnetic field $\mathbf{B}_z$ are mounted at the vacuum chamber (grey) by coil mounts (dark grey). Manufacturing tolerances $\Delta s = \pm 2\,\mathrm{mm}$ in the mount positioning can lead to a tilt of the Helmholtz coils (shown by the red tilted bar). This tilt results in a misorientation of $\mathbf{B}_z$ by the angle ϵ with respect to the experiment's $z-$axis. The resulting magnetic field points in the direction of $\mathbf{B}'$. Using Δs and assuming a misplacement of the coil mounts shown by the small red arrows, the worst case misorientation is estimated to be $\epsilon \approx 0.87°$. The technical drawing is used with permission of T. Nordmann.

There are always imperfections in the manufacturing process of, e.g., the positioning of drilled holes for the coil mounts. Here the uncertainty of the desired positions of the drilled holes is given by $\Delta s \approx \pm 2\,\mathrm{mm}$ [49]. Assuming the worst case, the drilled holes of the upper and lower mounts of the coils producing $\mathbf{B}_z$ are horizontally displaced by Δs in opposite directions. This situation is shown schematically in Fig. 4.4 by the small red arrows (not to scale). These

displacements will then lead to a tilt of both coils (shown by the red tilted bar) and hence a tilt of $\mathbf{B}_z$ in the direction of $\mathbf{B}'$. The resulting worst case misorientation ξ can then be calculated using the vertical distance between the drilled holes $d = 264\,\text{mm}$ via

$$\xi = \arctan(\frac{2\Delta s}{d}) \approx \frac{2\Delta s}{d} = \frac{2 \times 2\,\text{mm}}{264\,\text{mm}} \approx 0.0152\,\text{rad}\,(\approx 0.87^\circ). \tag{4.27}$$

Estimates for ξ can also be found in the literature. In [51], Lange et al. present a scheme to suppress second-rank tensor frequency shifts in atomic clocks by rotating the applied bias magnetic field during the dark time of a Ramsey interrogation. The authors give an uncertainty of the desired magnetic field orientation θ of $u(\theta) \equiv \xi = \pm 1^\circ \approx 0.0175\,\text{rad}$. Tan et al. demonstated an even smaller uncertainty of $\xi = u(\theta_0) = 0.4^\circ \approx 0.007\,\text{rad}$ in [52], where the electric quadrupole shift is minimized by aligning the bias magnetic field to a specific angle $\theta_0 \approx 54.7^\circ$. Both publications show that possible uncertainties of the magnetic field orientation are on the order of $\xi \approx 1^\circ$ or $\approx 0.0175\,\text{rad}$. Although Tan et al. demonstrate a smaller uncertainty, such a precise alignment is restricted to the specific angle θ_0 for which the quadrupole shift vanishes. The experimental conditions which Lange et al. face in the presented scheme come closer to the requirements regarding a arbitrarily chosen B-field orientation. Therefore, also taking into account the results of the estimate for misorientation due to manufacturing tolerances in the indium setup $\xi \approx 0.87\,\text{deg}$, for the first analysis of the ellipticity induced shift ξ is estimated to be

$$\xi_{\text{est}} \approx 0.0175\,\text{rad}\,(1^\circ). \tag{4.28}$$

ϵ describes the ellipticity of the polarization vector $\mathbf{a}$ and hence of the probe field. Usually, an elliptical polarization is introduced by propagation of a light wave through birefringent materials. Since both orthogonal components of the incident wave face different refractive indices, the propagation through the material introduces a phase shift ϕ between the two orthogonal components. When $\phi = n\pi$ with $n \in \mathbb{Z}$, the light is linearly polarized, otherwise elliptically or circularly polarized. Elements in atomic clock experiments which show a certain birefringence and hence introduce an unwanted ellipticity are e.g. vacuum windows.
To estimate the impact of vacuum windows on the probe fields polarization, the experimental setup shown in Fig. 4.5 is used.

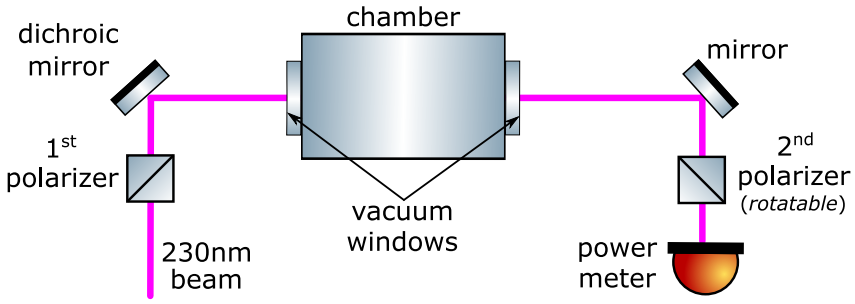

Figure 4.5 Measurement setup to determine ϵ as a result of birefringence in vacuum windows. After passage of the 230 nm beam through the 1st polarizer, its polarization in linear. After passing the two vacuum windows, both orthogonal components of the beam's electric field have acquired a relative phase shift ϕ resulting in an elliptical polarization. The magnitudes of both components are then analyzed using the 2nd rotatable polarizer by measuring minimum (P_{min}) and maximum (P_{max}) transmitted powers. From the ratio of both measured powers, the angle $\epsilon \approx 9.92^\circ$ can be estimated.

For the whole measurement, the In^+ detection beam path is used, since the wavelength λ_{230} is close to the clock laser wavelength at $\lambda_{\text{clock}} \approx 236.5\text{nm}$. Therefore, the impact of birefringent materials on the polarization is comparable for both wavelength. The idea behind this setup is

as follows. Before the beam is reflected to the vacuum windows, it passes the 1st polarizer. This polarizer ensures that the beams polarization is linear, such that every change in polarization can be traced back to the following elements. After passing the dichroic mirror, the two vacuum windows of the chamber and the second mirror in front of 2nd polarizer, the light has acquired a phase ϕ. This phase might lead to a certain degree of elliptical polarization parametrized by ϵ, which is analyzed in the following way. At first, the transmitted power P through the 2nd polarizer is measured using the power meter. By rotating the polarizer around the axis defined by the incident beam, a defined maximum $P_{\max} \propto I_{\max}$ and minimum $P_{\min} \propto I_{\min}$ of the transmitted power can be found, where $I_{\min/\max}$ are the respective minimum and maximum intensities. These powers correspond to the absolute values of the electric field components $|\mathbf{E}_{x'}| \propto \sqrt{I_{\max}}$ and $|\mathbf{E}_{y'}| \propto \sqrt{I_{\min}}$ aligning with the principal axes of the polarization ellipse as shown in Fig. 4.6.

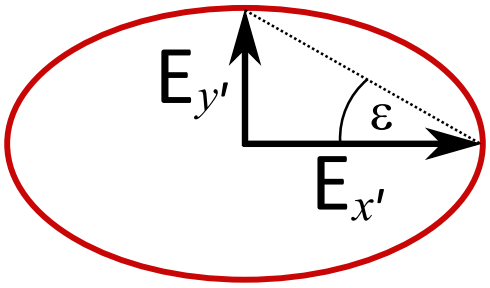

Figure 4.6 Polarization ellipse of the probe field after passage through vacuum windows. The beam's electric field can be decomposed in the two orthogonal component $\mathbf{E}_{x'}$ and $\mathbf{E}_{y'}$. The ellipticity parameter ϵ can then be calculated from the ratio $\mathbf{E}_{x'}/\mathbf{E}_{y'}$ which is determined using the measurement setup shown in Fig. 4.5. Figure by analogy with Fig. 4.2 a), originally taken from [18].

After subtracting a measured background power P_{bg}, the ratio of the minimum and maximum transmitted power, is calculated to be

$$\frac{P_{\min} - P_{\text{bg}}}{P_{\max} - P_{\text{bg}}} = \frac{I_{\min}}{I_{\max}} = \frac{|\mathbf{E}_{y'}|^2}{|\mathbf{E}_{x'}|^2} = 0.030 \pm 0.001, \tag{4.29}$$

where the given ratio is the mean of three power ratio measurements. The uncertainty of 10^{-4} is the observed signal when the measurement is repeated using the two polarizers without any optical element in between. Here an upper bound for the ratio of $\approx 1.6 \times 10^{-4} \ll 0.03$ is found which is sufficiently small compared to the measured ratio given in Eq. 4.29. From Fig. 4.6,

$$\epsilon = \arctan\left(\frac{|\mathbf{E}_{y'}|}{|\mathbf{E}_{x'}|}\right) \approx \frac{|\mathbf{E}_{y'}|}{|\mathbf{E}_{x'}|}. \tag{4.30}$$

The measured power ratio in Eq. 4.29 can be used to determine ϵ

$$\epsilon \approx \sqrt{\frac{|\mathbf{E}_{y'}|}{|\mathbf{E}_{x'}|}} = (0.173 \pm 0.003)\,\text{rad}\,(= (9.92 \pm 0.19)^\circ). \tag{4.31}$$

A similar measurement procedure is used to determine the residual ellipticity produced by an EOM without applied voltage. In the indium setup, an EOM is used to create circularly polarized 230 nm light for the detection of indium and for optical pumping (see 3.2.3). This measurement is of interest, because there are considerations to guide the clock laser overlapped with a 230 nm beam through an EOM. Such a setup could be necessary to employ direct radial laser cooling of indium. During clock interrogation, the EOM would be switched off (i.e. without applied voltage) since there is no indium detection/cooling light needed during the clock

pulse (see Fig. 3.3), but its impact on the clock laser polarization needs to be determined experimentally. The used experimental setup consists of an EOM placed between two polarizers, the measurement is carried out in the same way as for the vacuum windows. Here a power ratio between 1/60 and 1/70 is measured, leading to an angle $\epsilon \approx 0.13\,\mathrm{rad}\,(\approx 7.4°)$.
Experimental estimates for ϵ are also reported in the literature. In [53], Nemitz et al. give an upper bound for the vacuum window induced ellipticity of a 759 nm lattice laser used in a ^{171}Yb lattice clock (clock transition at 578 nm). The authors determine ϵ by comparison of the clock transition Rabi frequency $|\Omega_0|$ and the Rabi frequency $|\Omega_{+/-}|$ of the $\sigma-$transitions (see [53]). This comparison yields $\epsilon \leq 0.024\pi \approx 0.075\,\mathrm{rad}\,(\approx 4.3°)$.
The measurement procedure of Nemitz et al. to determine ϵ is the most significant of the three given estimates, since it analyzes the polarization inside the vacuum chamber at the location of the atoms/ions. In the vacuum window measurement in the indium setup, the polarization is analyzed after passage of the probe beam through two vacuum windows and after reflection at (dichroic) mirrors. Hence the measured angle ϵ is a result of multiple phase shifts by each optical component. In principle, the polarization state inside the chamber is completely unknown. There is the same issue with the EOM measurement, which should rather be seen as an orientation of the device's impact on the polarization in future setups. To make a conservative estimate for ξ, which most likely overestimates than underestimates the probe field ellipticity, the mean of the values found in [53] and determined in the vacuum window measurement for the indium setup are calculated. Therefore, ϵ is estimated to be

$$\epsilon_{\mathrm{est}} = 0.124\,(\approx 7°). \tag{4.32}$$

Since estimates for both experimental imperfections are found (ξ_{est} and ϵ_{est}) the factor $|\epsilon\xi|_{\mathrm{est}}$ needed for a first shift analysis is given by

$$|\epsilon\xi|_{\mathrm{est}} = |\epsilon|_{\mathrm{est}}|\xi|_{\mathrm{est}} \approx 2 \times 10^{-3}. \tag{4.33}$$

To summarize the results, all found estimates for ξ and ϵ are gathered in Tab. 1.

Table 1 Summary of estimates for ξ and ϵ.

angle	in rad	in deg	reference
ξ	0.00152	0.87	this work (manufacturing tolerances)
ξ	0.0175	1	[51]
ξ	0.07	0.4	[52]
ξ_{est}	0.0175	1	
ϵ	0.173	9.92	this work (measurement vacuum windows)
ϵ	0.13	7.4	this work (measurement EOM)
ϵ	0.075	4.3	[53]
ϵ_{est}	0.124	7.1	

As mentioned, all the given values represent just an orientation for the first analysis presented in the next subsection. For the indium setup, a deeper analysis of the factor $|\epsilon\xi|$ based on clock spectroscopy is presented in 4.1.4.

4.1.3 Estimate of the ellipticity induced shift for different clock species

In this subsection, the shift is determined for different optical clocks using the previously found estimate and experimental data found in the literature. For the investigated clock species ^{171}Yb, ^{87}Sr, ^{27}Al$^+$ and ^{115}In$^+$, publications of following experiments are used: Yb lattice clock at NIST [4], Sr lattice clock at JILA [3], Al$^+$ clock at NIST [2] and In$^+$ clock at PTB (Mehlstäubler

group).
As can be seen from Eq. 4.25 and 4.26, besides the clock transition ground and excited state $g-$factors g_g and g_e as well as the nuclear spins $I = F$ for the determination of A, the Rabi frequency $|\Omega_0|$ during Rabi interrogation and the frequency Δ_Z for all clocks need to be found. Using $g-$factor values given in [54–56] and nuclear spins I given in [18], A is calculated [3]. To estimate the respective Rabi frequencies $|\Omega_0|$, the probe times $\tau_{\text{probe,Rabi}}$ during Rabi interrogation given in the referenced publications are used. Here it is assumed, that the probe time corresponds to a $\pi-$pulse such that $|\Omega_0| \approx \pi/\tau_{\text{probe,Rabi}}$. To determine Δ_Z in the In^+ and Al^+ ion clocks, $g-$factors, nuclear spins and Eq. 4.26 are used. For the Sr and Yb lattice clocks, the frequency difference $\Delta_\omega = |\omega_{-F-F} - \omega_{+F+F}|$ between both clock transitions is published in [3] and [4], from which $\Delta_Z = |\Delta_\omega|/(2F)$ can be calculated (see Eqs. 4.3, 4.4 and the definition of Δ_Z). Finally, the shift is calculated using Eq. 4.25 as well as the fractional frequency shift using the clock transition frequencies ν_{clock}(calculated from the clock wavelength λ_{clock} reported in the referenced publications). A summary of all used parameters and calculated shifts as well as used references is given in Tab. 2.

Table 2 Gathered parameters and calculated estimates of the ellipticity induced shift for different clock experiments.

	$^{115}In^+$ (PTB)	$^{27}Al^+$ (NIST)[2]	^{87}Sr (JILA)[3]	^{171}Yb (NIST)[4]
F[18]	9/2	5/2	9/2	1/2
A[18]	0.045[38]	0.209[54]	0.053[55]	0.85[56]
λ_{clock} (nm)	236.5	267	698	578
ν_{clock} (THz)	1267.4	1123.6	429.8	519.0
$\tau_{\text{probe,Rabi}}$ (ms)	150	150	600	560
Ω_0 (s^{-1})	20.9	20.9	5.24	5.61
B (G)	1.07	1.2	0.57	1
Δ_Z (Hz) at B	480[38]	1989[54]	62	399
Δ_Z (Hz) at 1 G	449[38]	1657[54]	108	399
$\lvert\epsilon\xi\rvert$	0.002	0.002	0.002	0.002
$\lvert\delta_{\text{ac}}^{(\text{el-ind})}\rvert$ (μHz)	2.1	2.3	1.1	3.4
$\frac{\lvert\delta_{\text{ac}}^{(\text{el-ind})}\rvert}{\nu_{\text{clock}}}$ (10^{-21})	1.6	2.1	2.9	6.5

In the following, the influence of the respective clock species and experimental parameters as well as the resulting shifts in the investigated experiments are briefly analyzed and compared.
At first, all four species show significant differences in the intrinsic shift sensitivity represented by the parameter A which enters the shift linearly. While the values of In^+ and Sr are on the same order, Al^+ has a ~ 4 times higher sensitivity. A special species regarding the intrinsic sensitivity is Yb whose A parameter is ~ 20 times larger compared to that of In^+. This can be explained by the small value of F, which leads to a high suppression of the clock transitions relative to the $|\Delta m_F| = 1$ $\sigma-$transitions via the Clebsch-Gordan coefficients (as can be seen by comparing the respective Rabi frequencies $|\Omega_0|$ and $|\Omega_\pm|$ in Eqs. 4.12 and 4.11). Moreover, Al^+ shows the largest value of Δ_Z at a given magnetic field, which is advantageous due to $|\delta_{\text{ac}}^{(\text{el-ind})}| \propto \Delta_Z^{-1}$. As it is the case for most frequency shifts, Al^+ and In^+ also profit from high transition frequencies considering the resulting fractional frequency shifts. Regarding experimental parameters, since $|\delta_{\text{ac}}^{(\text{el-ind})}| \propto |\Omega_0|^2 \propto \tau_{\text{probe}}^{-2}$, long interrogation times as used in the Yb and Sr clock experiments are favorable.
The calculated fractional frequency shifts are in the low to mid 10^{-21} region for all considered clock experiments, while the indium clock shows the smallest shift with a fractional value of

[3] The calculated values for A are also published in [18].

1.6×10^{-21}. It is followed by Al^+ (2.1×10^{-21}), Sr (2.9×10^{-21}) and finally Yb with 6.5×10^{-21}. For a comparison of the influence of different clock interrogation schemes the interested reader may consult [18].
In the next subsection, a more precise estimate for $|\epsilon\xi|$ will be determined experimentally by clock spectroscopy. Afterwards, the final evaluation of the shift in the indium clock using the found experimental estimate for $|\epsilon\xi|$ is presented.

4.1.4 Experimental estimate of $|\epsilon\xi|$ for the $^{115}In^+$ clock

In subsection 4.1.2, individual estimates for the angles ϵ and ξ were found. Since these estimates originate from different clock setups and in addition differ from each other by a factor of ≈ 2 in some cases (see Tab. 1), they cannot be used without assuming a proper uncertainty. Therefore, a way to determine an upper bound for the product $|\epsilon\xi|$ based on clock spectroscopy in the $^{115}In^+$ setup is presented in this subsection.
At first, it is necessary to express $|\epsilon\xi|$ in terms of parameters which can be measured experimentally. As shown in subsection 4.1.1, the absolute value of the ellipticity induced shift can be expressed in terms of the clock transition Rabi frequency $|\Omega_0|$ (Eq. 4.25). Since $\Delta_{\mathrm{g/e}} = g_{\mathrm{g/e}}\mu_B B/\hbar$ (Eqs. 4.6 and 4.5), Eq. 4.25 can be written as

$$|\delta_{\mathrm{ac}}^{(\mathrm{el-ind})}| = \frac{|\Delta_{\mathrm{g}}^2 - \Delta_{\mathrm{e}}^2|}{4F|\Delta_{\mathrm{g}}\Delta_{\mathrm{e}}|}\frac{|\Omega_0|^2}{\Delta_Z}|\epsilon\xi| = \frac{|(\Delta_{\mathrm{g}} + \Delta_{\mathrm{e}})(\Delta_{\mathrm{g}} - \Delta_{\mathrm{e}})|}{4F|\Delta_{\mathrm{g}}\Delta_{\mathrm{e}}|}\frac{|\Omega_0|^2}{\Delta_Z}|\epsilon\xi| \tag{4.34}$$

where the binomial theorem was used in the last step. On the other hand, the shift can also be expressed in terms of the $\sigma-$transition Rabi frequencies $|\Omega_\pm|$ by taking the absolute of Eq. 4.18

$$|\delta_{\mathrm{ac}}^{(\mathrm{el-ind})}| = \left|\frac{\Delta_{\mathrm{g}} + \Delta_{\mathrm{e}}}{8\Delta_{\mathrm{g}}\Delta_{\mathrm{e}}}\right| \times ||\Omega_+|^2 - |\Omega_-|^2|. \tag{4.35}$$

From Eqs. 4.34 and 4.35 one can find

$$\left|\frac{\Delta_{\mathrm{g}} + \Delta_{\mathrm{e}}}{8\Delta_{\mathrm{g}}\Delta_{\mathrm{e}}}\right| \times ||\Omega_+|^2 - |\Omega_-|^2| = \frac{|(\Delta_{\mathrm{g}} + \Delta_{\mathrm{e}})(\Delta_{\mathrm{g}} - \Delta_{\mathrm{e}})|}{4F|\Delta_{\mathrm{g}}\Delta_{\mathrm{e}}|}\frac{|\Omega_0|^2}{\Delta_Z}|\epsilon\xi|, \tag{4.36}$$

which can be reduced using $\Delta_Z = |\Delta_{\mathrm{g}} - \Delta_{\mathrm{e}}|$ and expressed as

$$\frac{||\Omega_+|^2 - |\Omega_-|^2|}{2} = \frac{|\Omega_0|^2}{F}|\epsilon\xi| \tag{4.37}$$

$$\Leftrightarrow \frac{||\Omega_+|^2 - |\Omega_-|^2|}{|\Omega_0|^2}\frac{F}{2} = |\epsilon\xi|. \tag{4.38}$$

Thus, $|\epsilon\xi|$ only depends on the clock transition Rabi frequency $|\Omega_0|$ and both $\sigma-$transition Rabi frequencies $|\Omega_\pm|$. All three quantities can be found experimentally by observing Rabi oscillations on the respective transitions.
Such an experiment is carried out as follows. At first, both clock transitions need to be scanned, namely the $|F = 9/2, m_{F,g} = \pm 9/2\rangle \rightarrow |F = 9/2, m_{F,e} = \pm 9/2\rangle$ transitions, which are denoted as $\pi_\pm$ in the following. This is for the determination of $|\Omega_0|$, as well as the bias magnetic field B. The value of the applied field is needed to to calculate the frequencies of the two σ-transitions $|F = 9/2, m_{F,g} = \pm 9/2\rangle \rightarrow |F = 9/2, m_{F,e} = \pm 7/2\rangle$ (denoted as $\sigma^\mp$) with frequencies $\omega_{\sigma\mp}$ relative to the unperturbed clock transition frequency $|\omega_0|$. As shown in subsection 4.1.1, both clock transition frequencies ω_{-F-F} and ω_{+F+F} are affected by the 1st order Zeeman shift due

to the magnetic field (see Eqs. 4.3 and 4.4). From the frequency difference $\Delta_{\nu,\pi}$

$$\begin{aligned}\Delta_{\nu,\pi} &= \frac{\omega_{-F-F} - \omega_{+F+F}}{2\pi} = \nu_{-F-F} - \nu_{+F+F} \\ &= \nu_0 - \frac{\Delta_g - \Delta_e}{2\pi}F - (\nu_0 + \frac{\Delta_g - \Delta_e}{2\pi}F) \\ &= 9(g_g - g_e)\frac{\mu_B B}{h} \end{aligned} \tag{4.39}$$

with $F = 9/2$ and $\nu_0 = \omega_0/(2\pi)$, the magnetic field B can be directly calculated via

$$B = \frac{\Delta_{\nu,\pi} h}{9(g_g - g_e)\mu_B}. \tag{4.40}$$

For the determination of $\Delta_{\nu,\pi}$ line scans of both π-transitions are done with a probe field intensity I_{low} leading to a π-pulse time of $\tau_{\text{pulse}} \approx 150\,\text{ms}$. Afterwards, both line scans are fitted with the fit function

$$f(\nu) = a \times \text{sinc}(b(\nu - \nu_0))^2 \tag{4.41}$$

where a, b and ν_0 (the center frequency) are free fit parameters. Since the two center frequencies ν_{-F-F} and ν_{+F+F} are now found, their frequency difference is calculated to be $\Delta_{\nu,\pi} \approx (4298.30 \pm 0.18)\,\text{Hz}$ (uncertainty from fitting). Figure 4.7 shows the fitted line scans, where the frequency axes are adjusted to give frequencies relative to the uperturbed clock frequency ν_0.

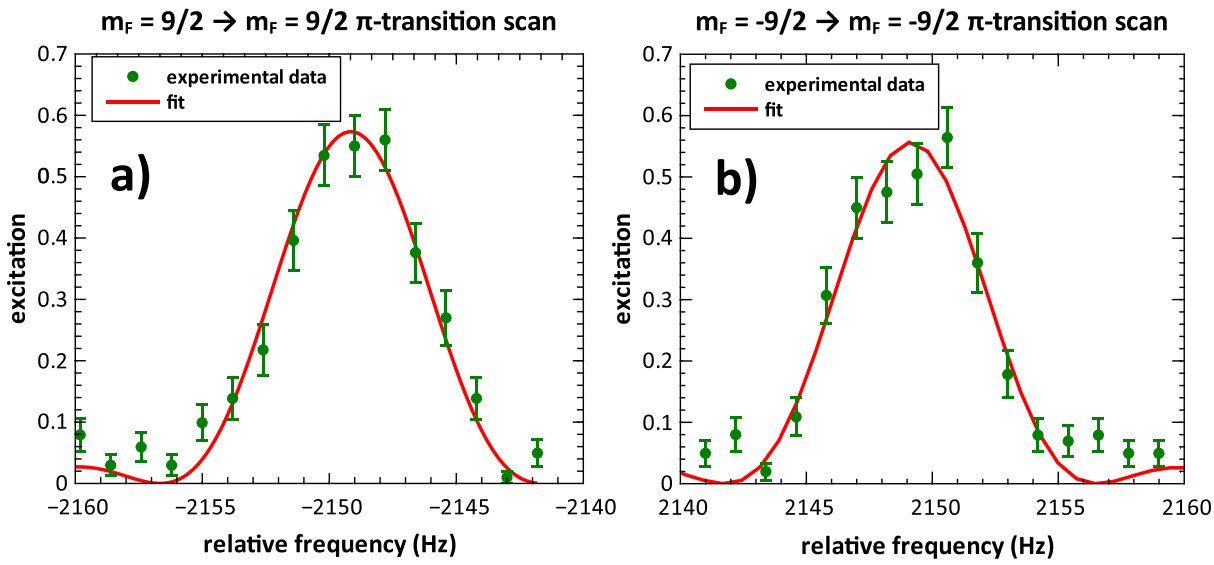

Figure 4.7 Line scans of the π_+ (a) and π_- (b) clock transitions. Experimental data (green) aquired using a probe field intensity I_{low} and a pulse time $\tau_{\text{pulse}} \approx 150\,\text{ms}$ is fitted (solid red line) to find the transition's center frequencies $\nu_{\pi\pm}$ from which the frequency difference is calculated to be $\Delta_{\nu,\pi} = \nu_{\pi-} - \nu_{\pi+} \approx (4298.30 \pm 0.18)\,\text{Hz}$. All frequencies are given relative to the unperturbed clock transition frequency ν_0 for $B = 0\,\text{G}$.

With the frequency difference $\Delta_{\nu,\pi}$, B can now be calculated using Eqs. 4.40 and g-factor values given in [38]. It yields $B \approx (1.065 \pm 0.017) \times 10^{-4}\,\text{T} = (1.065 \pm 0.017)\,\text{G}$. As can be seen from Eqs. 4.3 and 4.4, the 1st order Zeeman shift of both clock frequencies is equal in magnitude but opposite in sign. Hence, its absolute value is given by $\Delta_{\nu,\pi}/2$
Next, line scans of both $\sigma^{\pm}$-transitions are acquired. To do the scans, it is nescessary to determine their relative center frequencies $\nu_{\sigma+}$ and $\nu_{\sigma-}$. These relative frequencies are equal to the respective 1st order Zeeman shifts for the calculated magnetic field B. The shifts (or relative

frequencies) can be calculated by

$$\begin{aligned}\nu_{\sigma\pm} &= \mp\left(\frac{(F-1)\Delta_{\mathrm{e}}}{2\pi} - \frac{F\Delta_{\mathrm{g}}}{2\pi}\right) \\ &= \mp\left(\frac{7}{2}\frac{\Delta_{\mathrm{e}}}{2\pi} - \frac{9}{2}\frac{\Delta_{\mathrm{g}}}{2\pi}\right) \\ &\approx \pm(679 \pm 15)\,\mathrm{Hz}\end{aligned} \tag{4.42}$$

where again $g-$factor values given in [38] were, from which the given uncertainty mainly originates.
Frequency scans are performed around these frequencies. Since both Rabi frequencies $|\Omega_{\pm}|$ are assumed to be small (because of a small ellipticity of the probe field), the scans are acquired using a probe beam intensity I_{high} and a probe time of $\tau_{\mathrm{probe}} = 150\,\mathrm{ms}$. This intensity leads to a π-pulse time of $\tau_{\pi} \approx 10\,\mathrm{ms}$ when probing the $\pi_{\pm}$-transitions as will be shown later in the analysis of $|\Omega_0|$. The resulting scans of the σ^- and σ^+ transitions are shown in Fig. 4.8, the calculated center frequencies $\nu_{\sigma+/-}$ of both transitions are highlighted as red vertical lines.

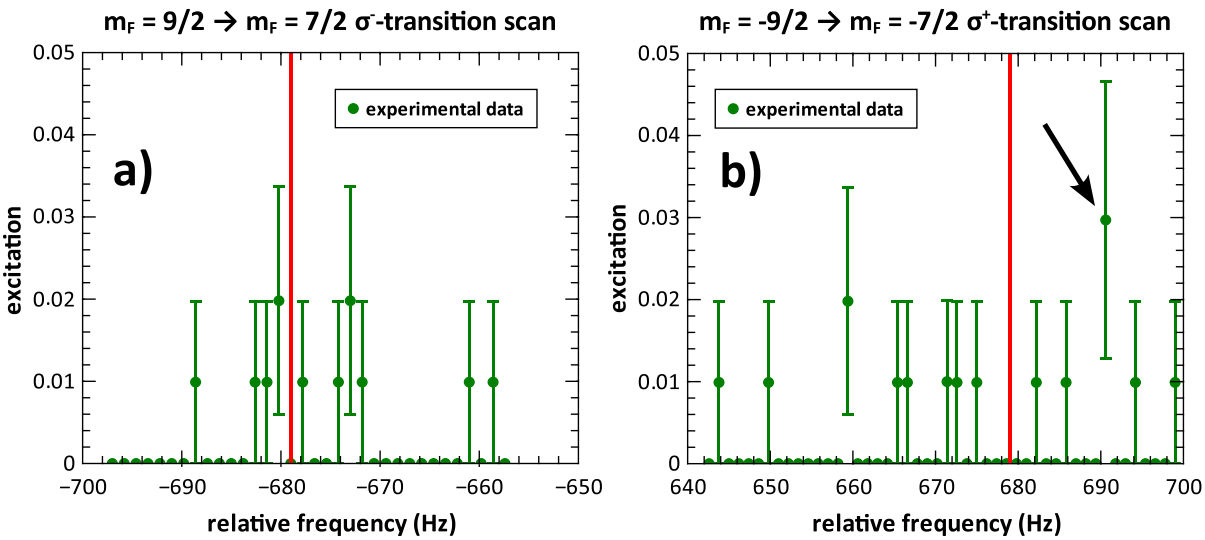

Figure 4.8 Frequency scan around the σ^- (a) and σ^+ (b) transitions. A broad frequency scan is performed around the calculated center frequencies $\nu_{\sigma+/-} = \pm(679 \pm 15)$ highlighted as red vertical lines. The data points (green) are acquired using a probe field intensity I_{high} and pulse time $\tau = 150\,\mathrm{ms}$. Both scans do not show a line shape and the measured excitation is most likely given due to detection noise. For further analysis of the transition's Rabi frequencies $|\Omega_{\pm}|$, the data point highlighted by the black arrow in b) is used as an upper bound for the maximum measured excitation of ≈ 0.03.

Both lines are scanned in a frequency interval of at least $\nu_{\sigma+/-} \pm 18.5\,\mathrm{Hz}$ and resolution of $1.2\,\mathrm{Hz}$. As can be seen, there is no significant excitation and the transitions can not be clearly located. The measured signal is most likely given by detection noise, such that it is not possible to clearly distinguish between noise and an actual transition signal. For further analysis of the $\sigma-$transition's Rabi frequencies $|\Omega_{\pm}|$, the maximum measured signal of ≈ 0.03 acquired in the σ^+ transition scan (see Fig. 4.8 b)), highlighted by the black arrow, will be used as an upper bound for the excitation.
To verify that both $\sigma-$transitions are not shifted out of the scanned frequency interval during the time $t_{\mathrm{measure}} \approx 85\,\mathrm{min}$ between the determination of their respective center frequency (by determination of B via the $\pi-$transition scans) and the actual frequency scan, it is important to analyze possible frequency drifts. There are two significant drifts which need to be taken into account. One is a magnetic field drift which directly affects the transitions via the 1st

order Zeeman shift. The other one is a frequency drift of the cryogenic silicon cavity at PTB (see [47]) to which the clock laser is transfer locked. Its value is $\dot{\nu}_{\text{Silicon}} \approx 120\,\mu\text{Hz/s}$ (private communication with authors of [47]). To find an estimate for a possible magnetic field drift rate $\dot{B}$, clock servo B-field data shown in Fig. 4.9 and aquired over a month in the spring clock campaign is analyzed.

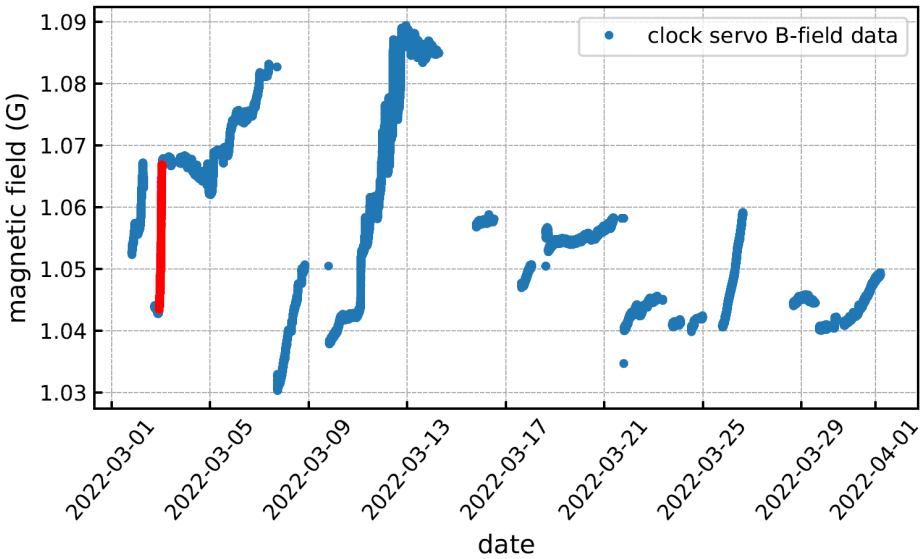

Figure 4.9 Magnetic field fluctuations during the spring clock campaign. To estimate a magnetic field drift during the total measurement time t_{measure}, clock servo magnetic field data (blue) is analyzed. The data points were acquired during the spring clock campaign over a month. The data points highlighted in red show the largest continuous magnetic field drift on a timescale comparable to t_{measure} and are used for the drift evaluation. Using these datapoints, the drift rate can be estimated to be $\dot{B} < 4\,\mu\text{G/s}$

For the estimation of the drift rate, the data highlighted red is taken into account since it shows the steepest continuous drift on a timescale comparable to t_{measure}. From the highlighted data, two data points separated in time by t_{measure} are chosen to estimate the drift rate. This is done by simply dividing the difference between their respective magnetic field values ($\Delta B \approx 18\,\mu\text{G}$) by their time difference ($\Delta t = t_{\text{measure}}$) such that $\Delta B/\Delta t = \dot{B} \approx 4\,\mu\text{G/s}$. Using this rate, the maximum shift of the magnetic field is given by $\dot{B} \times t_{\text{measure}} \approx 20.4\,\text{mG}$ resulting in an upper bound for the 1st order Zeeman shift of $|\Delta\nu_B| \leq 13\,\text{Hz}$ (calculation by analogy with Eq. 4.42).
To evaluate the frequency shift originating from the silicon cavity drift $|\Delta\nu_{\text{Silicon}}|$ one needs to take into account that the probe beam frequency drifts with $4\dot{\nu}_{\text{Silicon}}$. Here the factor of 4 originates from the generation of the probe field by two frequency doubling processes. The shift is then calculated to be $|\Delta\nu_{\text{Silicon}}| = 4\dot{\nu}_{\text{Silicon}} t_{\text{measure}} \approx 2.5\,\text{Hz}$. An upper bound for the total frequency shift due to both drift contributions can then be estimated to be $|\Delta\nu_{\text{drift}}| \leq |\Delta\nu_{\text{B}}| + |\Delta\nu_{\text{Silicon}}| = 15.5\,\text{Hz}$. Because the uncertainty of $\nu_{\sigma+/-}$ is $\sigma(\nu_{\sigma+/-}) = \pm 15\,\text{Hz}$, the total uncertainty of the transition's frequencies is given by the sum of $\sigma(\nu_{0,\sigma+/-})$ and the above calculated shift $|\Delta\nu_{\text{drift}}|$ and yields $(\pm 15\,\text{Hz}) + (\pm 15.5\,\text{Hz}) = \pm 30.5\,\text{Hz}$. This is a crucial result, since it shows the possibility that both σ-transitions were not actually in the scanned intervals which are minimum $\nu_{0,\sigma+/-} \pm 18.5\,\text{Hz}$. Therefore, about 1/3 of the frequency intervals in which the transitions could be located are not covered by the performed scans.[4]

[4]The used scans were originally not acquired to exactly fit the purpose of this analysis. Unfortunately, due to indium loading problems, the scans could not be repeated throughout the process of writing this thesis.

Here it needs to be mentioned that the estimation of possible line shifts is very pessimistic and assumes the worst case scenario of possible drifts. Moreover, the by far largest contribution to the uncertainty of the calculated σ-transition frequencies originates from the uncertainty of the excited state g-factor g_e reported in [38], which is currently the most accurate literature value. Nevertheless, to be completely certain about the validity of the acquired data, the frequency scans of the σ-transitions should be repeated with a scanning range of at least $\pm 30.5\,\mathrm{Hz}$.
In the following, the Rabi frequencies $|\Omega_0|$ and $|\Omega_\pm|$ are evaluated using the above data. For the analysis of $|\Omega_0|$, experimentally acquired data of Rabi oscillations on one of the clock transition is compared to the theoretical model of thermally dephasing Rabi oscillations presented in 2.6. The assumed temperature of the modes along the radial axes with ν_{rad1} and ν_{rad2} are $T_{\mathrm{rad1}} = 0.42\,\mathrm{mK}$ and $t_{\mathrm{rad2}} = 0.73\,\mathrm{mK}$ as found in the clock sequence temperature analysis presented in 5.2.2. The projection of the clock laser onto the radial trap axis with ν_{rad1} (see Fig. 3.2 b)) is assumed to be $\theta = 30°$ [49].
The data was acquired using the probe field intensity I_{high} which was also used in the frequency scan of the σ-transitions. This experiment was done on a different day, but under comparable experimental conditions as for the transition scans shown above. In Fig. 4.10 the data is shown together with plots of the theoretical model for different Rabi frequencies $|\Omega_0|/(2\pi)$.

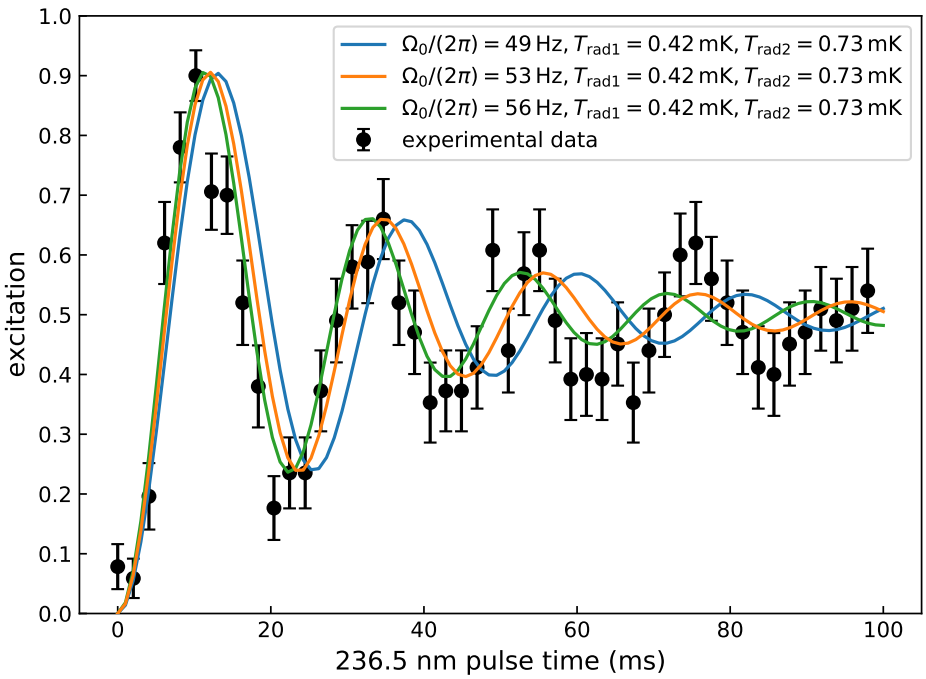

Figure 4.10 Rabi oscillations on the clock transition. To evaluate the Rabi frequency $|\Omega_0|$, experimental data (black) acquired using a probe field intensity I_{high} are plotted together with a theoretical model for thermal dephasing Rabi oscillations (solid lines), which is described in detail in 2.6. The model assumes that all modes referring to the secular frequencies $\nu_{\mathrm{rad1/2}}$ are at temperatures $T_{\mathrm{rad1}} = 0.42\,\mathrm{mK}$ and $T_{\mathrm{rad1}} = 0.73\,\mathrm{mK}$ as found in the clock cycle temperature analysis in section 5.2.2. The solid orange line fits the data points best, the two other solid lines (blue and green) are plotted to estimate the uncertainty of $|\Omega_0|/(2\pi)$.

The resulting Rabi oscillations which agree best with the experimental data are shown as solid orange line. It refers to a Rabi frequency $|\Omega_0|/(2\pi) = 53\,\mathrm{Hz}$ yielding a π-pulse time of $\tau_\pi = \pi/|\Omega_0| \approx 9.4\,\mathrm{ms}$. The two other theoretical Rabi oscillations shown as solid green ($|\Omega_0|/(2\pi) = 56\,\mathrm{Hz}$) and blue ($|\Omega_0|/(2\pi) = 49\,\mathrm{Hz}$) lines are plotted to estimate the uncertainty of $|\Omega_0|/(2\pi)$. For both frequencies there is a significant deviation from the experimental data,

especially for long probe times (i.e. $\tau_{\text{probe}} > 30\,\text{ms}$). The largest Rabi frequency difference (here between the frequencies of oscillations shown by the blue and orange lines) is given by 4 Hz, such that $|\Omega_0|/(2\pi) = (53 \pm 4)\,\text{Hz}$.
For the evaluation of the σ-transitions Rabi frequencies, the upper bound of ≈ 0.03 for the excitation is used, which was found in the σ^+-transition, see Fig. 4.8 b). The evaluation of the corresponding Rabi frequency $\Omega_+/(2\pi)$ is done by analogy with the previous determination of $|\Omega_0|/(2\pi)$. Since the experimental conditions are the same as for probing of the π-transitions, only the Rabi frequency is adjusted such that the theoretical model agrees with the $\approx 3\%$ excitation for the used 150 ms pulse time. The result is shown in Fig. 4.11.

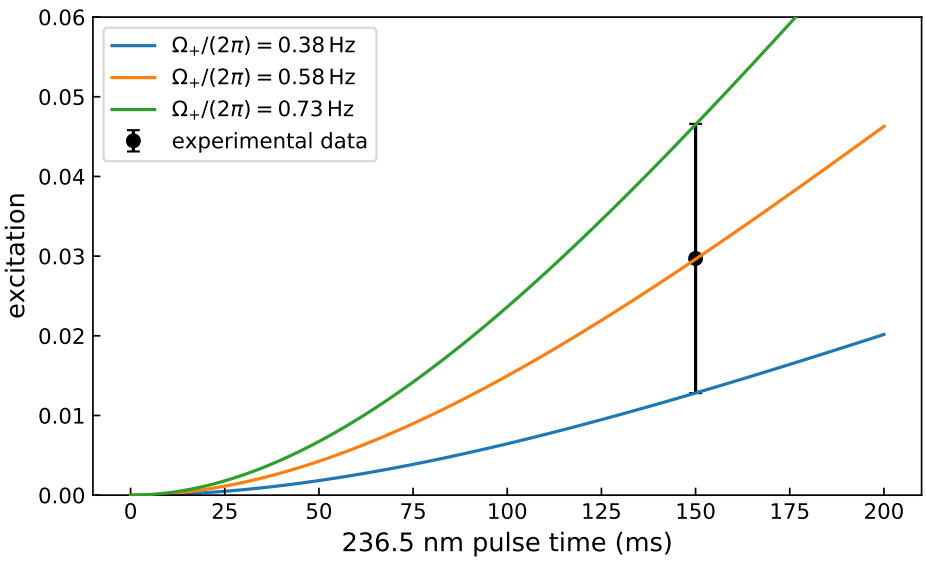

Figure 4.11 Theoretical Rabi oscillations on σ^+-transition. To find an estimate for $|\Omega_+|/(2\pi)$, the data point (black) showing the maximum measured excitation in line scan of the σ^+−transition (see Fig. 4.8 b)) is plotted together with the theoretical model for thermally dephasing Rabi oscillations (solid lines). Except for an adjusted Rabi frequency, the parameters assumed in the model are the same as for the evaluation of the clock transition Rabi frequency $|\Omega_0|$. The Rabi frequency $|\Omega_+|$ is adjusted such that the model fits the the data point (solid orange line) and the borders of the point's uncertainty interval (blue and green lines).

The solid orange line fits the data point best, referring to oscillations with a Rabi frequency of $|\Omega_+|/(2\pi) = 0.58\,\text{Hz}$. In addition, Rabi oscillations for frequencies of 0.38 Hz and 0.73 Hz (blue and green lines) are plotted which match the borders of the data point's uncertainty interval. These frequencies are acquired to estimate an uncertainty for $|\Omega_+|/(2\pi)$. This uncertainty is again calculated by the maximum frequency difference between $|\Omega_+|/(2\pi) = 0.58\,\text{Hz}$ and the frequencies of the two other plotted oscillations such that $|\Omega_+|/(2\pi) = (0.58 \pm 0.20)\,\text{Hz}$.
Since an upper bound of $|\Omega_+|$ is now found, an upper bound for $|\epsilon\xi|$ can be evaluated, describing the worst case of polarization impurities during clock operation. For this, it is conservatively assumed that the ellipticity of the probe field is purely right handed. This assumption leads to a vanishing coupling between the two states $|F = 9/2, m_{F,g} = 9/2\rangle$ and $|F = 9/2, m_{F,e} = 9/2\rangle$ and therefore vanishing $|\Omega_-|$. As a result, $|\epsilon\xi|$ maximizes and hence the shift, as can be seen in Eqs. 4.38 and 4.25. Moreover, it allows to rewrite Eq. 4.38 as

$$\frac{|\Omega_+|^2}{|\Omega_0|^2}\frac{F}{2} \geq |\epsilon\xi|. \tag{4.43}$$

Using the above values for $|\Omega_+|/(2\pi)$ and $|\Omega_0|/(2\pi)$ as well as $F = 9/2$, the upper bound for

$|\epsilon\xi|$ yields

$$|\epsilon\xi|_{\max} \leq (2.7 \pm 1.9) \times 10^{-4}. \tag{4.44}$$

In the next subsection the shift will be evaluated for the indium setup based on the aforementioned results.

4.1.5 Evaluation of the ellipticity induced shift for the $^{115}\mathrm{In}^+$ clock

After an upper bound for $|\epsilon\xi|$ was found in the previous subsection, there are only experimental parameters left to calculate an upper bound for the ellipticity induced shift given in Eq. 4.25. For the bias magnetic field, a value of $B = (1.07 \pm 0.06)\,\mathrm{G}$ is assumed, which is derived from the mean value of the data shown in Fig. 4.9. The uncertainty is given by the maximum measured magnetic field difference. Now, Δ_Z can be calculated with $g-$factor values given in [38]. Lastly, the Rabi frequency during clock spectroscopy needs to be determined, since the yet determined frequency $|\Omega_0| \equiv |\Omega_{0,\mathrm{high}}|$ refers to the probe field intensity I_{high}, while I_{low} was used during the spring clock campaign. This conversion is done using $\Omega_{0,\mathrm{high}}/(2\pi) = (53 \pm 4)\,\mathrm{Hz}$ and the ratio $I_{\mathrm{high}}/I_{\mathrm{low}} = 134 \pm 2.3$, where the ratio is determined from respective intensity stabilization setpoints. Since the ratio of the Rabi frequencies at I_{high} and I_{low} is given by

$$\frac{\Omega_{0,\mathrm{high}}}{\Omega_{0,\mathrm{low}}} = \frac{\frac{d_{\mathrm{eg,F}} E_{\mathrm{high}} a^{(0)} \sqrt{F}}{\hbar\sqrt{F+1}}}{\frac{d_{\mathrm{eg,F}} E_{\mathrm{low}} a^{(0)} \sqrt{F}}{\hbar\sqrt{F+1}}} = \frac{E_{\mathrm{high}}}{E_{\mathrm{low}}} = \sqrt{\frac{I_{\mathrm{high}}}{I_{\mathrm{low}}}}, \tag{4.45}$$

where the definition of $|\Omega_0|$ in Eq. 4.12 was used, $\Omega_{0,\mathrm{low}}/(2\pi)$ can be calculated via

$$\frac{\Omega_{0,\mathrm{low}}}{2\pi} = \frac{\Omega_{0,\mathrm{high}}}{2\pi\sqrt{\frac{I_{\mathrm{high}}}{I_{\mathrm{low}}}}} \approx (4.6 \pm 0.3)\,\mathrm{Hz}. \tag{4.46}$$

Using these values, the A parameter from Eq. 4.26, the definition of Δ_Z and Eq. 4.25, the upper bound for the shift yields

$$\frac{|\delta_{\mathrm{ac,max}}^{(\mathrm{el-ind})}|}{2\pi} \leq \frac{|g_{\mathrm{g}}^2 - g_{\mathrm{e}}^2|}{4F|g_{\mathrm{g}} g_{\mathrm{e}}|} \frac{|\Omega_{0,\mathrm{low}}|^2}{2\pi|\frac{g_e \mu_B |\mathrm{B}|}{\hbar} - \frac{g_g \mu_B |\mathrm{B}|}{\hbar}|} |\epsilon\xi|_{\max} \approx (0.5 \pm 0.4)\,\mu\mathrm{Hz}, \tag{4.47}$$

resulting in a fractional frequency shift (using $\nu_{\mathrm{clock}} = 1267\,\mathrm{THz}$) of

$$\frac{|\delta_{\mathrm{ac,max}}^{(\mathrm{el-ind})}|}{2\pi \times \nu_{\mathrm{clock}}} \leq (4 \pm 3) \times 10^{-22}. \tag{4.48}$$

Although Yudin et all. propose in [18] to include the absolute shift in the evaluation of atomic clock uncertainty budgets (and hence the evaluated value in Eq. 4.48), this is done differently for the indium budget because of the following reasoning.
Since polarization impurities are introduced by, e.g., temperature fluctuations in birefringent materials, it is likely that the angle ϵ and hence the orientation of the ellipticity varies over time. Therefore it is assumed that the upper bound for $|\Omega_+|$ is also an upper bound for $|\Omega_-|$. Moreover, in the transition scan of the $\sigma-$ transitions (see Fig. 4.8) it is not possible to distinguish detection noise from an actual signal produced by the driven transitions. The only statement which can be made is that $\{|\Omega_+|/(2\pi), |\Omega_-|/(2\pi)\} \in [0, 0.58]\,\mathrm{Hz}$. Therefore the $\sigma-$transition Rabi frequencies used for the shift evaluation are $|\Omega_{+,\mathrm{mean}}| = |\Omega_{-,\mathrm{mean}}| = |\Omega_+|/2 = 0.58/2\,\mathrm{Hz}$. The uncertainty is chosen to be $u(|\Omega_{+/-,\mathrm{mean}}|) = \pm 0.29\,\mathrm{Hz}$ such that the uncertainty interval overlaps the full range of possible $\sigma-$Rabi frequencies $[0, 0.58]\,\mathrm{Hz}$. Note that $|\Omega_\pm| = 0\,\mathrm{Hz}$ is also included in the uncertainty interval to account for the case of a vanishing shift, i.e. for a linearly polarized probe

field. In addition, there is the uncertainty of the determination of $|\Omega_+|/(2\pi)$ of $\pm 0.20\,\mathrm{Hz}$ which needs to be added in quadrature such that

$$\frac{\Omega_{+\mathrm{mean}}}{2\pi} = \frac{\Omega_{-\mathrm{mean}}}{2\pi} = (0.3 \pm 0.4)\,\mathrm{Hz}$$

These assumptions lead to a vanishing factor $|\epsilon\xi|$ and therefore to a vanishing shift. Now, $|\epsilon\xi|$ yields

$$|\epsilon\xi| = (0 \pm 2.3) \times 10^{-4}. \tag{4.49}$$

Using this, the shift is reevaluated to be

$$\frac{\delta_{\mathrm{ac}}^{(\mathrm{el-ind})}}{2\pi} = (0 \pm 0.5)\,\mu\mathrm{Hz} \tag{4.50}$$

while the fractional shift yields

$$\frac{\delta_{\mathrm{ac}}^{(\mathrm{el-ind})}}{2\pi \times \nu_{\mathrm{clock}}} = (0 \pm 4) \times 10^{-22}. \tag{4.51}$$

4.2 Ac-Stark shift by far off-resonant transitions

This section presents the results of the analysis of the ac-Stark shift by far off-resonant transitions. 4.2.1 gives a brief overview over the origin othe the shift. Afterwards, the shift is determined in 4.2.2 for the $^{115}\mathrm{In}^+$ clock at PTB based on theoretical considerations.

4.2.1 Theoretical background

In general, every off-resonant transition including either the $^1\mathrm{S}_0$ ground state or the $^3\mathrm{P}_0$ excited state of the clock transition results in an ac-Stark shift of the respective clock states. For large detunings $\Delta = \omega_{\mathrm{probe}} - \omega_0$, where ω_{probe} is the probe field frequency and ω_0 the frequency of the off-resonant transition, the ac-Stark shift of the ground state of this transition is given by [22]

$$\Delta E_{g,\,\mathrm{off-res}} = \frac{\hbar|\Omega|^2}{4\Delta} = \frac{(d_{eg}E_{\mathrm{probe}})^2}{4\Delta\hbar}. \tag{4.52}$$

Here d_{eg} is the dipole matrix element of the respective off-resonant transition and E_{probe} the electric field strength of the probe field as presented in 2.3.2. In principle, also the energy shift of the excited state needs to be taken into account, if one of the clock states is the excited state of an off-resonant transition. But for the $^3\mathrm{P}_0$ excited state, there is no such transition as will be presented in the next section. Since the clock transition frequency is calculated via the energy difference between the two clock states $\omega_{\mathrm{clock}} = \Delta E_{\mathrm{clock}}/\hbar = (E_{\mathrm{e}} - E_{\mathrm{g}})/\hbar$, in presence of coupling Ω, each energy shift of one of the levels directly results in a frequency shift

$$\delta_{\mathrm{ac}}^{(\mathrm{off-res})} = \pm\frac{\Delta E_{g,\,\mathrm{off-res}}}{\hbar} = \pm\frac{|\Omega|^2}{4\Delta}. \tag{4.53}$$

Here the sign of the respective frequency shift depends on the sign of Δ and whether the ground or excited state of the clock transition is shifted. For example, when the off-resonant transition is blue detuned relative to the clock transition ($\omega_{\mathrm{clock}} < \omega_0$) and includes the clock transition ground state (e.g., the $^1\mathrm{S}_0 \rightarrow {}^3\mathrm{P}_1$ indium detection transition), the ground state is shifted to smaller energies, leading to a larger energy difference $\Delta E_{\mathrm{clock}}$. Hence the related frequency shift has a positive sign. On the other hand, if the off-resonant transition is blue detuned including the excited state of the clock transition (e.g. $^3\mathrm{P}_0 \rightarrow {}^3\mathrm{D}_1$), its energy is also shifted to a smaller value which results in a reduced energy difference $\Delta E_{\mathrm{clock}}$ and to a negative frequency shift. The total ac-Stark shift by far off-resonant transitions is then given by the sum of the ac-Stark shifts originating from all parasitic transitions

$$\delta_{\mathrm{ac,total}}^{(\mathrm{off-res})} = \sum_{i=1}^{N_{\mathrm{off-res}}} \delta_{\mathrm{ac},i}^{(\mathrm{off-res})}. \tag{4.54}$$

4.2.2 Evaluation of the ac-Stark shift by far off-resonant transitions

For the evaluation the ac-Stark shift by far off-resonant transitions $\delta_{\mathrm{ac}}^{\mathrm{off-res}}$, the probe field strength during clock interrogation E_{probe} and the dipole matrix elements d_{eg} as well as the respective detunings Δ of the investigated transitions need to be determined. For the determination of E_{probe}, the previously determined Rabi frequency $|\Omega_{0,\mathrm{low}}|$ (Eq. 4.46) can be used. The Rabi frequency of the clock transition is given as defined in Eq. 4.12 by

$$|\Omega_0| = \frac{|d_{eg,F} E_{\mathrm{probe}} a^{(0)} c_{\mathrm{CG},0}|}{\hbar}, \tag{4.55}$$

where $d_{eg,F} = \langle F_g || d || F_e \rangle$ is the reduced dipole matrix element and $c_{\mathrm{CG},0}$ the respective Clebsch-Gordan coefficient. From Eq. 4.12 one finds

$$\begin{aligned} E_{\mathrm{probe}} &= \frac{\hbar |\Omega_0|}{|d_{eg,F} a^{(0)} c_{\mathrm{CG}}|} \\ &\approx \frac{\hbar |\Omega_0|}{|d_{eg,F} c_{\mathrm{CG}}|}, \end{aligned} \tag{4.56}$$

where in the last step $|a^{(0)}| \approx 1$ is assumed, which is justified as follows. In the last section, $|\Omega_0| = 2\pi(53 \pm 4)\,\mathrm{Hz}$ as well as an upper bound for the $\sigma-$transition Rabi frequencies $|\Omega_+| \leq 2\pi(0.58 \pm 0.20)\,\mathrm{Hz}$ were found using the probe field intensity I_{high}. The ratio of $|\Omega_0|$ and $|\Omega_+|$ (Eqs. 4.12 and 4.11) normalized by their respective Clebsch-Gordan coefficients $c_{\mathrm{CG},0}$ and $c_{\mathrm{CG},+}$ yields

$$\frac{|\Omega_0|}{|\Omega_+|} \frac{c_{\mathrm{CG},+}}{c_{\mathrm{CG},0}} = \frac{53}{0.58} \frac{\frac{1}{\sqrt{F+1}}}{\frac{\sqrt{F}}{\sqrt{F+1}}} = \frac{53}{0.58} \sqrt{\frac{2}{9}} = \frac{|a^{(0)}|}{|a^{(+1)}|} \tag{4.57}$$

such that

$$|a^{(+1)}| = \frac{0.58}{53} \sqrt{\frac{9}{2}} |a^{(0)}| \approx 0.023 |a^{(0)}|. \tag{4.58}$$

Assuming $|a^{(-1)}| \approx |a^{(+1)}|$ and using that the polarization vector $\mathbf{a}$ (Eq. 4.10) is a unit vector, it follows that

$$1 = |\mathbf{a}| = \sqrt{|a^{(0)}|^2 + |a^{(+1)}|^2 + |a^{(-1)}|^2} \approx \sqrt{|a^{(0)}|^2 + 2(0.023|a^{(0)}|)^2} \approx |a^{(0)}|. \tag{4.59}$$

Hence for the determination of E_{probe} only the matrix element of the clock transition, in the following denoted as $d_{eg,F,\mathrm{clock}}$, needs to be found.
In general, dipole matrix elements can calculated from excited state life times τ_{life} or Einstein A-coefficients $A = \tau_{\mathrm{life}}^{-1}$ (decay rates), while the connection between A and $d_{\mathrm{eg}} = |\langle g|d|e\rangle|$ is given by [25]

$$A = \frac{\omega_0^2 |\langle g|d|e\rangle|^2}{3\pi\epsilon_0 \hbar c^3}, \tag{4.60}$$

where ω_0 is the transition frequency, ϵ_0 the vacuum permittivity and c the speed of light. For fine structure transitions $|J_g\rangle \to |J_e\rangle$, the degeneracy of the ground and excited state $2J_{g/e} + 1$ needs to be taken into account. It can be shown that in this case the decay rate is given by [25]

$$A_{J_g J_e} = \frac{\omega_0^2}{3\pi\epsilon_0 \hbar c^3} \frac{1}{2J_e + 1} \sum_{m_g, m_e} |\langle J_g, m_g | d | J_e, m_e \rangle|^2 \tag{4.61}$$

$$= \frac{\omega_0^2}{3\pi\epsilon_0 \hbar c^3} \frac{2J_g + 1}{2J_e + 1} |\langle J_g || d || J_e \rangle|^2. \tag{4.62}$$

Equation 4.62 can then be solved for the reduced matrix element $d_{eg,J} = |\langle J_g||d||J_e\rangle|$

$$|\langle J_g||d||J_e\rangle| = \sqrt{\frac{A_{J_gJ_e}3\pi\epsilon_0\hbar\lambda^3}{(2\pi)^3}\frac{2J_e+1}{2J_g+1}}, \tag{4.63}$$

where $\omega_0/c = k$ is replaced by $k = (2\pi)/\lambda$.
To calculate the dipole matrix element of the clock transition, the Einstein A-coefficient is calculated from the $^3P_0$ state lifetime of $\tau_{\text{life}} = 0.195(8)\,\text{s}$ reported in [38]. The coefficient yields $A_{\text{clock}} = (5.13 \pm 0.21)\,\text{s}^{-1}$. Now, using Eq. 4.63, the clock transition wavelength $\lambda_{\text{clock}} = c/\nu_{\text{clock}}$ as well as $J_e = J_g = 0$, the reduced matrix element of the clock transition is calculated to be $d_{eg,J,\text{clock}} = (1.55 \pm 0.03) \times 10^{-33}\,\text{Cm}$. Since the total angular momentum of the clock transition ground and excited state includes the nuclear spin $I = 9/2$, one needs to find the reduced matrix element $d_{eg,F,\text{clock}} = \langle F_g = 9/2||d||F_e = 9/2\rangle$ in the hyperfine basis $\{|F\rangle\}$. But regarding the fact that both clock states are $J = 0$ states, there is just one $F = 9/2$ hyperfine state for each clock state. Therefore

$$d_{eg,F,\text{clock}} = d_{eg,J,\text{clock}}.$$

A straight forward proof is given as follows. At first, following [25], the reduced dipole matrix element in the basis $\{|J\rangle\}$ can be expressed in terms of $\{|F, m_F\rangle\}$ by

$$\sum_{F_g,m_g} |\langle F_g, m_g|d|F_e, m_e\rangle|^2 = \frac{2J_g+1}{2J_e+1}|\langle J_g||d||J_e\rangle|^2. \tag{4.64}$$

Applying Eq. 4.64 to the clock transition yields

$$\begin{aligned}\sum_{F_g,m_g} |\langle F_g, m_g|d|F_e, m_e\rangle|^2 &= |\langle\frac{9}{2},\frac{7}{2}|d|\frac{9}{2},\frac{9}{2}\rangle|^2 + |\langle\frac{9}{2},\frac{9}{2}|d|\frac{9}{2},\frac{9}{2}\rangle|^2 \\ &= \frac{2J_g+1}{2J_e+1}d^2_{eg,J,\text{clock}} \overset{J_g=J_e}{=} d^2_{eg,J,\text{clock}}.\end{aligned} \tag{4.65}$$

Now, the two matrix elements on the right hand side of Eq. 4.65 can be replaced using the Wigner-Eckart theorem. The application of the theorem to transitions between hyperfine states yields [25]

$$\langle F_g, m_g|d|F_e, m_e\rangle = \langle F_g||d||F_e\rangle \underbrace{\langle F_g, m_g|F_e, m_e; 1, q\rangle}_{c_{\text{CG}}}, \tag{4.66}$$

where $q = \{-1, 1, 0\}$ indicates the photon polarization with respect to the bias magnetic field orientation. Using Eq. 4.66, Eq. 4.65 can be rewritten as

$$\begin{aligned}|\langle\frac{9}{2},\frac{7}{2}|d|\frac{9}{2},\frac{9}{2}\rangle|^2 + |\langle\frac{9}{2},\frac{9}{2}|d|\frac{9}{2},\frac{9}{2}\rangle|^2 &= d^2_{eg,F,\text{clock}}(\underbrace{|\langle\frac{9}{2},\frac{7}{2}|\frac{9}{2},\frac{9}{2};1,-1\rangle|^2}_{|c_{\text{CG},-}|^2} + \underbrace{|\langle\frac{9}{2},\frac{9}{2}|\frac{9}{2},\frac{9}{2};1,0\rangle|^2}_{|c_{\text{CG},0}|^2}) \\ &= d^2_{eg,F,\text{clock}}\left(\frac{\frac{9}{2}}{\frac{9}{2}+1} + \frac{1}{\frac{9}{2}+1}\right) = d^2_{eg,F,\text{clock}},\end{aligned}$$

where the Clebsch-Gordan coefficients as defined in Eqs. 4.11 and 4.12 are used. Finally, again using Eq. 4.64,

$$\begin{aligned}d^2_{eg,F,\text{clock}} &= d^2_{eg,J,\text{clock}} \\ \Leftrightarrow d_{eg,F,\text{clock}} &= d_{eg,J,\text{clock}}.\end{aligned}$$

An alternative approach to determine the clock transition matrix element is presented in [57]. This approach uses the fact that the clock transition excited state $|\widetilde{^3\mathrm{P}_0}, F = 9/2\rangle$ is a mixture of the unperturbed states $|^3\mathrm{P}_0, F = 9/2\rangle$, $|^3\mathrm{P}_1, F = 9/2\rangle$ and $|^1\mathrm{P}_0, F = 9/2\rangle$

$$|\widetilde{^3\mathrm{P}_0}, F = \frac{9}{2}\rangle = |^3\mathrm{P}_0, \frac{9}{2}\rangle + \alpha_0(\alpha|^3\mathrm{P}_1, \frac{9}{2}\rangle + \beta|^1\mathrm{P}_1, \frac{9}{2}\rangle) + \beta_0(\beta|^3\mathrm{P}_1, \frac{9}{2}\rangle + \alpha|^1\mathrm{P}_1, \frac{9}{2}\rangle), \tag{4.67}$$

with mixing coefficients $\alpha_0 = -1.1 \times 10^{-3}$, $\beta_0 = 3.5 \times 10^{-5}$, $\alpha = 0.997$ and $\beta = -0.079$. Note that the Hamiltonian which introduces the mixing between $^3\mathrm{P}_0$ and $^3\mathrm{P}_1$,$^1\mathrm{P}_1$ is diagonal in the $\{|F\rangle\}$ basis, such that only $F = I = 9/2$ states contribute to the state mixture [58]. Using Eq. 4.67, $d_{eg,F,\mathrm{clock}}$ is given by

$$\underbrace{|\langle^1\mathrm{S}_0, F = \frac{9}{2}||d||\widetilde{^3\mathrm{P}_0}, F = \frac{9}{2}\rangle|}_{d_{eg,F,\mathrm{clock}}} = |(\alpha_0\beta + \beta_0\alpha)|\underbrace{|\langle^1\mathrm{S}_0, F = \frac{9}{2}||d||^1\mathrm{P}_1, F = \frac{9}{2}\rangle|}_{:=d_{eg,F,158\mathrm{nm}}}. \tag{4.68}$$

Hence, to calculate $d_{\mathrm{eg,F,clock}}$, the matrix element $d_{\mathrm{eg,F,158nm}}$ of the $|^1\mathrm{S}_0, F = 9/2\rangle \rightarrow |^1\mathrm{P}_1, F = 9/2\rangle$ at $\lambda \approx 158.637\,\mathrm{nm}$ (taken from [59]) needs to be determined. At first, the dipole matrix element $d_{\mathrm{eg,J,158nm}}$ is calculated using Eq. 4.63 and the respective Einstein A coefficient $A_{158\,\mathrm{nm}} = (1.27 \pm 0.08) \times 10^9\,\mathrm{s}^{-1}$ reported in [60], such that $d_{\mathrm{eg,J,158nm}} = (2.32 \pm 0.07) \times 10^{-29}\,\mathrm{Cm}$. Now $d_{\mathrm{eg,F,158nm}}$ can be calculated from $d_{\mathrm{eg,J,158nm}}$ using the decomposition formula [25]

$$\underbrace{\langle F_g||d||F_e\rangle}_{d_{eg,F}} = \underbrace{\langle J_g||d||J_e\rangle}_{d_{eg,J}}(-1)^{F_e+J_g+1+I}\sqrt{(2F_e+1)(2J_g+1)}\underbrace{\begin{Bmatrix} J_g & J_e & 1 \\ F_e & F_g & I \end{Bmatrix}}_{\text{Wigner } 6j \text{ symbol}}, \tag{4.69}$$

where the expression in curly brackets is the Wigner $6j$ symbol which can be calculated using, e.g. Mathematica. Finally, the clock transition matrix element yields $d_{eg,F,\mathrm{clock}} = (1.63 \pm 0.05) \times 10^{-33}\,\mathrm{Cm}$. As can be seen, both ways to calculate the clock transition matrix element agree with each other within the given uncertainties. Since the first calculated value of the matrix element is directly calculated from the excited state lifetime and hence fewer experimental parameters are needed for its determination, $d_{eg,J,\mathrm{clock}} = (1.55 \pm 0.03) \times 10^{-33}\,\mathrm{Cm}$ is used in the following. Now, the probe field E_{probe} can be calculated using $c_{\mathrm{CG},0}$, the Rabi frequency $|\Omega_{0,\mathrm{low}}| = 2\pi \times (4.6 \pm 0.3)\,\mathrm{Hz}$ determined in the previous section (see Eq. 4.46) and Eq. 4.56, such that $E_{\mathrm{probe}} = (2.18 \pm 0.18)\,\mathrm{V/m}$.

In the following, the order of magnitude of the ac-Stark shift produced by different off-resonant transitions is investigated. For the first analysis, the hyperfine structure is neglected and the ac-Stark shift is calculated for fine structure states $|J\rangle$ using the respective dipole matrix elements $d_{eg,J}$. This is done to estimate the magnitude of each shift and to decide which transitions need to be considered in the evaluation of total shift $\delta_{\mathrm{ac,total}}^{(\mathrm{off-res})}$. In principle, every-off resonant transition coupling to the clock transition ground or excited state produces an ac-Stark shift and should therefore be included in the shift analysis. But since $\delta_{\mathrm{ac}}^{(\mathrm{off-res})} \propto \Omega^2 \propto d_{eg}^2 \propto A$ and $\delta_{\mathrm{ac}}^{(\mathrm{off-res})} \propto \Delta^{-1}$, the significance of each off resonant transition is therefore given by the magnitude of the respective $A-$coefficient and the detuning Δ relative to the clock transition. In the NIST Atomic Spectra Database [59], wavelength λ as well as $A-$coefficients for various transitions in In^+ can be found. In Tab. 3, selected transitions together with needed parameters for the calculation are gathered. These transitions are chosen because they show either a small detuning or a large $A-$coefficient. With these parameters, for every transition the reduced dipole matrix element $d_{eg,J}$ is calculated using Eq. 4.63 and finally, using Eq. 4.53 and the previously calculated probe field E_{probe}, each contribution $\delta_{\mathrm{ac,i}}^{(\mathrm{off-res})}$.

Table 3 Transitions and respective experimental parameters for the determination of the individual shifts $\delta_{\mathrm{ac},i}^{(\mathrm{off-res})}$, transitions highlighted blue result in a fractional frequency shift $> 10^{-22}$ and are used for further evaluation of the total shift $\delta_{\mathrm{ac,total}}^{(\mathrm{off-res})}$.

transition	λ (nm)	A (10^9/s)	Δ (10^{15} Hz)	$d_{eg,J}$ (10^{-30} Cm)	$\frac{\delta_{\mathrm{ac,i}}^{(\mathrm{off-res})}}{\omega_{\mathrm{clock}}}$ (10^{-22})
$(5s)^2\ {}^1\mathrm{S}_0 \rightarrow 5s8p\ {}^1\mathrm{P}_1$	73.478	0.036	−2.81263	1.233	+0.012
$(5s)^2\ {}^1\mathrm{S}_0 \rightarrow 5s5p\ {}^1\mathrm{P}_1$	158.637	1.27[60]	−0.622399	23.230	+18.474
$(5s)^2\ {}^1\mathrm{S}_0 \rightarrow 5s5p\ {}^3\mathrm{P}_1$	230.606	0.0023	−0.0326177	1.733	+1.961
$5s5p\ {}^3\mathrm{P}_0 \rightarrow 5s10d\ {}^3\mathrm{D}_1$	96.993	0.046	−1.82346	2.114	−0.052
$5s5p\ {}^3\mathrm{P}_0 \rightarrow 5s11s\ {}^3\mathrm{S}_1$	97.348	0.016	−1.81219	1.253	−0.018
$5s5p\ {}^3\mathrm{P}_0 \rightarrow 5s8d\ {}^3\mathrm{D}_1$	102.244	0.034	−1.66473	1.967	−0.050
$5s5p\ {}^3\mathrm{P}_0 \rightarrow 5s6d\ {}^3\mathrm{D}_1$	121.263	0.13	−1.20485	4.967	−0.436
$5s5p\ {}^3\mathrm{P}_0 \rightarrow 5s7s\ {}^1\mathrm{S}_0$	126.316	0.03	−1.10595	1.465	−0.041
$5s5p\ {}^3\mathrm{P}_0 \rightarrow (5p)^2\ {}^3\mathrm{P}_1$	164.005	0.37	−0.560545	13.180	−6.603
$5s5p\ {}^3\mathrm{P}_0 \rightarrow 5s5d\ {}^3\mathrm{D}_1$	167.187	0.73	−0.525754	19.054	−14.715
$5s5p\ {}^3\mathrm{P}_0 \rightarrow 5s6s\ {}^3\mathrm{S}_1$	193.619	0.096	−0.280962	8.612	−5.624

As can be seen, there are just a few transitions producing a fractional frequency shift on the order of $10^{-21} \cdots 10^{-22}$. These blue highlighted transitions (see Tab. 3) will be used in the following analysis of the total shift $\delta_{\mathrm{ac}}^{(\mathrm{off-res})}$ and its uncertainty. All other transitions result in a minor contribution to the total shift and are therefore neglected.
For the evaluation of the total shift and its uncertainty, the original references of the data given in [59] are reviewed to find the uncertainties of the Einstein $A-$parameters. These uncertainties as well as the evaluated uncertainties of matrix elements and the fractional frequency shifts are shown in Tab. 4. For the starred values uncertainties could not be found, because they originate from theoretical calculations or the reference was not accessible. Therefore, a conservative uncertainty of $\pm 100\%$ was assumed. The given wavelengths are precisely known compared to the $A-$parameters and therefore considered without uncertainty.

Table 4 Individual fractional frequency shifts $\delta_{\mathrm{ac},i}^{(\mathrm{off-res})}/\omega_{\mathrm{clock}}$ and calculated uncertainties for the transitions highlighted blue in Tab. 4.

transition	A (10^9/s)	$d_{eg,J}$ (10^{-30} Cm)	$\frac{\delta_{\mathrm{ac,i}}^{(\mathrm{off-res})}}{\omega_{\mathrm{clock}}}$ (10^{-22})
$(5s)^2\ {}^1\mathrm{S}_0 \rightarrow 5s5p\ {}^1\mathrm{P}_1$	1.27 ± 0.08[60]	23.2 ± 0.7	$+18.5 \pm 3.2$
$(5s)^2\ {}^1\mathrm{S}_0 \rightarrow 5s5p\ {}^3\mathrm{P}_1$	0.0023 ± 0.0002[60]	1.73 ± 0.08	$+2.0 \pm 0.4$
$5s5p\ {}^3\mathrm{P}_0 \rightarrow (5p)^2\ {}^3\mathrm{P}_1$	$0.37^* \pm 0.37$ [59, 61]	13 ± 7	-6.6 ± 6.6
$5s5p\ {}^3\mathrm{P}_0 \rightarrow 5s5d\ {}^3\mathrm{D}_1$	$0.73^* \pm 0.73$[59, 62]	20 ± 10	-14.7 ± 14.9
$5s5p\ {}^3\mathrm{P}_0 \rightarrow 5s6s\ {}^3\mathrm{S}_1$	$0.096^* \pm 0.096$[59, 61]	9 ± 4	-5.6 ± 5.7

Now, the total total shift $\delta_{\mathrm{ac,total}}^{(\mathrm{off-res})}$ can be calculated using Eq. 4.54

$$\frac{\delta_{\mathrm{ac,total}}^{(\mathrm{off-res})}}{2\pi} = (-0.8 \pm 2.2)\,\mu\mathrm{Hz}$$

which leads to a fractional frequency shift

$$\frac{\delta_{\mathrm{ac,total}}^{(\mathrm{off-res})}}{\omega_{\mathrm{clock}}} = (-0.7 \pm 1.7) \times 10^{-21}.$$

So far, the treatment of the shift completely neglects the hyperfine structure of the contributing states. Only $|J\rangle$ states were considered. Since ^{115}In has a half integer nuclear spin

$I = 9/2$, for every $J = 1$ state, there are three hyperfine states $|F = \{11/2, 9/2, 7/2\}\rangle$. As shown in Eq. 4.59, the components $|a^{(\pm 1)}|$ driving $\sigma^{\pm}$ transitions are small compared to $|a^{(0)}|$. Therefore, the probe field mainly introduces coupling between $\Delta m_F = 0$ Zeeman substates and $\Delta m_F = \pm 1$ transitions are highly suppressed. As a result, there will be only coupling between the $|m_{F,g/e}|= 9/2$ Zeeman substates of the clock ground and excites state Zeeman manifolds to $|F = \{11/2, 9/2\}, |m_F|= 9/2\rangle$ excited states of the considered off resonant transitions. On the other hand, there is no coupling at all to $|F = 7/2\rangle$ hyperfine states, due to missing $||m_F|= 9/2\rangle$ substates. The missing coupling will lead to a reduced ac-Stark shift compared to the previously determined value. A more rigorous treatment which considers the presence of hyperfine structure is done in the following.
To take the hyperfine structure into account, it is nescessary to calculate the respective matrix elements $d_{eg,F,m_F} = \langle F_g, m_F|d|F_e, m_F\rangle$. This can be done from the matrix elements $d_{eg,J}$ given in Tab. 5 and the decomposition formula in Eq. 4.69 and afterwards applying the Wigner-Eckart theorem for hyperfine transitions (see Eq. 4.66). The matrix elements $d_{eg,F,m}$ as well as resulting ac-stark shifts are calculated and gathered in Tab. 5.

Table 5 Reevaluated individual fractional frequency shifts $\delta_{\mathrm{ac},i}^{(\mathrm{off-res})}/\omega_{\mathrm{clock}}$ for selected hyperfine Zeeman transitions.

transition	$d_{eg,F,\lvert m_F\rvert=9/2}$ (10^{-30} Cm)	$\frac{\delta_{\mathrm{ac,i}}^{(\mathrm{off-res})}}{\omega_{\mathrm{clock}}}$ (10^{-22})
$(5s)^2\ {}^1\mathrm{S}_0 \rightarrow 5s5p\ {}^1\mathrm{P}_1\ F = 11/2$	6.26 ± 0.20	$+1.34 \pm 0.23$
$(5s)^2\ {}^1\mathrm{S}_0 \rightarrow 5s5p\ {}^1\mathrm{P}_1\ F = 9/2$	12.1 ± 0.4	$+5.0 \pm 0.9$
$(5s)^2\ {}^1\mathrm{S}_0 \rightarrow 5s5p\ {}^3\mathrm{P}_1\ F = 11/2$	0.467 ± 0.020	$+0.143 \pm 0.026$
$(5s)^2\ {}^1\mathrm{S}_0 \rightarrow 5s5p\ {}^3\mathrm{P}_1\ F = 9/2$	0.90 ± 0.04	$+0.5 \pm 0.1$
$5s5p\ {}^3\mathrm{P}_0 \rightarrow (5p)^2\ {}^3\mathrm{P}_1\ F = 11/2$	3.6 ± 1.8	-0.5 ± 0.5
$5s5p\ {}^3\mathrm{P}_0 \rightarrow (5p)^2\ {}^3\mathrm{P}_1\ F = 9/2$	7 ± 3	-1.8 ± 1.8
$5s5p\ {}^3\mathrm{P}_0 \rightarrow 5s5d\ {}^3\mathrm{D}_1\ F = 11/2$	5.1 ± 2.6	-1.1 ± 1.1
$5s5p\ {}^3\mathrm{P}_0 \rightarrow 5s5d\ {}^3\mathrm{D}_1\ F = 9/2$	10 ± 5	-4 ± 4
$5s5p\ {}^3\mathrm{P}_0 \rightarrow 5s6s\ {}^3\mathrm{S}_1\ F = 11/2$	2.3 ± 1.2	-0.4 ± 0.4
$5s5p\ {}^3\mathrm{P}_0 \rightarrow 5s6s\ {}^3\mathrm{S}_1\ F = 9/2$	4.5 ± 2.2	-1.5 ± 1.6

Using the evaluated individual shifts, the total shift as well as the fractional total frequency shift are calculated

$$\frac{\delta_{\mathrm{ac,total}}^{(\mathrm{off-res})}}{2\pi} = (-0.3 \pm 0.6)\,\mu\mathrm{Hz} \tag{4.70}$$

$$\frac{\delta_{\mathrm{ac,total}}^{(\mathrm{off-res})}}{\omega_{\mathrm{clock}}} = (-2 \pm 5) \times 10^{-22}. \tag{4.71}$$

In the next subsection, the total probe field induced ac-Stark shift including the ellipticity induced shift presented in section 4.1.5 as well as the ac-Stark shit by off-resonant transitions is evaluated.

4.3 Evaluation of the total probe field induced ac-Stark shift

After the ellipticity induced shift $\delta_{\mathrm{ac}}^{(\mathrm{el-ind})}$ as well as the ac-Stark shift by off resonant transitions $\delta_{\mathrm{ac}}^{(\mathrm{off-res})}$ were determined in 4.1.5 and 4.2.2, the total resulting probe field induced shift $\delta_{\mathrm{ac}}^{(\mathrm{probe})}$ can be evaluated. Since frequency shifts in atomic clocks simply add up, $\delta_{\mathrm{ac}}^{(\mathrm{probe})}$ can be calculated by the sum of $\delta_{\mathrm{ac}}^{(\mathrm{el-ind})}$ and $\delta_{\mathrm{ac,total}}^{(\mathrm{off-res})}$ given in Eqs. 4.51 and 4.71

$$\frac{\delta_{\mathrm{ac}}^{(\mathrm{probe})}}{2\pi} = \frac{\delta_{\mathrm{ac}}^{(\mathrm{el-ind})} + \delta_{\mathrm{ac,total}}^{(\mathrm{off-res})}}{2\pi} = (-0.3 \pm 0.8)\,\mu\mathrm{Hz} \tag{4.72}$$

resulting in a fractional frequency shift of

$$\frac{\delta_{\mathrm{ac}}^{(\mathrm{probe})}}{\omega_{\mathrm{clock}}} = (-2 \pm 6) \times 10^{-22}. \tag{4.73}$$

4.4 Summary

This chapter presented the analysis of two contributions to the probe field induced ac-Stark shift, namely the ellipticity induced ac-stark shift and the ac-Stark shift by off-resonant transitions. As shown by Yudin et. al [18], the ellipticity induced shift originates from an unwanted ellipticity of the probe field as well as a misorientation of the bias magnetic field, which are described by the parameters ϵ and ξ. A first estimate of these experimental imperfections resulted in $|\epsilon\xi|_{\mathrm{est}} \approx 2 \times 10^{-3}$. Using this estimate, a first comparative analysis of the shift for different clock experiments was done. The calculated shift are in the low to mid 10^{-21} region for all considered clock species, the lowest value of $\approx 1.6 \times 10^{-22}$ was determined for the indium clock at PTB. It was also shown that $^{115}\mathrm{In}^{+}$ is a favorable species, since it shows the lowest intrinsic shift sensitivity among all compared species. In an experimental analysis based on clock spectroscopy in the indium clock setup, an upper bound for $|\epsilon\xi|_{\mathrm{max}} \leq (2.7 \pm 1.9) \times 10^{-4}$ was determined. Finally, based on the experimental results, the fractional ellipticity induced shift for the indium clock was determined to be $(0 \pm 4) \times 10^{-22}$.
Afterwards, the ac-Stark shift by far off-resonant transitions was determined based on a theoretical analysis. Since the ac-Stark shift is proportional to the square of the probe field strength, E_{probe} was determined. Afterwards, dipole matrix elements for various far-off resonant transitions in $^{115}\mathrm{In}^{+}$ were calculated to estimate their contribution to the total ac-Stark shift. It was shown that, neglecting hyperfine structure, only 5 finestructure transitions yield a shift on the order of $10^{-21} - 10^{-22}$. With these five transitions, a more rigorous analysis was done. The analysis took into account the hyperfine structure as well as, using results of the analysis of the ellipticity induced shift, the polarization state of the probe field. Here the ac-Stark shift by far off-resonant transitions was determined to be $(-2 \pm 5) \times 10^{-22}$.
Finally, the total fractional probe field induced ac-Stark shift was determined to be $(-2 \pm 6) \times 10^{-22}$ as the sum of both analyzed shifts.

5 Modelling and analysis of sympathetic Doppler cooling

As presented in chapter 2, the clock ion temperature has a major impact on the performance of an atomic clock by means of e.g. the temperature related loss of contrast (maximum excited state population $|c_e|^2$, see 2.6) or the thermal time dilation shift (see 2.3.1). In addition, the axial temperature cannot be determined from Rabi flops due to a missing projection of the clock laser onto the trap axis. This motivates a thorough theoretical ion temperature analysis for the indium clock. Such an analysis is carried out in this chapter based on a model for sympathetic Doppler cooling described by Keller et al. [19]. While in [19] the model is restricted to a single cooling beam with a fixed orientation relative to the trap axes, here it is extended to multiple cooling beams with arbitrary orientation and applied to the experimental conditions in the indium setup. The theoretical model and its extension will be subject of section 5.1. In section 5.2, the model will be used to simulate and analyze the ion temperatures for the clock sequence used in the spring 2022 clock campaign (see Fig. 3.3). Based on the results of section 5.2, possible improvements of selected phases in the clock sequence are investigated in section 5.3.

5.1 Theoretical Model

This section presents the theoretical model used to simulate sympathetic Doppler cooling in the indium clock setup. The section is structured as follows. In 5.1.1, the basic model as presented in [19] is introduced. 5.1.2 presents the extensions of the model to multiple cooling beams and the application to the experimental conditions in the indium clock setup. Afterwards, in 5.1.3, the model is further simplified, while in 5.1.4, the validity of fundamental assumptions made in [19] is investigated. Lastly, 5.1.5 presents the calculation of important parameters needed for the following simulations in sections 5.2 and 5.3.

5.1.1 Rate equation model for sympathetic mode cooling

The energy $E_{j\alpha}$ of a mode α along the principal axis[5] j in the process of sympathetic Doppler cooling is affected by three rates, such that the temporal change is given by

$$\frac{\mathrm{d}}{\mathrm{d}t}E_{j\alpha} = \dot{E}_{j\alpha} = \dot{E}_{\mathrm{cool,laser},j\alpha} + \dot{E}_{\mathrm{heat,laser},j\alpha} + \dot{E}_{\mathrm{heat,ext},j\alpha}. \tag{5.1}$$

Here $\dot{E}_{\mathrm{cool,laser},j\alpha}$ is the cooling rate as a measure for the dissipated thermal energy per unit time and $\dot{E}_{\mathrm{heat,laser},j\alpha}$ the heating rate which accounts for heating due to photon absorption and spontaneous emission. Besides these two rates which originate from interaction of the cooling laser with the cooling ions, there is an additional heating rate $\dot{E}_{\mathrm{heat,ext},j\alpha}$. This rate describes the non-laser-related heating originating e.g. from stray electric fields. Usual Doppler cooling times are on the order of ms (see section 3.3) while the oscillation periods in the trap are on the order of tens of μs. Therefore, it is convenient to average $\dot{E}_{\mathrm{cool,laser},j\alpha}$ and $\dot{E}_{\mathrm{cool,laser},j\alpha}$ and hence neglect changes on the timescales smaller than an oscillation period. The time average of the aforementioned rates are then given by

$$\langle \dot{E} \rangle_{\mathrm{cool,laser},j\alpha} = \Gamma_{\mathrm{sc},0} k_B T_{j\alpha} \hbar k_j \rho_j \frac{1}{m_{\mathrm{ion,cool}}} \underbrace{\sum_{i=1}^{N_{\mathrm{cool}}} \beta'^2_{j\alpha,i}}_{:=C_{j\alpha}} \tag{5.2}$$

$$\langle \dot{E} \rangle_{\mathrm{heat,laser},j\alpha} = \frac{\Gamma_{\mathrm{sc},0}}{2} \Big(\underbrace{\hbar^2 k_j^2}_{\propto \mathrm{absorption}} + \underbrace{\hbar^2 k^2 \xi_j}_{\propto \mathrm{emission}} \Big) \frac{C_{j\alpha}}{m_{\mathrm{ion,cool}}}. \tag{5.3}$$

[5] To avoid confusion with $k-$vector components k, the principal axes index k introduced in section 2.4.2 is renamed j.

Here k_B is the Boltzmann constant, $m_{\text{ion,cool}}$ the mass of the contributing cooling ions in the Coulomb crystal, k_j the projection of the cooling laser $k-$vector $\mathbf{k}$ ($k = |\mathbf{k}|$) onto the mode principal axis j and $C_{j\alpha}$ defined as the sum of squared mass-weighted-space mode eigenvector components $\beta'_{j\alpha,i}$ as presented in section 2.4.3. Moreover, there is the scattering rate $\Gamma_{\text{sc},0}$ and the friction coefficient ρ_j defined as

$$\Gamma_{\text{sc},0} = \frac{\Gamma}{2}\frac{s}{1+s+(\frac{2\Delta_0}{\Gamma})^2} \tag{5.4}$$

$$\rho_j = \frac{8k_j\Delta_0}{\Gamma^2(1+s+(\frac{2\Delta_0}{\Gamma})^2)}, \tag{5.5}$$

with the natural linewidth Γ and saturation parameter s of the cooling transition as well as the detuning $\Delta_0 = \omega_L - \omega_0 \approx -\Gamma/2$ of the cooling laser frequency ω_L with respect to the cooling transition center frequency ω_0. Both expressions result from a linearization of each cooling ion's scattering rate $\Gamma_{\text{sc},i}$ (by analogy with the treatment of a single trapped ion in [31])

$$\begin{aligned}\Gamma_{\text{sc},i} &= \frac{\Gamma}{2}\frac{s}{1+s+\left(\frac{2(\Delta_0-\mathbf{k}\sum_{j,\alpha}\mathbf{v}_{j\alpha,i}}{\Gamma}\right)^2} \\ &\approx \Gamma_{\text{sc},0}(1+\sum_{j,\alpha}\rho_j v_{j\alpha,i}),\end{aligned} \tag{5.6}$$

in the ion's oscillation velocity $|\mathbf{v}_i| = |\sum_{j,\alpha}\mathbf{v}_{j\alpha,i}|$ where $\mathbf{v}_{j\alpha,i}$ is the component of $\mathbf{v}_i$ describing the velocity of the motion in the mode α along the principal axis j. The mode velocities are given by

$$|\mathbf{v}_{j\alpha,i}| = v_{0,j\alpha,i}\,|\cos(\omega_{j\alpha}t+\varphi_{j\alpha})|, \tag{5.7}$$

with the peak oscillation velocity

$$v_{0,j\alpha,i} = |\beta'_{j\alpha,i}|\sqrt{\frac{2k_BT_{j\alpha}}{m_{\text{ion,cool}}}}. \tag{5.8}$$

Here $T_{j\alpha}$ is the mode temperature. Note that the cosine in $\mathbf{v}_{j\alpha,i}$ originates from the oscillatory motion along each mode principal axis. The linearization is justified by the assumption that the 1st order Doppler shift $|\delta_{\text{1D},i}| = |\mathbf{k}\sum_{j,\alpha}\mathbf{v}_{j\alpha,i}| = |\sum_{j,\alpha}k_jv_{j\alpha,i}| \ll |\Delta_0|$, which will be discussed further in subsection 5.1.4. By having a closer look at the heating rate in Eq. 5.3, one can see that it is given by two terms $\propto k_j^2$ and $\propto k^2\xi_j$. The first term $\propto k_j^2$ describes heating due to absorption. The proportionality results from the fact that only the component $\hbar\mathbf{k}_j$ of the absorbed photon momentum $\hbar\mathbf{k}$ parallel to the mode principal axis j contributes to heating[6]. The second term $\propto k\xi_j$ describes heating due to the spontaneous emission, where the geometric factor ξ_j covers the angular dependence of the cooling transition's emission pattern with respect to the mode principal axis. For a spherically symmetric emission pattern, $\xi_j = 1/3$, as will be shown in subsection 5.1.5.

Since the motion along one of the mode principal axes can be described by a 1D harmonic oscillator,

$$\langle E\rangle = k_BT$$

holds. Hence by division of $\langle\dot{E}\rangle_{j\alpha}$ by k_B a differential equation for the mode temperature $T_{j\alpha}$ is obtained

$$\frac{\langle\dot{E}\rangle_{j\alpha}}{k_B} = \dot{T}_{j\alpha} = \underbrace{\Gamma_{\text{sc},0}\hbar k_j\rho_j\frac{C_{j\alpha}}{m_{\text{ion,cool}}}}_{:=c_{1,j\alpha}}T_{j\alpha} + \underbrace{\frac{\Gamma_{\text{sc},0}}{2k_B}(\hbar^2k_j^2+\hbar^2k^2\xi_j)\frac{C_{j\alpha}}{m_{\text{ion,cool}}} + \frac{1}{k_B}\dot{E}_{\text{heat,ext,j}\alpha}}_{:=c_{0,j\alpha}}, \tag{5.9}$$

$$\Rightarrow \dot{T}_{j\alpha} = c_{1,j\alpha}T_{j\alpha} + c_{0,j\alpha}, \tag{5.10}$$

[6]Note that the same argument holds for the cooling rate $\langle\dot{E}\rangle_{\text{cool,laser},j\alpha} \propto k_j^2$.

where $c_1 < 0$ for $\Delta_0 < 0$ and $c_0 > 0$ are the cooling and heating coefficients. It can be shown that the general solution to the derived differential equation in Eq. 5.10 is given by

$$T_\alpha(t) = \left[T_{j\alpha}(t_0) + \frac{c_{0,j\alpha}}{c_{1,j\alpha}} e^{c_{1,j\alpha} t_0}\right] e^{c_{1,j\alpha} t} - \frac{c_{0,j\alpha}}{c_{1,j\alpha}}. \tag{5.11}$$

Choosing the initial time $t_0 = 0\,\mathrm{s}$, the solution simplifies to

$$T_{j\alpha}(t) = \left[\underbrace{T_{j\alpha}(t_0)}_{=T_{\mathrm{ini},j\alpha}} + \frac{c_{0,j\alpha}}{c_{1,j\alpha}}\right] e^{c_{1,j\alpha} t} \underbrace{- \frac{c_{0,j\alpha}}{c_{1,j\alpha}}}_{:=T_{\mathrm{eq},j\alpha}} \tag{5.12}$$

$$= \left[T_{\mathrm{ini,j}\alpha} - T_{\mathrm{eq},j\alpha}\right] e^{c_{1,j\alpha} t} + T_{\mathrm{eq},j\alpha}, \tag{5.13}$$

where $T_{\mathrm{ini},j\alpha}$ is the initial temperature and $T_{\mathrm{eq},j\alpha}$ the equilibrium temperature for cooling times $t \to \infty$, given by

$$T_{\mathrm{eq},j\alpha} = -\frac{\frac{\Gamma_{\mathrm{sc},0}}{2k_B}(\hbar^2 k_j^2 + \hbar^2 k^2 \xi_j)\frac{C_{j\alpha}}{m_{\mathrm{ion,cool}}} + \frac{1}{k_B}\dot{E}_{\mathrm{heat,ext},j\alpha}}{\Gamma_{\mathrm{sc},0}\hbar k_j \rho_j \frac{C_{j\alpha}}{m_{\mathrm{ion,cool}}}} = -\frac{c_{0,j\alpha}}{c_{1,j\alpha}}. \tag{5.14}$$

Assuming a vanishing external heating rate, as will be discussed in subsection 5.1.3, the factor $C_{j\alpha}$ cancels such that there is no explicit dependence on the mode $j\alpha$. Therefore all modes along a given principal axis have the same equilibrium temperature. For a single cooling beam with equal projection on the three mode principal axes (i.e. $k_j = 1/\sqrt{3}k$), as well as a symmetric emission pattern ($\xi_j = 1/3$), the equilibrium temperature is equal to the well known Doppler limit T_D

$$T_{\mathrm{eq},j\alpha} = \frac{\hbar\Gamma}{2k_\mathrm{B}} = T_\mathrm{D} \tag{5.15}$$

in the limit $s \to 0$ [19]. For different cooling beam orientations, the equilibrium temperature can even be smaller. This was shown theoretically in [31] for cooling of a single trapped ion. The author assumed a single cooling beam parallel to a mode principle axis where the minimum temperature T_min along this axis is given by

$$T_\mathrm{min} = \frac{\hbar\Gamma\sqrt{1+s}}{4kB}(1+\xi_j) \overset{s\to 0}{\to} \frac{\hbar\Gamma}{4kB}(1+\xi_j) \overset{\xi_j<1}{<} T_\mathrm{D}, \tag{5.16}$$

which is smaller than T_D since $\xi_j < 1$.
If the cooling $c_{0/1} \equiv c_{0/1}(t)$ are assumed to be functions of time, e.g. for time dependent saturation parameters $s(t)$ as used in the cooling phase of the clock sequence (see Fig. 3.3), the solution of 5.10 is given by

$$T_{j\alpha}(t) = e^{\int_{t_0}^{t} c_{1,j\alpha}(t')\,dt'}\left[T_{\mathrm{ini},j\alpha} + \int_{t_0}^{t} c_{0,j\alpha}(t') e^{-\int_{t_0}^{t'} c_{1,j\alpha}(t'')\,dt''}\,dt'\right]. \tag{5.17}$$

Note that the assumed rate equation model is derived in the limit of small saturation $s \ll 1$, where absorption and emission processes can be considered uncorrelated [31]. A more rigorous treatment can be found e.g. in [48, 63]. To keep things simple, effects such as the mentioned correlations will be neglected throughout this thesis.
Since the general time dependence of the mode Temperature $T_{j\alpha}$ is now found, the model will be extended to multiple lasers and applied to the experimental conditions in the indium clock setup at PTB.

5.1.2 Extension of the model to multiple lasers in the $^{115}In^+$ clock setup

In the following, the cooling coefficients $c_{0/1}$ for the axial modes and the modes of both radial axes are derived. As shown in 3.2, there are three Yb^+ cooling beams addressing the Doppler cooling transition at $\approx 370\,\text{nm}$ which are named H1, H2 and V. Although the indium detection beam at $\approx 230.6\,\text{nm}$, named 230, is not intentionally used for cooling yet, it contributes to the time evolution of the mode temperatures. Therefore it needs to be taken into account. For all the beams, the $k-$vector projections k_j on the principal axes need to be determined. The orientation of the beams in the xz- and xy-plane relative to the trap axis with secular frequency ν_{ax} and radial principal axes frequencies ν_{rad1} and ν_{rad2} are shown in Fig. 5.1. In addition, each projection of the $k-$vectors $\mathbf{k}_{\text{H1}}$, $\mathbf{k}_{\text{H2}}$, $\mathbf{k}_{\text{V}}$ and $\mathbf{k}_{230}$ on the principal trap axes are shown as transparent arrows. Here φ is the relative angle between H1/H2 and the radial principal axis (parallel to the $z-$axis) and θ the relative angle between V and the radial principal axis ν_{rad1}.

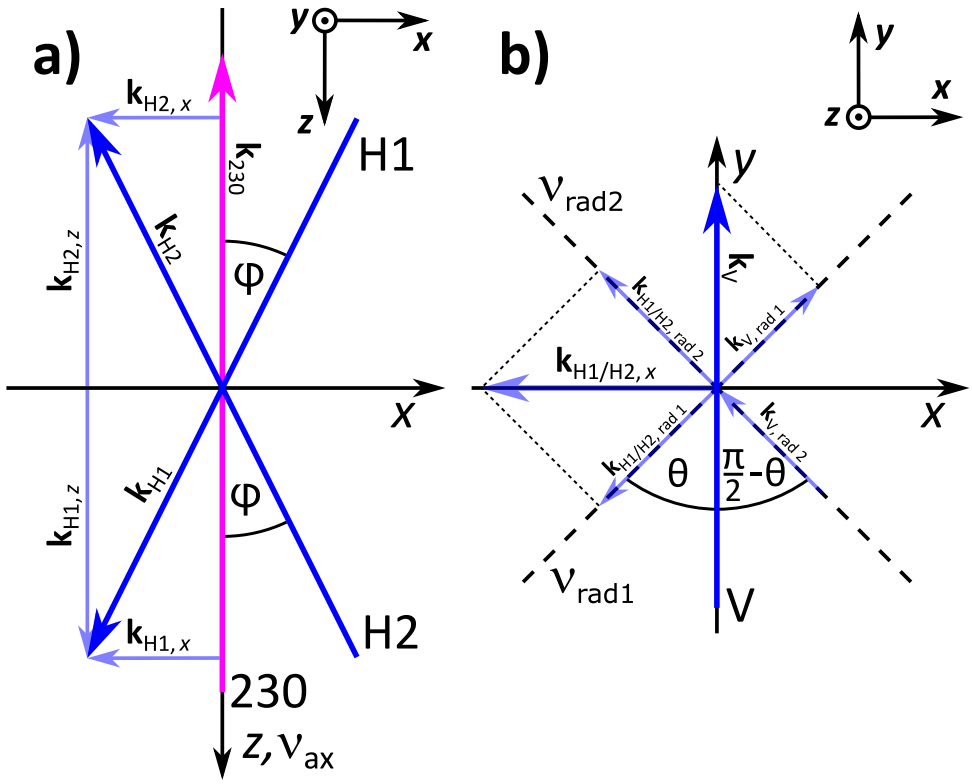

Figure 5.1 Projections of the ytterbium Doppler cooling and indium detection beams onto the principal trap axes. a) Both Doppler cooling beams H1 and H2 (dark blue) have an angle of $\varphi = 23°$ relative to the trap axis with secular frequency ν_{ax}. Each beam's $k-$vector projections onto the experiments $x-$ and $z-$axis are shown as transparent blue arrows. The indium detection beam 230 (pink) is parallel to z and hence the trap axis. b) For the indium detection beam 230 there is no projection onto the radial axes with secular frequencies $\nu_{\text{rad1/2}}$ (dashed bars). The orientation of the radial trap axes is described by the angle θ relative to the vertical Doppler cooling beam V (dark blue). The $k-$vector projections of H1, H2 and V are again highlighted by transparent blue arrows.

As can be seen in Fig. 5.1 a), the 230 beam is oriented parallel to the trap axis ν_{ax}, its projection is independent of φ and θ

$$k_{230,\text{ax}} = k_{230} = |\mathbf{k}_{230}| = \frac{2\pi}{\lambda_{230}}. \tag{5.18}$$

Because all trap axes are orthogonal, there is no projection on the radial trap axes ν_{rad1} and

ν_{rad2}. The projections of H1 and H2 onto ν_{ax} can be calculated to be

$$k_{\mathrm{H1/H2,ax}} = k_{\mathrm{H1/H2,z}} = \cos(\varphi)|\mathbf{k}_{\mathrm{H1}}| = \cos(\varphi)k_{370}, \tag{5.19}$$

while the projection onto the x-axis is

$$k_{\mathrm{H1/H2,x}} = \sin(\varphi)k_{370}. \tag{5.20}$$

Note that H1, H2 and V originate from the same laser source and hence

$$|\mathbf{k}_{\mathrm{H1}}| = |\mathbf{k}_{\mathrm{H2}}| = |\mathbf{k}_{\mathrm{V}}| = k_{370} = \frac{2\pi}{\lambda_{370}}. \tag{5.21}$$

From Fig. 5.1 b), one finds that the projection of H1 and H2 onto the radial axes can be determined by

$$k_{\mathrm{H1/H2,rad1}} = \cos\left(\frac{\pi}{2} - \theta\right) k_{\mathrm{H1/H2,x}} = \sin(\theta)\sin(\varphi)k_{370} \tag{5.22}$$

$$k_{\mathrm{H1/H2,rad2}} = \cos(\theta)k_{\mathrm{H1/H2,x}} = \cos(\theta)\sin(\varphi)k_{370}. \tag{5.23}$$

For V, there is no projection onto the trap axis and the projections onto the two radial axes are given by

$$k_{\mathrm{V,rad1}} = \cos(\theta)k_{370} \tag{5.24}$$

$$k_{\mathrm{V,rad2}} = \sin(\theta)k_{370}. \tag{5.25}$$

Besides the projections, the individual scattering rates originating from each laser need to be found. Since there are multiple 370 nm beams interacting with the cooling ions, each (ytterbium) ion scatters photons with an effective scattering rate $\Gamma_{\mathrm{sc,eff}}$. This scattering rate originates from the sum of all saturations s of the contributing cooling beams. The effective saturation s_{eff} is (since $s \propto I$) therefore given by the sum of all saturations $s_{\mathrm{H1}}, s_{\mathrm{H2}}$ and s_{V} of H1, H2 and V (see [48])

$$s_{\mathrm{eff}} = s_{\mathrm{H1}} + s_{\mathrm{H1}} + s_{\mathrm{V}}. \tag{5.26}$$

Using this effective saturation, $\Gamma_{\mathrm{sc,eff}}$ can be calculated using Eq. 5.4

$$\Gamma_{\mathrm{sc,eff}} = \frac{\Gamma_{370}}{2} \frac{s_{\mathrm{eff}}}{1 + s_{\mathrm{eff}} + (\frac{2\Delta_{0,370}}{\Gamma})^2}, \tag{5.27}$$

where $\Gamma_{370} = 2\pi \times 19.6\,\mathrm{MHz}$ is the natural linewidth of the cooling transition and $\Delta_{0,370} \approx -\Gamma_{370}/2$. The fraction of $\Gamma_{\mathrm{sc,eff}}$ originating from each cooling beam can now be calculated from the ratio between each beam's saturation and the effective saturation. Hence the scattering rates due to the beams H1, H2 and V yield

$$\Gamma_{\mathrm{sc,H1}} = \Gamma_{\mathrm{sc,eff}} \frac{s_{\mathrm{H1}}}{s_{\mathrm{eff}}} = \frac{\Gamma_{370}}{2} \frac{s_{\mathrm{H1}}}{1 + s_{\mathrm{eff}} + (\frac{2\Delta_{0,370}}{\Gamma})^2} \tag{5.28}$$

$$\Gamma_{\mathrm{sc,H2}} = \Gamma_{\mathrm{sc,eff}} \frac{s_{\mathrm{H2}}}{s_{\mathrm{eff}}} = \frac{\Gamma_{370}}{2} \frac{s_{\mathrm{H2}}}{1 + s_{\mathrm{eff}} + (\frac{2\Delta_{0,370}}{\Gamma})^2} \tag{5.29}$$

$$\Gamma_{\mathrm{sc,V}} = \Gamma_{\mathrm{sc,eff}} \frac{s_{\mathrm{V}}}{s_{\mathrm{eff}}} = \frac{\Gamma_{370}}{2} \frac{s_{\mathrm{V}}}{1 + s_{\mathrm{eff}} + (\frac{2\Delta_{0,370}}{\Gamma})^2}. \tag{5.30}$$

Since there is just one beam interacting with the indium ions, the corresponding scattering rate is given by

$$\Gamma_{\mathrm{sc,230}} = \frac{\Gamma_{230}}{2} \frac{s_{230}}{1 + s_{230} + (\frac{2\Delta_{0,230}}{\Gamma})^2}. \tag{5.31}$$

Here s_{230} is the saturation coefficient of the 230 beam, $\Gamma_{230} = 2\pi \times 360\,\text{kHz}$ is the natural linewidth of the indium detection transition and $\Delta_{0,230} \approx -\Gamma_{230}/2$.
With the above projections of the $k-$vectors as well as the scattering rates for all beams, the cooling and heating coefficients c_1 and c_0 can be defined for each principal axis.
For the definition, it is assumed that the coefficients can be calculated by summing up the individual cooling and heating coefficients originating from each beam. This assumption is justified by the fact that there is no interference between two or more beams which could lead to a time dependent modulation of the intensity at the ion position and hence a modulation of the saturation. Of course, H1 and H2 are not orthogonal, but as can be seen in the clock sequence scheme in Fig. 3.3, never switched on simultaneously. Moreover, since 230 and the other 370 nm beams are far detuned from each other, there is also no interference. A more rigorous approach including the effect of interference can be found in [48].
At first, the heating coefficients are derived. Using the definition of c_0 in Eq. 5.9, $c_{0,\text{rad1/2}}$ for the modes of radial trap axes $\nu_{\text{rad1/2}}$ are given by

$$c_{0,\text{rad1/2},\alpha} = \frac{1}{k_B}\dot{E}_{\text{heat,ext,rad1/2},\alpha} + c_{0,\text{rad1/2},370,\alpha} + c_{0,230,\alpha} \tag{5.32}$$

with the external heating rates of the radial modes $\dot{E}_{\text{heat,ext,rad1/2},\alpha}$ and laser specific heating coefficients

$$\begin{aligned} c_{0,\text{rad1/2},370,\alpha} &= \frac{1}{k_B}\hbar^2(\Gamma_{\text{sc,H1}}k^2_{\text{H1,rad1/2}} + \Gamma_{\text{sc,H2}}k^2_{\text{H2,rad1/2}} + \Gamma_{\text{sc,V}}k^2_{\text{V,rad1/2}} \\ &\quad + \Gamma_{\text{sc,eff}}k^2_{370}\xi_{\text{Yb,rad}})\frac{1}{m_{\text{Yb}}}\underbrace{\sum_{i=1}^{N_{\text{Yb}}}\beta'^2_{\text{Yb,rad1/2},\alpha,i}}_{:=C_{\text{Yb,rad1/2},\alpha}} \end{aligned} \tag{5.33}$$

$$\begin{aligned} &= \frac{1}{k_B}\frac{\Gamma_{\text{sc,eff}}}{s_{\text{eff}}}\hbar^2(s_{\text{H1}}k^2_{\text{H1,rad1/2}} + s_{\text{H2}}k^2_{\text{H2,rad1/2}} + s_{\text{V}}k^2_{\text{V,rad1/2}} \\ &\quad + s_{\text{eff}}k^2_{370}\xi_{\text{Yb,rad}})\frac{C_{\text{Yb,rad1/2},\alpha}}{m_{\text{Yb}}} \end{aligned} \tag{5.34}$$

$$c_{0,\text{rad1/2},230,\alpha} = \frac{1}{k_B}\Gamma_{\text{sc,230}}\hbar^2 k^2_{230}\xi_{\text{In,rad}}\frac{1}{m_{\text{In}}}\underbrace{\sum_{j=1}^{N_{\text{In}}}\beta'^2_{\text{In,rad1/2},\alpha,j}}_{:=C_{\text{In,rad1/2},\alpha}}. \tag{5.35}$$

Here $\xi_{\text{Yb,rad}} = 1/3$ and $\xi_{\text{In,rad}} = 3/10$ are the geometric factors for spontaneous emission for the radial trap axes. Both factors take into account the emission patterns of the ytterbium cooling and indium detection transition as will be shown in subsection 5.1.5. Note that there is no term for heating by photon absorption in $c_{0,230}$, since the 230 beam has no projection onto the radial trap axes. For the cooling parameters $c_{1,\text{rad1/2}}$ the friction coefficients ρ (see Eq. 5.5) need to be defined for each laser. They are given by

$$\rho_{\text{H1,rad1/2}} = \frac{8k_{\text{H1,rad1/2}}\Delta_{0,370}}{\Gamma^2_{370}(1 + s_{\text{eff}} + (\frac{2\Delta_0}{\Gamma_{370}})^2)} \tag{5.36}$$

$$\rho_{\text{H2,rad1/2}} = \frac{8k_{\text{H2,rad1/2}}\Delta_{0,370}}{\Gamma^2_{370}(1 + s_{\text{eff}} + (\frac{2\Delta_0}{\Gamma_{370}})^2)} \tag{5.37}$$

$$\rho_{\text{V,rad1/2}} = \frac{8k_{\text{V,rad1/2}}\Delta_{0,370}}{\Gamma^2_{370}(1 + s_{\text{eff}} + (\frac{2\Delta_0}{\Gamma_{370}})^2)}. \tag{5.38}$$

Note that the saturation coefficient in the denominator is given by s_{eff}, not by the beam specific coefficient s_{H1}, s_{H2} or s_{V}. This can be explained by the fact that the friction coefficient ρ results from a Taylor expansion of the total scattering rate Γ_{sc} in Eq. 5.6 (for $s = s_{\text{eff}}$). Or from the physical point of view, the transition saturates independent of the incident direction of the photons.
With the given friction coefficients and the definition of c_1 in Eq. 5.9, the cooling coefficients $c_{1,\text{rad1/2}}$ become

$$\begin{aligned} c_{1,\text{rad1/2},\alpha} &= \hbar(\Gamma_{\text{sc,H1}} k_{\text{H1,rad1/2}} \rho_{\text{H1,rad1/2}} + \Gamma_{\text{sc,H2}} k_{\text{H2,rad1/2}} \rho_{\text{H2,rad1/2}} \\ &\quad + \Gamma_{\text{sc,V}} k_{\text{V,rad1/2}} \rho_{\text{V,rad1/2}}) \frac{C_{\text{Yb,rad1/2},\alpha}}{m_{\text{Yb}}} \end{aligned} \tag{5.39}$$

$$\begin{aligned} &= \frac{\Gamma_{\text{sc,eff}}}{s_{\text{eff}}} \hbar(s_{\text{H1}} k_{\text{H1,rad1/2}} \rho_{\text{H1,rad1/2}} + s_{\text{H2}} k_{\text{H2,rad1/2}} \rho_{\text{H2,rad1/2}} \\ &\quad + s_{\text{V}} k_{\text{V,rad1/2}} \rho_{\text{V,rad1/2}}) \frac{C_{\text{Yb,rad1/2},\alpha}}{m_{\text{Yb}}}. \end{aligned} \tag{5.40}$$

For the temperature dynamics of the axial modes, the situation is different. There is no contribution of V to the cooling coefficient $c_{1,\text{ax},\alpha}$, because V is orthogonal to the axial modes. Hence, V only contributes via heating by spontaneous emission. On the other hand, the 230 beam is parallel to the axial modes and therefore contributes to cooling and heating during the indium detection. Again, starting with the heating coefficient, $c_{0,\text{ax},\alpha}$ is given by

$$c_{0,\text{ax},\alpha} = \frac{1}{k_B} \dot{E}_{\text{heat,ext,ax},\alpha} + c_{0,\text{ax},370,\alpha} + c_{0,230,\alpha} \tag{5.41}$$

with the external heating rate $\dot{E}_{\text{heat,ext,ax},\alpha}$ for the axial modes and laser specific coefficients defined by

$$c_{0,\text{ax},370,\alpha} = \frac{1}{k_B} \hbar^2 (\Gamma_{\text{sc,H1}} k_{\text{H1,ax}}^2 + \Gamma_{\text{sc,H2}} k_{\text{H2,ax}}^2 + \Gamma_{\text{sc,eff}} k_{370\,\text{nm}}^2 \xi_{\text{Yb,ax}}) \frac{1}{m_{\text{Yb}}} \underbrace{\sum_{i=1}^{N_{\text{Yb}}} \beta'^2_{\text{Yb,ax},\alpha,i}}_{:=C_{\text{Yb,ax},\alpha}} \tag{5.42}$$

$$= \frac{1}{k_B} \frac{\Gamma_{\text{sc,eff}}}{s_{\text{eff}}} \hbar^2 (s_{\text{H1}} k_{\text{H1,ax}}^2 + s_{\text{H2}} k_{\text{H2,ax}}^2 + s_{\text{V}} k_{\text{V,ax}}^2 + s_{\text{eff}} k_{370\,\text{nm}}^2 \xi_{\text{Yb,ax}}) \frac{C_{\text{Yb,ax},\alpha}}{m_{\text{Yb}}} \tag{5.43}$$

$$c_{0,\text{ax},230,\alpha} = \frac{1}{k_B} \Gamma_{\text{sc,230}} \hbar^2 k_{230}^2 (1 + \xi_{\text{In,ax}}) \frac{1}{m_{\text{In,ax}}} \underbrace{\sum_{j=1}^{N_{\text{In}}} \beta'^2_{\text{In,ax},\alpha,j}}_{:=C_{\text{In,ax},\alpha}}. \tag{5.44}$$

where $\xi_{\text{Yb,ax}} = 1/3$ and $\xi_{\text{In,ax}} = 2/5$ are the geometric factors for the axial modes (see subsection 5.1.5). For the cooling parameter, again the friction coefficients ρ need to be defined. They are given by

$$\rho_{\text{H1,ax}} = \frac{8 k_{\text{H1,ax}} \Delta_{0,370}}{\Gamma_{370}^2 (1 + s_{\text{eff}} + (\frac{2\Delta_{0,370}}{\Gamma_{370}})^2)} \tag{5.45}$$

$$\rho_{\text{H2,ax}} = \frac{8 k_{\text{H2,ax}} \Delta_{0,370}}{\Gamma_{370}^2 (1 + s_{\text{eff}} + (\frac{2\Delta_{0,370}}{\Gamma_{370}})^2)} \tag{5.46}$$

$$\rho_{230} = \frac{8 k_{230} \Delta_{0,230}}{\Gamma_{230}^2 (1 + s_{230} + (\frac{2\Delta_{0,230}}{\Gamma_{230}})^2)}. \tag{5.47}$$

Using these, axial cooling is described by

$$c_{1,\text{ax},\alpha} = c_{1,\text{ax},370,\alpha} + c_{1,\text{ax},230,\alpha} \tag{5.48}$$

with

$$c_{1,\mathrm{ax},370,\alpha} = \hbar(\Gamma_{\mathrm{sc,H1}} k_{\mathrm{H1,ax}} \rho_{\mathrm{H1,ax}} + \Gamma_{\mathrm{sc,ax}} k_{\mathrm{H2,ax}} \rho_{\mathrm{H2,ax}}) \frac{C_{\mathrm{Yb,ax},\alpha}}{m_{\mathrm{Yb}}} \tag{5.49}$$

$$= \frac{\Gamma_{\mathrm{sc,eff}}}{s_{\mathrm{eff}}} \hbar(s_{\mathrm{H1}} k_{\mathrm{H1,ax}} \rho_{\mathrm{H1,ax}} + s_{\mathrm{H2}} k_{\mathrm{H2,ax}} \rho_{\mathrm{H2,ax}}) \frac{C_{\mathrm{Yb,ax},\alpha}}{m_{\mathrm{Yb}}} \tag{5.50}$$

$$c_{1,\mathrm{ax},230,\alpha} = \hbar(\Gamma_{\mathrm{sc},230} k_{230} \rho_{230}) \frac{C_{\mathrm{In,ax},\alpha}}{m_{\mathrm{In}}}. \tag{5.51}$$

By inserting the respective total cooling and heating coefficients for the axial and radial modes into Eq. 5.12, the time dependence of the mode Temperatures $T_{\mathrm{ax},\alpha}(t)$ and $T_{\mathrm{rad1/2},\alpha}(t)$ in the indium clock setup is fully described in the framework of the assumed model. This time dependence will be used extensively to analyze the mode temperatures during the spring clock campaign in section 5.1 and afterwards in section 5.3 to investigate possible optimizations regarding e.g. cooling time and end temperatures of the Doppler cooling phase. In the next subsection, the magnitude of the external heating rates $\dot{E}_{\mathrm{heat,ext,rad},\alpha}$ and $\dot{E}_{\mathrm{heat,ext,ax},}\alpha$ are analyzed.

5.1.3 Estimate of external heating rates

External heating is predominantly induced by unwanted stray fields which originate predominantly from the trap electrodes. In [19], Keller et al. measured the radial heating using a single trapped ytterbium ion

$$\dot{\overline{n}}_{\mathrm{rad}} = 2.8 \times 10^{11}\, s^{-1} \frac{\mathrm{Hz}^2}{\nu_{\mathrm{rad}}^2}, \tag{5.52}$$

where $\overline{n}$ is the mean phonon occupation number of the radial modes. The connection to the heating rate $\dot{E}_{\mathrm{heat,ext,rad},\alpha}$ is given by

$$\dot{E}_{\mathrm{heat,ext,rad},\alpha} = \dot{\overline{n}}_{\mathrm{rad}} \hbar \omega_{\mathrm{rad}} = \dot{\overline{n}}_{\mathrm{rad}} h \nu_{\mathrm{rad}}. \tag{5.53}$$

$\dot{\overline{n}}_{\mathrm{rad}}$ was determined using a radial secular frequency $\nu_{\mathrm{rad}} = 500\,\mathrm{kHz}$, such that

$$\dot{E}_{\mathrm{heat,ext,rad},\alpha} = \frac{1.12}{\mathrm{s}} h \times 500\,\mathrm{kHz} \approx 4 \times 10^{-28}\, \frac{\mathrm{J}}{\mathrm{s}}. \tag{5.54}$$

In the process of photon emission during Doppler cooling, the photons recoil energy increases the thermal energy of the ion by

$$E_{\mathrm{rec}} = \frac{\hbar^2 k^2}{2 m_{\mathrm{ion}}}, \tag{5.55}$$

which is $E_{\mathrm{rec},370} \approx 5 \times 10^{-30}\mathrm{J}$ in case of the ytterbium cooling transition. Assuming that this energy is equally distributed to the modes of the three principal axes, as well as a scattering rate on the order of MHz, the radial and axial heating rates due to photon emission are estimated to be

$$\dot{E}_{\mathrm{heat,emiss,rad},\alpha} \propto \dot{E}_{\mathrm{heat,emiss,ax},\alpha} \propto \frac{5 \times 10^{-30}\mathrm{J} \times 1\,\mathrm{Hz}}{3} \approx 1.7 \times 10^{-24} \frac{\mathrm{J}}{\mathrm{s}} \tag{5.56}$$

which is more than three orders of magnitude larger than the external radial heating rate. Regarding the fact that radial secular frequencies were $\nu_{\mathrm{rad1/2}} \approx 800\,\mathrm{kHz}$ in the spring clock campaign, the corresponding external heating rate is even smaller.
The external heating of the axial modes can be estimated using a rate of $\dot{\overline{n}}_{\mathrm{ax}} \approx 5/s$ determined by Kalincev et al. in [64] for an axial secular frequency of $\approx 200\,\mathrm{kHz}$, close to the axial frequency $\nu_{\mathrm{ax}} = 275\,\mathrm{kHz}$ used during the spring clock campaign. This measurement was done with an ion trap of the same type. Therefore, the external radial heating rate in the indium setup is estimated to be

$$\dot{E}_{\mathrm{heat,ext,rad},\alpha} \approx \frac{5}{\mathrm{s}} h \times 275\,\mathrm{kHz} \approx 9 \times 10^{-28}\, \frac{\mathrm{J}}{\mathrm{s}} \ll \dot{E}_{\mathrm{heat,emiss,ax},\alpha}. \tag{5.57}$$

All above mentioned heating rates correspond to the center-of-mass (COM) mode where all ions are oscillating in phase (see e.g. the axial mode $\alpha = 1$ and the radial mode $\alpha = 4$ in Fig. 5.3). For all other modes, the external heating rates are further suppressed [65]. Since the estimated external heating rates are orders of magnitude smaller compared to the heating rate resulting from photon scattering, both are neglected throughout the application of the model.

5.1.4 Linearization of ion scattering rates for the In^+ detection and Yb^+ cooling transition

As presented in subsection 5.1.1, the model is simplified by a linearization of the scattering rate $\Gamma_{\mathrm{sc},i}$ (see Eq. 5.6) which holds for a 1st order Doppler shift of each ion $|\delta_{\mathrm{1D},i}| = |\sum_{j,\alpha} k_j v_{j\alpha,i}| \ll |\Delta_0|$. The validity of the linearization for the ytterbium cooling and indium detection transition are analyzed in the following.
For the analysis, the maximum mode temperatures $T_{j\alpha,\mathrm{max}}$ are calculated for which the condition $|\delta_{\mathrm{1D},i}| \leq |\Delta_0|$ is still satisfied. In principle, it is necessary to take into account all modes $j\alpha$ which contribute to the 1st order Doppler shift. Since the phases $\varphi_{j\alpha}$ in the mode velocities (see Eq. 5.7) are uncorrelated and unknown, it is not feasible to determine the shift and hence the maximum temperature for an ion number $i \geq 2$. Therefore, a single trapped ion is assumed. In this case $|\beta'_{j\alpha,i}| = 1$ and the cosine dependence is neglected and set to 1.
For the 370 nm cooling transition, the used detuning is $\Delta_{0,370} \approx -\Gamma_{370}/2 = -2\pi \times 9.8\,\mathrm{MHz}$. The maximum mode temperature $T_{\alpha,\mathrm{max,Yb}}$ can then be calculated via

$$k_j \sqrt{2k_B T_{j\alpha}/m_{\mathrm{Yb}}} \leq k_{370} \sqrt{2k_B T_{j\alpha}/m_{\mathrm{Yb}}} \stackrel{!}{=} |\Delta_{0,370}|^2 \tag{5.58}$$

$$\Leftrightarrow T_{j\alpha,\mathrm{max,Yb}} \leq \frac{|\Delta_{0,370}|^2 m_{\mathrm{Yb}}}{2k_{370}^2 k_B} \approx 136\,\mathrm{mK}. \tag{5.59}$$

As will be discussed in detail in the next section, the melting point of the ion crystal in the configuration used during the spring clock campaign is estimated to be $T_{\mathrm{melt}} \approx 18\,\mathrm{mK} \ll T_{j\alpha,\mathrm{max,Yb}}$ [66], above which the ions are not in a crystallized phase anymore. Therefore, the linearization of the ytterbium scattering rate is most likely valid.
For the indium ions and the 230.6 nm detection transition, the maximum temperature $T_{j\alpha,\mathrm{max,In}}$ can be calculated using the detuning $\Delta_{0,230} \approx -\Gamma_{230}/2 = 2\pi \times 180\,\mathrm{kHz}$, such that

$$T_{j\alpha,\mathrm{max,In}} \leq \frac{|\Delta_{0,230}|^2 m_{\mathrm{In}}}{2k_{230}^2 k_B} \approx 0.012\,\mathrm{mK}. \tag{5.60}$$

This is a crucial result. Since $T_{j\alpha,\mathrm{max,In}} \ll T_{\mathrm{melt}}$, the linearization cannot be applied to all times and hence all temperatures at which the ions are crystallized. Moreover, compared to the ytterbium Doppler temperature $T_{\mathrm{D,Yb}} \approx 0.47\,\mathrm{mK}$, it becomes clear that $T_{j\alpha,\mathrm{max,In}} < T_{\mathrm{D,Yb}}$. The condition $|\delta_{\mathrm{1D}}| \ll |\Delta_0|$ for the linearization can therefore only be fulfilled simultaneously for the indium and ytterbium ions and transitions when the axial mode temperatures $T_{\mathrm{ax},j\alpha} < T_{j\alpha,\mathrm{max,In}}$. Note that only the axial temperatures need to fulfill this condition since the 230 beam has no projection on the radial modes.
To check whether this is the case in the experiment, indium scattering rates observed during the spring clock campaign on the detection transition are compared to theoretical scattering rates for a vanishing 1st order Doppler shift.
At first, the scattering rate $\Gamma_{0,230}$ of a single indium ion (see Eq. 5.31) is calculated, which assumes a vanishing Doppler shift and hence $T_{\mathrm{ax},j\alpha} \ll T_{j\alpha,\mathrm{max,In}}$

$$\Gamma_{\mathrm{sc},230} = \frac{2\pi \times 360\,\mathrm{kHz}}{2} \frac{s_{230}}{1 + s_{230} + (\frac{2(\frac{360\,\mathrm{kHz}}{2})}{360\,\mathrm{kHz}})^2} = \frac{753982}{\mathrm{s}}. \tag{5.61}$$

Here the saturation coefficient is $s_{230} = 4$, which equals the saturation of the indium ion due to the 230 beam during the spring clock campaign. As presented in 3.2.4, ion scattering rates

are measured using PMTs. Here one needs to consider that only a small fraction of all scattered photons are collected by the detection system. This detection efficiency is described by a factor η_{det}. The factor contains all effects lowering the amount of collected photons such as the solid element of the ion emission pattern covered by the lens system, losses in optical components or the PMT's quantum efficiency[7]. To compare experimentally observed scattering rates with theoretical values as calculated above, η_{det} needs to be determined. In general, the relation

$$\Gamma_{\mathrm{sc,230,exp}} = \eta_{\mathrm{det}} \Gamma_{\mathrm{sc,230}} \tag{5.62}$$

holds. Therefore, η_{det} can be determined by the ratio of the experimentally observed scattering rate $\Gamma_{\mathrm{sc,230,exp}}$ and the theoretical scattering rate $\Gamma_{\mathrm{sc,230}}$ at a fixed saturation s_{230}

$$\eta_{\mathrm{det}} = \frac{\Gamma_{\mathrm{sc,230,exp}}}{\Gamma_{\mathrm{sc,230}}}. \tag{5.63}$$

To cancel the influence of the 1st order Doppler shift $|\delta_{\mathrm{1D}}|$ and hence the mode temperature T_α, one can use the fact that the ion's scattering rate saturates in the limit of high saturations s_{230}

$$\Gamma_{\mathrm{sc,230}} \overset{s \gg 1}{\rightarrow} \frac{\Gamma_{230}}{2} \tag{5.64}$$

$$\Gamma_{\mathrm{sc,230,exp}} \overset{s \gg 1}{\rightarrow} \Gamma_{\mathrm{sc,230,exp,max}}, \tag{5.65}$$

where $\Gamma_{\mathrm{sc,230,exp,max}}$ is the maximum experimentally observed PMT count rate. $\Gamma_{\mathrm{sc,230,exp}}$ can be straightforwardly measured by increasing the power $P_{230} \propto s_{230}$ of the 230 beam and acquiring the saturated count rate. Two scans, one at a detuning $\Delta_0 \approx 0$ (black data) and the other one at $\Delta_0 \approx -\Gamma_{230}/2$ (red data), as well as fitted saturation curves (solid lines) shown in Fig. 5.2.

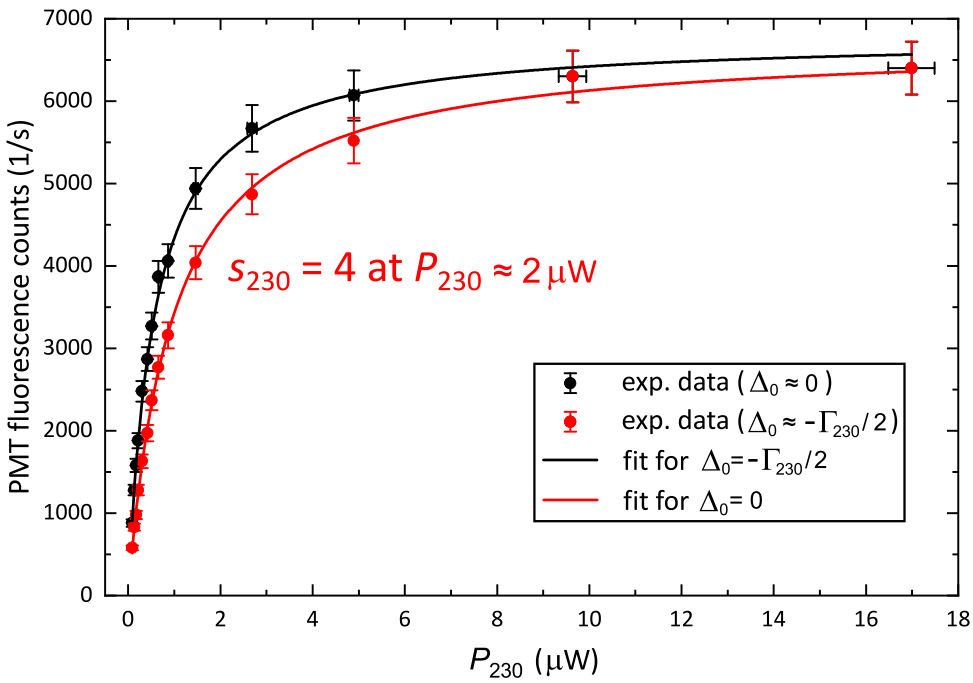

Figure 5.2 Saturation scans of the 230.6 nm indium detection transition. To find the maximum scattering rate $\Gamma_{\mathrm{sc,230,exp,max}}$ of one indium ion, the power P_{230} of the beam 230 is varied and the corresponding PMT count rates are measured. Two data sets are acquired for the detunings $\Delta_0 \approx 0$ (black data) and $\Delta_0 \approx -\Gamma_{230}/2$ (red data). Both sets are fitted using Eq. 5.66, from which two values for $\Gamma_{\mathrm{sc,230,exp,max}}$ are determined. Figure used with changes under permission of T. Nordmann.

[7] A thorough analysis of all these effects is presented by T. Nordmann et al. in [44].

Both data sets were fitted, also under the assumption of a vanishing 1st order Doppler shift, using the fit function

$$\Gamma_{\text{exp}}(P_{230}) = \Gamma_{\text{max,exp}} \frac{\frac{P_{230}}{P_{230,\text{sat}}}}{1 + \frac{P_{230}}{P_{230,\text{sat}}} + (\frac{2\Delta_0}{\Gamma_{230}})^2}. \tag{5.66}$$

Here $\Gamma_{\text{max,exp}}$ and $P_{230,\text{sat}}$ are free fit parameters, from which $\Gamma_{\text{sc,230,exp,max}}$ and the saturation power (with $P_{230}/P_{230,\text{sat}} = s_{230}$) can be determined. The resulting fits show a good agreement with the experimental data, which indicates that the assumption of a vanishing 1st order Doppler shift could be valid. Or to be conservative, that the axial mode temperatures $T_{\text{ax},\alpha}$ are on the order of $T_{\alpha,\text{max,In}}$. From both fits, the maximum experimental scattering rate $\Gamma_{\text{max,exp}}$ are determined to be $(6784 \pm 97)/\,\text{s}$ and $(6717 \pm 122)/\,\text{s}$ for the black and red fit respectively, while the saturation powers $P_{230,\text{sat}}$ yield $(0.564 \pm 0.015)\mu\text{W}$ and $(0.479 \pm 0.014)\mu\text{W}$ (uncertainties from fitting). Both saturation powers are on the order of $0.5\mu\text{W}$, such that a saturation of $s_{230} = 4$ is reached for $P_{230} = 2\,\mu\text{W}$, which was used during the indium detection in the spring clock campaign.
To determine the detection efficiency, the mean of both values is used, such that

$$\Gamma_{\text{sc,230,exp,max}} = \frac{6750 \pm 80}{\text{s}}. \tag{5.67}$$

Now, η_{det} can be calculated using Eq. 5.63 as well as Γ_{230}

$$\eta_{\text{det}} = \frac{\Gamma_{\text{sc,230,exp,max}}}{\frac{\Gamma_{230}}{2}} = \frac{6750/\text{s}}{2\pi \times 180\,\text{kHz}} \approx (6 \pm 0.07) \times 10^{-3}. \tag{5.68}$$

Finally, to verify that the experimentally observed scattering rate at $s_{230} = 4$ agrees with the theoretical value calculated in Eq. 5.61, line scans of the $\sigma^{\pm}$ Zeeman transitions of the 230 nm detection transition are analyzed. These line scans were acquired during the spring clock campaign and show an average count rate of $\Gamma_{\text{sc,230,exp}} \approx (4400 \pm 200)/\text{s}$ (after subtracting the background count rate) at the detuning $\Delta_{0,230} = -\Gamma_{230}/2$. The average count rate is determined by interpolating between two data points acquired close to the detuning $\Delta_{0,230}$ to estimate the count rate at $\Delta_{0,230}$. Due to the interpolation, the uncertainty is assumed to be $\approx \pm 5\,\%$. From this average count rate, the corresponding total scattering rate can be calculated using Eq. 5.62

$$\Gamma_{\text{sc,230,exp}} = \eta_{\text{det}} \Gamma_{\text{sc,230}} \tag{5.69}$$

$$\Leftrightarrow \Gamma_{\text{sc,230}} = \frac{\Gamma_{\text{sc,230,exp}}}{\eta_{\text{det}}} \tag{5.70}$$

$$\approx \frac{(740000 \pm 30000)}{\text{s}},$$

in good agreement with the theoretical scattering rate determined in Eq. 5.61. As a result, axial mode temperatures on the order of $T_{j\alpha,\text{max,In}}$ seem to be realistic. Therefore, the linearized model for the indium detection transition will be applied in the temperature analysis of the corresponding detection phase.

5.1.5 Calculation of geometric factors ξ

To take into account the angular dependence of the dipole emission, the geometric factors $\xi_{\text{Yb,rad1/2}}$ and $\xi_{\text{In,rad1/2}}$ radial plane as well as $\xi_{\text{Yb,ax}}$ and $\xi_{\text{In,ax}}$ for the axial direction are calculated. For the calculation, it is important to consider both dipole emission patterns for $\pi-$, and $\sigma-$ emission. When the emitted light is purely linearly polarized, i.e. for a closed Zeeman transition with $\Delta m_F = 0$, the angular distribution of the emitted photons is given by [25]

$$f_\pi(\theta, \phi) = \frac{3}{8\pi} \sin(\theta)^2, \tag{5.71}$$

where $\theta \in [0, \pi)$ is the azimuth angle with respect to the quantization axis given by the direction of the bias magnetic field $\mathbf{B}$ (which is parallel to the z), and $\phi \in [0, 2\pi)$ the polar angle. For a purely circularly polarized light, i.e. for as closed $|\Delta m_F|= 1$ transition as it is the case for the stretched state indium detection transition, the pattern is given by

$$f_\sigma(\theta, \phi) = \frac{3}{16\pi}(1 + \cos(\theta)^2). \tag{5.72}$$

As can be seen, there is no explicit dependence of ϕ, resulting in a rotational symmetry around the z-axis. Moreover, both distributions are normalized

$$\int_{S^2} f_\pi(\theta, \phi) d\Omega = \int_{S^2} f_\sigma(\theta, \phi) d\Omega = 1, \tag{5.73}$$

where S^2 is the 2-sphere and $d\Omega = \sin(\theta) d\phi d\theta$ the solid angle element. Therefore, $f_\pi(\theta, \phi)$ and $f_\sigma(\theta, \phi)$ represent probability distributions for the emission of a photon into the solid angle $d\phi d\theta$. Following [63], the geometric factors ξ can be calculated by the second moment of the respective coordinate with respect to the given emission pattern. Here the second moment is a measure of the directional spread of photons in the process of spontaneous emission. E.g. for the calculation of $\xi_{z,\sigma}$, the geometric factor for emission along the z-axis assuming a circular polarization of the emitted light field, the second moment can be calculated by

$$\xi_{z,\sigma} = \int_{S_2} z^2 f(\theta, \phi) d\Omega = \int_{S_2} \cos(\theta)^2 f(\theta, \phi) d\Omega, \tag{5.74}$$

where in the last step the cartesian z-coordinate was replaced with its representation in spherical coordinates using the basis

$$\mathbf{r} = \begin{pmatrix} x \\ y \\ z \end{pmatrix} = \begin{pmatrix} \sin(\theta)\cos(\phi) \\ \sin(\theta)\sin(\phi) \\ \cos(\theta) \end{pmatrix}. \tag{5.75}$$

At first, the geometric factors for the indium detection transition $\xi_{\mathrm{In,rad1/2}}$ and $\xi_{\mathrm{In,ax}}$ are calculated. To drive both stretched state transitions $^1\mathrm{S}_0 \rightarrow {}^3\mathrm{P}_1$, $|m_{F,g} = \pm 9/2\rangle \rightarrow |m_{F,e} = \pm 11/2\rangle$, the 230 beam is circularly polarized. Since the B field is pointing along the $z-$ axis, using $f_\sigma(\theta, \phi)$, $\xi_{\mathrm{In,ax}}$ is given by the second moment of the $z-$component

$$\begin{aligned} \xi_{\mathrm{In,ax}} &= \int_{S_2} z^2 f_\sigma(\theta, \phi) d\Omega & (5.76) \\ &= \frac{3}{16\pi} \int_0^\pi \int_0^{2\pi} \cos(\theta)^2 (1 + \cos(\theta)^2) \sin(\theta) d\phi d\theta & (5.77) \\ &= \frac{2}{5}. & (5.78) \end{aligned}$$

Moreover, due to the rotational symmetry of $f_\sigma(\theta, \phi)$, the second moment of x and y are equal. The symmetry also allows to choose the $x/y-$axes along the modes of the radial axes $\nu_{\mathrm{rad1/2}}$. Hence, $\xi_{\mathrm{In,rad1/2}}$ can be calculated via

$$\begin{aligned} \xi_{\mathrm{In,rad1}} &= \int_{S_2} x^2 f_\sigma(\theta, \phi) d\Omega & (5.79) \\ &= \frac{3}{8\pi} \int_0^\pi \int_0^{2\pi} (\sin(\theta)\cos(\phi))^2 (1 + \cos(\theta)^2) \sin(\theta) d\phi d\theta & (5.80) \\ &= \frac{3}{10} = \xi_{\mathrm{In,rad2}}. & (5.81) \end{aligned}$$

The calculation of $\xi_{\mathrm{Yb,rad1/2}}$ and $\xi_{\mathrm{Yb,ax}}$ is a bit more complicated since the the ground and excited state of the 370 nm $^2\mathrm{S}_{1/2} \rightarrow {}^2\mathrm{P}_{1/2}$ cooling transitions are both $J = 1/2$ states. Therefore, there

is no closed transition. After a transition from the ground to the excited state, the cooling ion is in one of the $|m_{F,e} = \pm 1/2\rangle$ substates. The ion can then decay into $|m_{F,g} = \pm 1/2\rangle$ or $|m_{F,g} = \mp 1/2\rangle$ under emission of linearly ($\Delta m_F = 0$) or circularly ($\Delta m_F = \mp 1$) polarized light. The fraction of light being emitted in each decay channel is given by the squared Clebsch-Gordan coefficients $c^2_{\mathrm{CG},0}$ and $c^2_{\mathrm{CG},\pm}$ of both Zeeman transitions. The respective radiation pattern are then weighted by $c^2_{\mathrm{CG},0}$ and $c^2_{\mathrm{CG},\pm}$ and summed up to arrive at the combined emission pattern for the 370 nm cooling transition

$$f_{370}(\theta,\phi) = c^2_{\mathrm{CG},0} f_\pi(\theta,\phi) + c^2_{\mathrm{CG},\pm} f_\sigma(\theta,\phi) \tag{5.82}$$

$$= \sqrt{\frac{1}{3}}^2 \frac{3}{8\pi}\sin(\theta)^2 + \sqrt{\frac{2}{3}}^2 \frac{3}{16\pi}(1+\cos(\theta)^2) \tag{5.83}$$

$$= \frac{1}{8\pi}(1 + \underbrace{\sin(\theta)^2 + \cos(\theta)^2}_{=1}) = \frac{1}{4\pi}. \tag{5.84}$$

The resulting emission pattern is independent of θ and ϕ and hence spherically symmetric. Using $f_{370}(\theta,\phi)$, $\xi_{\mathrm{Yb,rad1/2}}$ and $\xi_{\mathrm{Yb,ax}}$ can be calculated. By analogy with the indium geometric factors, $\xi_{\mathrm{Yb,ax}}$ is given by the second moment of z and $\xi_{\mathrm{Yb,rad1/2}}$ by the second moment of x and y respectively

$$\xi_{\mathrm{Yb,ax}} = \int_{S_2} z^2 f_{370}(\theta,\phi) d\Omega \tag{5.85}$$

$$= \frac{1}{4\pi}\int_0^\pi \int_0^{2\pi} \cos(\theta)^2 \times \sin(\theta) d\phi d\theta \tag{5.86}$$

$$= \frac{1}{4\pi}\frac{2}{3}2\pi = \frac{1}{3} \tag{5.87}$$

$$\xi_{\mathrm{Yb,rad1}} = \int_{S_2} y^2 f_{370}(\theta,\phi) d\Omega \tag{5.88}$$

$$= \int_{S_2} x^2 f_{370}(\theta,\phi) d\Omega \tag{5.89}$$

$$= \frac{1}{4\pi}\int_0^\pi \int_0^{2\pi} (\sin(\theta)\sin(\phi))^2 \times \sin(\theta) d\phi d\theta \tag{5.90}$$

$$= \frac{1}{4\pi}\frac{4\pi}{3} = \frac{1}{3} = \xi_{\mathrm{Yb,rad2}}. \tag{5.91}$$

5.2 Clock sequence temperature analysis

After the model for sympathetic mode cooling was applied to the experimental conditions in the indium clock setup, this section presents the results of a mode temperature analysis of the clock sequence used in the spring clock campaign. In 5.2.1, basic calculation settings for the analysis and used experimental parameters are discussed, followed by the analysis in 5.2.2. Finally, 5.2.3 briefly summarizes this section.

5.2.1 General calculation settings and used experimental parameters

In this subsection, the general calculation settings as well as experimental parameters used for the temperature analysis of the clock cycle are presented.
At first, a Python code is written which calculates the time dependence of the axial and radial mode temperatures $T_{\mathrm{ax},\alpha}(t)$ and $T_{\mathrm{rad1/2},\alpha}(t)$. As can be seen in Fig. 3.3, the saturation parameters s of all lasers are constant, except for the Doppler cooling phase where the saturation parameters $s_{\mathrm{H1/V}} \equiv s_{\mathrm{H1/V}}(t)$ of H1/V are ramped down linearly. The time dependence of the phases for constant s can therefore be described by the analytical solution given in Eq. 5.12.

Using the cooling and heating coefficients derived in subsection 5.1.2, for each temperature dependence (axial and radial), a Python class is written. Both classes use the saturation coefficients of all contributing beams s, the initial mode temperature $T_{\mathrm{ini},j\alpha}$, the sum of the squared eigenvector components $C_{\mathrm{ax},\alpha}$ and $C_{\mathrm{rad1/2},\alpha}$ of the ytterbium and indium ions as well as the time spent in the respective phase as inputs. Since the radial mode $T_{\mathrm{rad1/2},\alpha}(t)$ shows an explicit dependence on the angle θ, this input is added to the radial temperature class. To simulate the temperatures resulting from the saturation ramp in the cooling phase, two additional classes for the radial and axial modes are written. Here the solution for time dependent cooling and heating coefficients $c_{0/1,j\alpha}(t)$ given in Eq. 5.17 is used. The time dependence of saturation coefficients $s_{\mathrm{H1/V}}$ of H1/V in $c_{0/1,j\alpha}(t)$ is implemented by the ramp function

$$\mathrm{ramp}(t) = 1 - at, \tag{5.92}$$

such that $s_{\mathrm{H1/V}}(t) = s_{\mathrm{H1/V}} \times \mathrm{ramp}(t)$. Here $a = t_{\mathrm{ramp}}^{-1}$ is the saturation ramp slope and t_{ramp} the time in which the saturation is ramped down from the initial saturation $s_{\mathrm{H1/V}}$ to 0. To evaluate the integrals in Eq. 5.17, a simple Riemann sum is used, where the integrated time interval is split into n parts. To find a proper number of integration steps n and also to test the numerical integration, a dummy temperature dependence is calculated using both solutions in Eqs. 5.17 and 5.12 assuming time independent saturation coefficients s. Here $n = 5000$ results in a deviation of both solutions within $< 1\%$ by keeping reasonable calculation times of $\approx 1 - 2\,\mathrm{s}$. These four classes for time dependent and independent s and for the axial and radial mode temperatures are then used further to simulate single phases of the clock sequence as well as parts of the sequence by concatenating multiple phases.
The input parameters for the simulation are chosen to agree with the experimental conditions in the campaign. All the needed parameters related to the trapping confinement are gathered in Tab. 6 [49] while the parameters related to the sequence are shown in Fig. 3.3.

Table 6 Confinement related experimental parameters for the spring clock campaign [49].

parameter	value
configuration	Yb-Yb-In-Yb/Yb-In-Yb-Yb
ν_{rf}	22 MHz
$\nu_{\mathrm{ax,Yb}}$	275 kHz
$\nu_{\mathrm{rad1,Yb}}$	825 kHz
$\nu_{\mathrm{rad2,Yb}}$	802 kHz
θ	30°

As shown in [42], smaller ratios $\nu_{\mathrm{rad}}/\nu_{\mathrm{ax}}$ lead to smaller cooling times for a fixed target temperature. Therefore, $\nu_{\mathrm{rad1,Yb}} \approx \nu_{\mathrm{rad2,Yb}} = 825\,\mathrm{kHz}$ is assumed and hence the worse cooling efficiency. This also simplifies the analysis of the radial mode temperatures, because now the only dependence on the specific mode axis is given by their projection onto the cooling beam V. In case of the radial axis with ν_{rad1} the projection is described by θ, while, due to the orthogonality, the projection of the second axis is $\pi/2 - \theta$.
Now corresponding mode frequencies ν_α, coefficients $C_{\mathrm{ax},\alpha}$ and $C_{\mathrm{rad},\alpha}$ as well as Lamb-Dicke parameters $\eta_{\mathrm{In,rad},\alpha}$ of the radial modes for the indium ion (assuming $\cos(\theta) = 1$ in Eq. 2.47) are determined and shown in Tab. 7. The calculation is done using a Mathematica code written by J. Keller based on the theory presented in 2.4.3.

Table 7 Calculated coefficients C_α for the axial and radial modes assuming $\nu_{\mathrm{rad,Yb}} = 825\,\mathrm{MHz}$ and $\nu_{\mathrm{ax,Yb}} = 275\,\mathrm{MHz}$.

mode index α	1	2	3	4
$\nu_{\mathrm{rad},\alpha}$ (kHz)	657	757	790	1130
$C_{\mathrm{rad,Yb},\alpha}$	0.9839	0.9814	0.9907	0.0439
$C_{\mathrm{rad,In},\alpha}$	0.0161	0.0186	0.0093	0.9561
$\eta_{\mathrm{In,rad},\alpha}$	0.0276	-0.0277	-0.0191	-0.1617
$\nu_{\mathrm{ax},\alpha}$ (kHz)	287	480	687	943
$C_{\mathrm{ax,Yb},\alpha}$	0.8354	0.9717	0.8785	0.3144
$C_{\mathrm{ax,In},\alpha}$	0.1646	0.0283	0.1215	0.6856

As can be seen in Eq. 5.12, C_α scales the cooling coefficients $c_1 \propto C_\alpha$ and therefore the exponential decrease of the mode temperature $T_\alpha(t)$. Hence, C_α is a measure for the cooling efficiency of the respective species in the mode α. This becomes clear in Fig. 5.3, where the mode eigenvectors of the axial and radial modes for the trapping parameters in Tab. 6 are shown. Here the displacement of the ions (blue Yb^+ and pink In^+) from the equilibrium position is proportional to their respective eigenvector components $\beta'_{j\alpha,i}$.

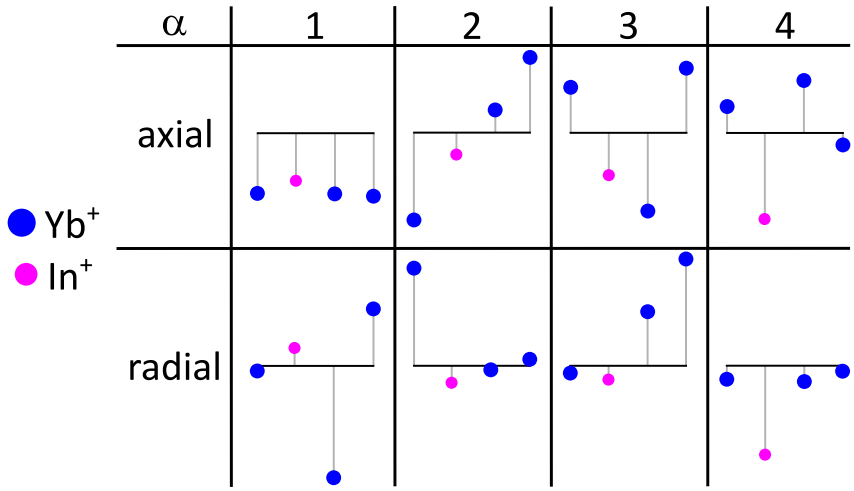

Figure 5.3 Radial and axial mode eigenvectors present during the spring clock campaign. For the trapping parameters used during the spring clock campaign (see Tab. 6), radial and axial mode eigenvectors are calculated. Blue and pink circles show ytterbium and indium ions. The corresponding mode frequencies, coefficients C_α as well as radial indium Lamb-Dicke parameters are shown in Tab. 7.

The larger the ytterbium eigenvector component, the larger the contribution of the each ion to the motion in the mode, and therefore its contribution to cooling. While the radial modes $\alpha = \{1, 2, 3\}$ show large eigenvector components for the ytterbium ions and just minor contributions for the indium ions, the situation is opposite for $\alpha = 4$. Here the motion is dominated by the indium ion. As a result, this is the mode with the smallest coefficient $C_{\mathrm{rad,Yb},\alpha}$ (see Tab. 7) and hence the worst cooled. A similar situation is given for the axial modes. In addition to the bad cooling efficiency, there is another interesting aspect motivating a thorough temperature analysis of the radial mode $\alpha = 4$. The corresponding large eigenvector component of the indium ion results in a large Lamb-Dicke factor $\eta_{\mathrm{In,rad},\alpha}$ (see Tab. 7 and Eq. 2.47). As presented in 2.6, radial modes with large indium Lamb-Dicke factors contribute most to thermal dephasing and hence to the temperature dependent loss of contrast. The temperature analysis is therefore done for the worst cooled radial and axial modes. The resulting temperatures T_α can be seen as an upper bound for the temperatures of all modes. In the following, the explicit dependence on α is dropped and all temperatures are calculated for $\alpha = 4$.
Before the clock cycle can be analyzed, another important assumption needs to be made. In

addition to the ion-light interaction as well as the mode structure, the initial temperature T_{ini} determines the mode temperature's time dependence. Here the results of a crystal melting point analysis done by L. Rüffert gives a helpful orientation [66]. The melting point $T_{\mathrm{melt}} \approx 18\,\mathrm{mK}$ can be understood as the maximum temperature above which the ions either start to change the configuration (change their position within the linear chain) or undergo a transition in an uncrystallized phase. Although the crystal is still cooled above T_{melt}, this case is not of interest for the temperature analysis since a change of configuration or a phase transition are detected in the clock sequence and trigger an invalidation of the current cycle (see 3.3). Therefore under the assumption that thermal energy is equally distributed to all modes in the beginning of each simulation, $T_{\mathrm{melt}} \approx 18\,\mathrm{mK}$ will be used as an upper bound for the initial mode temperatures T_{ini} for the axial and radial modes.

5.2.2 Clock sequence temperature analysis

As shown in section 3.3, the clock sequence consists of four branches accounting for situations which can occur during clock operation. Which branch is used depends on whether the crystal melted/changed its configuration between two cycles, or if the indium ion decayed back into the ground state after the previous clock interrogation. In principle, since only branch 1 is evaluated, its phases determine the temperature of the ions before the start of (and during) the clock interrogation. This assumption is only true, if reproducible temperatures are reached reached within one cycle of the sequence branch 1, independent of the foregoing used branch. The assumption is verified in 5.2.2.1, where the mode temperatures during the cooling phase are calculated for the worst case initial temperatures $T_{\mathrm{ini}} = T_{\mathrm{melt}}$. To obtain more realistic initial temperatures of the Doppler cooling phase and to analyze their impact on the mode temperature time dependence, in 5.2.2.2, the ytterbium and indium detection phases are simulated. 5.2.2.3 further analyzes the indium detection phase and its impact on the radial mode temperatures. In 5.2.2.4, the time dependence of the mode temperatures for the complete sequence branch 1 is determined. Here minimum initial mode temperatures $T_{\mathrm{opt}} \ll T_{\mathrm{melt}}$ are found which describe the case of optimal experimental conditions. These temperatures result solely from the phases in branch 1, neglecting possible disturbances such as heating by background gas collision. Lastly, in 5.2.2.5, the influence of experimental imperfections on the mode temperatures given by cooling laser frequency and intensity fluctuations are analyzed, followed by 5.2.2.6, where a first comparison of the determined radial temperatures with experimental data is done.

5.2.2.1 Analysis of the Doppler cooling phase for worst case initial temperatures T_{melt}

The Doppler cooling phase is simulated which consists of $t_{\mathrm{const}\,s} = 25\,\mathrm{ms}$ Doppler cooling at constant saturation $s_{\mathrm{H1/V}}$ for the beams H1/V (constant s phase) and afterwards a saturation ramp within $t_{\mathrm{ramp}} = 25\,\mathrm{ms}$ (ramped s phase) for the worst case mode temperature $T_{\mathrm{ini,ax}} = T_{\mathrm{ini,rad}} = T_{\mathrm{melt}}$. The resulting time dependencies are shown in Fig. 5.4. Here the mode temperatures are simulated for the trap axes orientation in the spring campaign shown by the yellow ($\theta = 30°$) and red ($\theta = 60°$) curves as well as the axial temperature (blue dashed line). Due to the assumption $\nu_{\mathrm{rad1}} = \nu_{\mathrm{rad2}}$, the mode temperatures of both trap axes can be calculated by adjusting the input parameter θ. Every pair of angles θ adding up to 90° describes a specific trap axes orientation. Hence, $\theta = 30°$ describes the modes along the radial axes with ν_{rad1} and with $\theta = 90° - 30° = 60°$ the temperatures of the orthogonal radial axis. In addition, radial temperatures for an equal projection of $\theta = 45°$ (green) on both radial axes as well as extreme cases $\theta = \{1°, 89°\}$ (dash-dotted, light blue and light green) are plotted. The time dependence of s_{V} is plotted as dark blue solid line, s_{H1} is not shown since there is a fixed ratio $s_{\mathrm{H1}}/s_{\mathrm{V}} \approx 1/3$. The location of the cooling phase within branch 1 is shown by the time line in the bottom. As

can be seen in Tab. 8, the final temperatures of the cooling phase are below 1 mK, except for the case of $\theta = 89°$ where the second principal axis is nearly orthogonal to V.

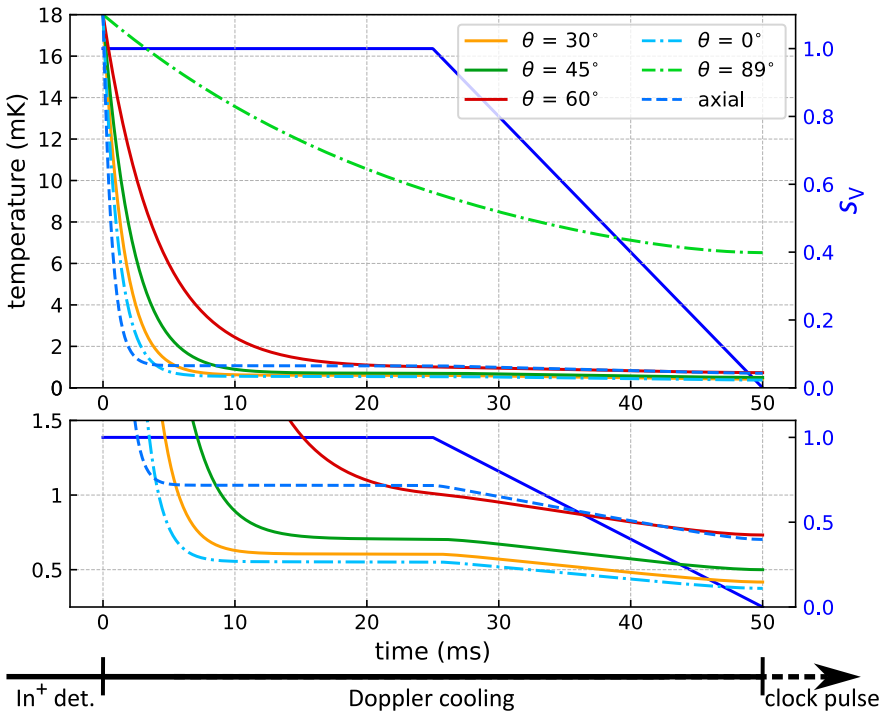

Figure 5.4 Time dependence of the axial and radial mode temperatures in the Doppler cooling phase assuming initial mode temperatures $T_{\text{ini}} = T_{\text{melt}} = 18\,\text{mk}$. The axial mode temperatures are shown as blue dashed line, the radial temperatures for different principal axes orientations θ as dash dotted and solid lines. The time dependence of the saturation coefficient s_{V} is shown as dark blue line. The cooling phase within the clock sequence branch 1 is shown by the time line in the bottom. Resulting end temperatures of the Doppler cooling phase T_{end} as well as selected temperature differences are shown in Tab. 8.

Table 8 Final temperatures T_{end} and selected temperature differences of the cooling phase assuming $T_{\text{ini}} = T_{\text{melt}}$ (see Fig. 5.4), all temperatures in mK.

mode	0°	30°	45°	60°	89°	axial
$T_{\text{end,const}\,s}$	0.55	0.61	0.71	1.01	9.43	1.07
$T_{\text{eq,const}\,s}$	0.55	0.61	0.71	0.97	4.13	1.07
$T_{\text{end,const}\,s} - T_{\text{eq,const}\,s}$	0	0	0	0.04	5.30	0
T_{end}	0.37	0.42	0.50	0.73	6.52	0.70
$T_{\text{end,const}\,s} - T_{\text{end}}$	0.18	0.19	0.21	0.28	2.91	0.37

Here a clear trend of increasing end temperatures T_{end} for increasing angles θ can be observed. In addition, the increase of T_{end} for large angles θ is overproportional compared to the decrease for small projections. Both effects are a result of a decreasing contribution of V for increasing values of θ. This can be explained by the dependence $k^2_{\text{V,rad}} \propto \cos(\theta)^2$ (Eq. 5.24) of V's contribution to the radial cooling coefficient $c_{1,\text{rad},370}$ (Eq. 5.40), while its contribution to the heating coefficient $c_{0,\text{rad},370}$ (Eq. 5.34) via spontaneous emission is independent of θ. Therefore, $\theta = 45$ yields the best trade-off regarding T_{end} for the modes of both radial axes. Besides the influence of θ on the radial end temperatures, a clear decrease of the cooling rate (or efficiency) can be observed for a decreasing V projection. While for $\theta = 0°$ the end temperature of the constant s phase $T_{\text{end,const}\,s}$ is equal to the corresponding equilibrium temperature $T_{\text{eq,const}\,s}$ within

$t \approx 9\,\mathrm{ms}$, for the worst projection $\theta = 89°$, an equilibrium is not reached for the full constant s time $t_{\mathrm{const\,s}} = 25\,\mathrm{ms}$ (see Tab. 8). For the projections of $\theta = \{30°, 60°\}$ used in the clock campaign as well as for $\theta = 45$, $T_{\mathrm{end,const}\,s} \approx T_{\mathrm{eq,const}\,s}$.
Regarding the axial modes, the cooling dynamics are faster compared to the radial modes. The high cooling efficiency is a result of a good projection of H1 ($\phi = 23°$) onto the axial modes and the coefficient $C_{\mathrm{ax,Yb}} \approx 0.31$, which is roughly eight times larger than the radial coefficient $C_{\mathrm{rad,Yb}} \approx 0.04$. On the other hand, the axial equilibrium temperature $T_{\mathrm{eq,const}\,s} = 1.07\,\mathrm{mk}$ is higher than the corresponding radial temperatures for $\theta \leq 60°$. This is a consequence of the orthogonality of the axial modes and V. Therefore, V does not contribute to the cooling coefficient $c_{1,\mathrm{ax},370}$ but to the heating coefficient $c_{0,\mathrm{ax},370}$ (see Eqs. 5.43 and 5.50) which leads to an increased equilibrium temperature $T_{\mathrm{eq}} \propto c_0$ (see Eq. 5.14).
Also the influence of the saturation ramp can be observed in Fig. 5.4. Within the ramped s phase ($t_{\mathrm{const}\,s} < t \leq 50\,\mathrm{ms}$), all investigated mode temperatures are further decreased by $\approx 30\%$ compared to the end temperature $T_{\mathrm{end,const}\,s}$ of the constant s phase (see Tab. 8). This temperature decrease is only possible due to the time dependent decrease of the saturation which results in a continuous decreases of the equilibrium temperature. Without the saturation ramp, i.e. keeping $s_{\mathrm{H1/V}}$ constant, the additional 25 ms of cooling time would not further decrease the temperature of all modes except for the extreme case of $\theta = 89°$. Note that an equal projection $\theta = 45°$ of both radial axes onto V might also be advantageous regarding a decrease of $t_{\mathrm{const}\,s}$. For this trap axes orientation, the radial modes reach equilibrium after $t \approx 15\,\mathrm{ms}$ such that the remaining 10 ms spent at constant saturation has no influence on the respective temperature $T_{\mathrm{end,const}\,s}$. This fact will be subject of the optimization of the clock sequence presented in section 5.3.
All axial modes as well as radial modes for $\theta \leq 60°$ reach (or are close to) equilibrium in the constant s phase assuming the worst case initial temperature $T_{\mathrm{ini}} = T_{\mathrm{melt}}$. Therefore, final temperatures of the ramped s phase and hence the end temperatures of the whole cooling phase T_{end} are reproducible within one clock cycle and hence robust against the worst case initial temperatures. In addition, within the validity of the model one can conclude that the indium ion's temperature during the clock interrogation is completely independent of chosen branches in the previous cycles such as reordering or rescue events in the sequence branches 3 or 4. Therefore, the analysis will be carried out in the following for the phases of branch 1. Note that the analysis of the extreme cases $\theta = 0°, 89°$ will be neglected in the following, as they are not relevant for the experiment due to the bad cooling efficiency of the modes for $\theta \approx 90°$. Since the orientation $\theta = 45°$ showed interesting properties regarding the cooling efficiency and resulting end temperatures, its analysis is continued.

5.2.2.2 Analysis of the mode temperatures during the In^+ and Yb^+ detection phases

So far, the end temperatures of the Doppler cooling phase were calculated for the worst case initial temperature $T_{\mathrm{ini}} = T_{\mathrm{melt}}$. Next, the influence of the Yb^+ and In^+ detection phases on the initial temperatures of the Doppler cooling phase are analyzed. As presented in 3.3, the ytterbium detection is used to detect whether the crystal melted or changed its configuration in the previous cycle. If such an event is detected, rescue or reordering attempts are started and the indium ion is not probed. The ytterbium detection therefore acts as a temperature filtering phase for temperatures $T > T_{\mathrm{melt}}$. For the simulation of both detection phases, the initial temperature of the ytterbium detection is chosen to be $T_{\mathrm{ini}} = T_{\mathrm{melt}}$, as it is the highest accepted temperature for branch 1 in the clock sequence. In Fig. 5.5, the time dependencies of the radial mode temperatures are plotted for $\theta = \{30°, 60°, 45°\}$ as well as the temperature of the axial modes. Note that the indium optical pumping phase is neglected, since its duration $t_{\mathrm{pump}} = 1\,\mathrm{ms}$ is negligible compared to $t_{\mathrm{In^+det}} = 20\,\mathrm{ms}$. In addition, due to the frequency ramp, it is not possible to make a proper statement on the 230 nm scattering rate.

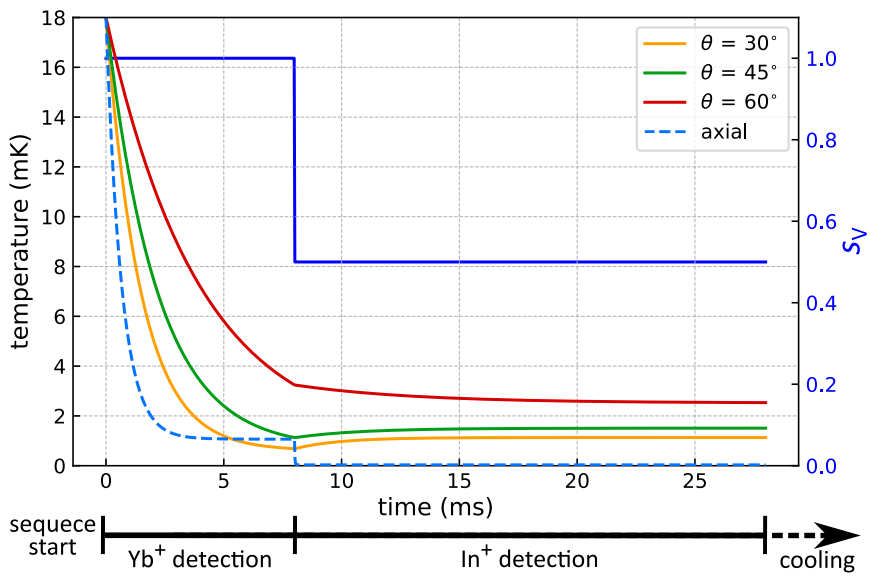

Figure 5.5 Time dependence of the axial and radial mode temperatures within the ytterbium and indium detection phases assuming an initial temperature $T_{\mathrm{ini}} = T_{\mathrm{melt}}$. The final temperatures of both phases are shown in Tab. 9.

Table 9 Final temperatures of the ytterbium and indium detection phases assuming an initial temperature of the ytterbium detection of $T_{\mathrm{ini}} = T_{\mathrm{melt}}$ (see Fig. 5.5), temperatures in mK.

mode	30°	45°	60°	axial
$T_{\mathrm{end,Yb^+det}}$	0.69	1.17	3.36	1.07
$T_{\mathrm{end,In^+det}}$	1.15	1.53	2.58	0.03

The corresponding end temperatures $T_{\mathrm{end,Yb^+det}}$ and $T_{\mathrm{end,In^+det}}$ of the ytterbium and indium detection phases are shown in Tab. 9. It can be seen that the ytterbium detection significantly reduces the initial temperatures and hence contributes to cooling. Although the detection is just $t_{\mathrm{Yb^+det}} = 8\,\mathrm{ms}$ long, the end temperatures $T_{\mathrm{end,Yb^+det}} \approx T_{\mathrm{eq,const}\,s}$ for the axial modes as well as for the radial modes with $\theta = 30°$ (compare with Tab. 8). This can be explained by the saturation coefficients $s_{\mathrm{V/H1}}$ used in the ytterbium detection which agree with the saturations during the constant s phase of Doppler cooling. The ytterbium detection can therefore be seen as an additional cooling phase at constant saturation. For the indium detection, the temperature dynamics of the radial and axial modes differ. While for $\theta = 60°$ the temperature is further decreased until the end of the indium detection, for $\theta = \{30°, 45°\}$ the opposite can be observed. For these two orientations, the mode temperatures are increased until an equilibrium $T_{\mathrm{eq,In^+det}}$ is reached which agrees with the corresponding temperature $T_{\mathrm{end,In^+det}} \approx T_{\mathrm{eq,In^+det}}$. The observed radial temperature dynamic is a consequence of a decreased 370 nm saturation ($s_{\mathrm{V}} = 0.5$ and $s_{\mathrm{V}} \approx 0.2$) in the presence of indium fluorescence on the 230 nm transition at $s_{230} = 4$. Since the 230 beam is parallel to the trap axis, the indium fluorescence results in heating of the radial modes via the heating coefficient $c_{0,\mathrm{rad},230}$ (see Eq. 5.35) while there is no contribution to the radial cooling coefficient $c_{1,\mathrm{rad}}$ (Eq. 5.40). The increased heating coefficient as well as decreased cooling coefficient (due to decreased $s_{\mathrm{V/H1}}$) then leads to an increased equilibrium temperature $T_{\mathrm{eq,In^+det}}$. Since $T_{\mathrm{end,Yb^+det}} > T_{\mathrm{eq,In^+det}}$ for $\theta = 60°$ the corresponding modes are further cooled, while for $\theta = \{30°, 45°\}$ the modes are heated ($T_{\mathrm{end,In^+det}} < T_{\mathrm{eq,In^+det}}$).
For the axial modes, a steep temperature drop to 0.03 mK can be observed, which is about two orders of magnitude lower than the axial end temperatures of the Doppler cooling phase (see Tab. 8). This is a consequence of the narrow 230 nm transition ($\Gamma_{230} = 2\pi \times 360\,\mathrm{kHz}$ compared to

$\Gamma_{370} = 2\pi \times 19.6\,\mathrm{MHz}$) which results in a reduced equilibrium temperatures compared to cooling solely on the 370 nm transition. Moreover, the indium ion has a large eigenvector component in the investigated axial mode $\alpha = 4$ (see Fig. 5.3) which results in a high coefficient $C_{\mathrm{ax,In},\alpha} \approx 0.686$ and fast cooling dynamics. Here one can say that the axial temperature dynamic is dominated by direct cooling on the indium detection transition.
At this point, it is important to mention that the time dependence as well as the final temperature on the radial modes can only serve as an orientation of dynamics resulting from the 230 nm fluorescence. As concluded in section 5.1.4, the used linearization of the indium scattering rate is valid only for temperatures $T_{\alpha,\mathrm{max,In}} < 0.012\,\mathrm{mK}$. Since the calculated axial temperature is above this limit, the model loses validity. The only statement which can be made is that the axial mode temperatures are likely close to an equilibrium, since the experimentally observed indium scattering rates agree with the maximum theoretical scattering rates. This equilibrium temperature could be on the order of $T = 100\,\mu\mathrm{K}$ as observed experimentally by E. Peik in [67]. Moreover, since the axial mode frequencies $\nu_{\mathrm{ax},\alpha}$ shown in Tab. 7 are on the order of the linewidth $\Gamma_{230}/(2\pi)$ of the indium detection transition, a rate equation model based on Doppler cooling theory is not a proper description anymore. Here the temperature dynamics is in an intermediate regime between Doppler and of resolved sideband cooling (see e.g. [31]), the simulation of which is beyond the scope of this analysis.

5.2.2.3 Analysis of radial heating due to In^+ detection

Since the indium detection induces heating of the radial modes, the corresponding heating coefficient $c_{0,\mathrm{rad},230}$ is analyzed. Here the maximum scattering rate for $s_{230} = 4$ is assumed, because it agrees with experimental observations (see section 5.1.4). To see the pure effect of radial heating due to the indium fluorescence, vanishing saturation coefficients $s_{\mathrm{V/H1}}$ are assumed ($\approx 10^{-6}$ in the simulation) by keeping the fixed ratio $s_{\mathrm{H1}}/s_{\mathrm{V}}$. Using the determined end temperatures $T_{\mathrm{end,Yb^+det}}$ as initial temperatures, the time dependence of the radial temperatures is shown in Fig. 5.6.

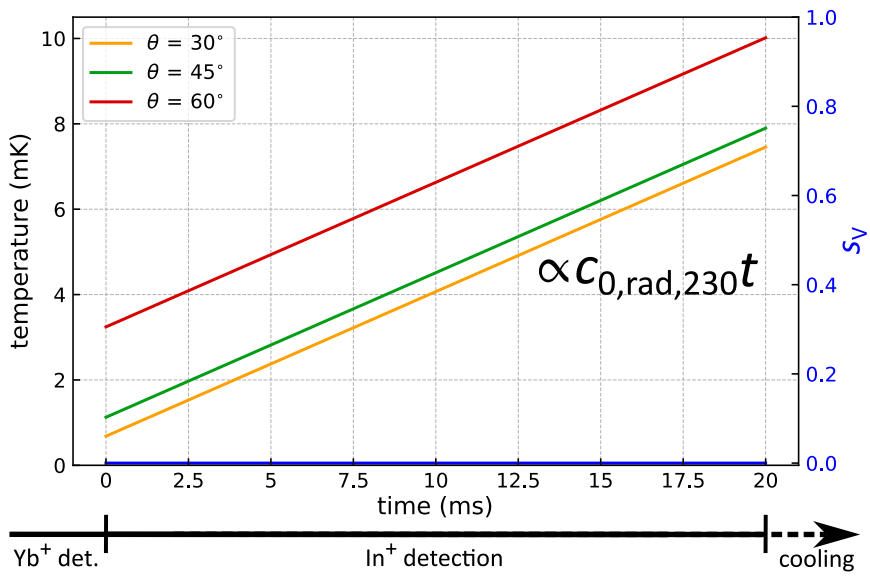

Figure 5.6 Time dependence of the radial mode temperatures during the indium detection phase for vanishing saturations $s_{\mathrm{V/H1}}$. Without the presence of the ytterbium cooling beams V and H1, the radial modes are heated by the indium fluorescence.

Here a linear increase of the radial temperatures as a function of time can be observed, while the slope (or radial heating rate) is given by $\approx 0.34\,\mathrm{mK/ms}$. The linearity is the result of a

constant heating rate due to the indium fluorescence at a constant scattering rate $\Gamma_{\mathrm{sc},230}(s_{230} = 4)$ (see Eq. 5.31). The slope corresponds to the radial heating coefficient $c_{0,\mathrm{rad},230}$, as can be seen from the general solution of $T_\alpha(t)$ for time independent coefficients $c_{0,1}$ (Eq. 5.12). In the limit of $s_{\mathrm{V/H1}} \to 0$, $c_{1,\mathrm{rad}} \to 0$. Now, the exponential function in Eq. 5.12 can be expanded to 1st order in $c_{1,\mathrm{rad}}$ such that

$$T_{\mathrm{rad}}(t) = \left[T_{\mathrm{ini}} + \frac{c_{0,\mathrm{rad}}}{c_{1,\mathrm{rad}}}\right] e^{c_{1,\mathrm{rad}}t} - \frac{c_{0,\mathrm{rad}}}{c_{1,\mathrm{rad}}} \tag{5.93}$$

$$\overset{c_{1,\mathrm{rad}}\to 0}{\approx} \left[T_{\mathrm{ini}} + \frac{c_{0,\mathrm{rad}}}{c_{1,\mathrm{rad}}}\right] (1 + c_{1,\mathrm{rad}}t) - \frac{c_{0,\mathrm{rad}}}{c_{1,\mathrm{rad}}} \tag{5.94}$$

$$= T_{\mathrm{ini}}(1 + c_{1,\mathrm{rad}}t) + c_{0,\mathrm{rad}}t \overset{s_{\mathrm{V/H1}}\to 0}{\approx} T_{\mathrm{ini}} + c_{0,\mathrm{rad},230}t. \tag{5.95}$$

Therefore, the heating rate is given by $c_{0,\mathrm{rad},230} \approx 0.34\,\mathrm{mK/ms}$ which agrees with the numerical value of this coefficient in the simulation. Here it can be concluded, that the indium detection contributes significantly to heating of the radial modes. To compensate for radial heating during the indium detection, the saturation coefficients $s_{\mathrm{V/H1}}$ could be increased. Such an optimization is subject of the clock sequence optimization in 5.3.

5.2.2.4 Mode temperature simulation of the complete sequence branch 1

After the simulation of the ytterbium and indium detection yielded end temperatures $T_{\mathrm{end,In^+det}}$ and hence initial temperatures of the cooling phase $T_{\mathrm{ini}} \leq 2.5\,\mathrm{mK} \ll T_{\mathrm{melt}}$ (Tab. 9), the complete branch 1 is simulated. This simulation aims for the initial temperatures T_{opt} and resulting end temperatures of the cooling phase under optimal experimental conditions without any external influences. Here external influences are e.g. collisions with background gas molecules which could lead to temperatures on the order of T_{melt} and hence the use of sequence branches 3 or 4. The simulation is split into two parts. At first, T_{opt} are determined in a simulation of the whole sequence branch 1. In a second simulation, the resulting end temperatures of the Doppler cooling phase for $T_{\mathrm{ini}} = T_{\mathrm{opt}}$ are calculated.
The end of the clock interrogation is chosen to be the starting point of the first simulation. Due to a vanishing external heating rate, it is assumed that the mode temperatures are constant during the 150 ms clock pulse. The initial temperatures of the simulation are hence the end temperatures of the Doppler cooling phase given in Tab. 8. As can be seen in Fig. 3.3, the following phases in branch 1 are an indium detection and, after the restart of the sequence, an ytterbium detection followed by another indium detection. The simulation of all three phases is shown in Fig. 5.7

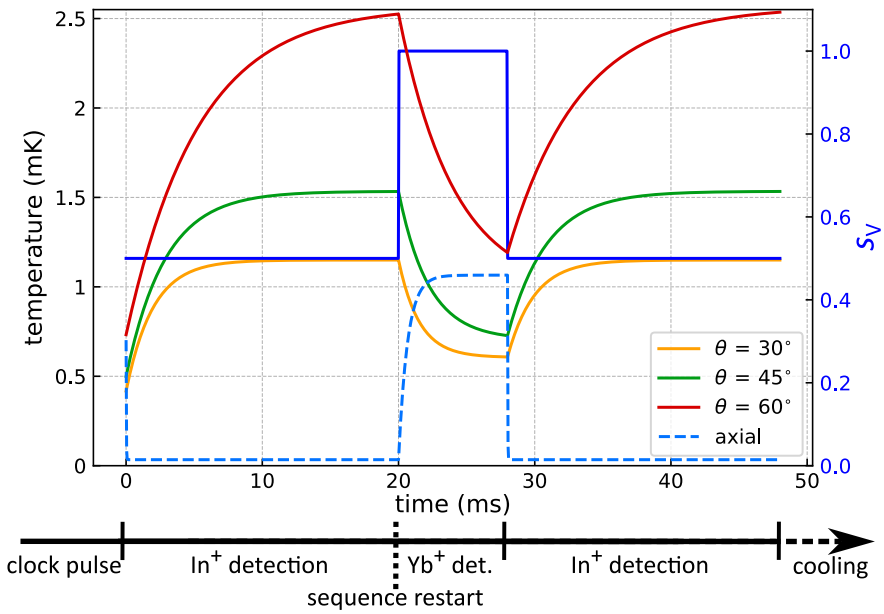

Figure 5.7 Simulation of the axial and radial mode temperatures in sequence branch 1 excluding the Doppler cooling phase. Starting point of the simulation is the end of clock pulse. Since the external heating rate is neglected, the mode temperatures remain unchanged during the clock interrogation. The end temperatures of this phase are therefore assumed to be the end temperatures of the Doppler cooling phase given in Tab. 8. These temperatures are used as initial temperatures of the simulation starting with the first indium detection ($t = 0$). The end temperatures of this phase $T_{\text{end,In+det}}$, the following ytterbium detection $T_{\text{end,Yb+det}}$ and the second indium detection T_{end} are given in Tab. 10.

Table 10 Final mode temperatures for the simulation of the phases in clock sequence branch 1 (see Fig. 5.7), temperatures in mK.

mode	30°	45°	60°	axial
$T_{\text{end,In+det}}$	1.15	1.53	2.53	0.03
$T_{\text{end,Yb+det}}$	0.61	0.73	1.19	1.07
$T_{\text{end}} =: T_{\text{opt}}$	1.15	1.53	2.54	0.03

As can be seen, under optimal experimental conditions, the axial and radial mode temperatures are $\leq 2.5\,\text{mK}$ throughout the whole sequence branch 1. In addition, an opposing temperature behavior for the radial and axial modes can be observed. While the radial modes are heated during the indium detection phases and cooled during the ytterbium detection, the situation is opposite for the axial modes. The final temperatures after the second indium detection T_{end} and hence optimal initial temperatures of the Doppler cooling phase, denoted as T_{opt} in the following, as well as end temperatures of each simulated phase are shown in Tab. 10. By comparison of T_{opt} with the initial temperatures determined in Fig. 5.5 (see $T_{\text{end,In+det}}$ in Tab. 9), one can see that the temperature differences are negligible. This is the case, although the initial temperature of the ytterbium detection was assumed to be T_{melt}. Therefore, it can be concluded, that the ytterbium and indium detection phases are long enough to reach reproducible temperatures within branch 1 already before the the Doppler cooling phase starts.
Since T_{opt} are determined, the Doppler cooling phase is again simulated to determine the mode temperatures present during clock interrogation under optimal experimental conditions. The simulation and resulting temperatures are shown in Fig. 5.8 and Tab. 11.

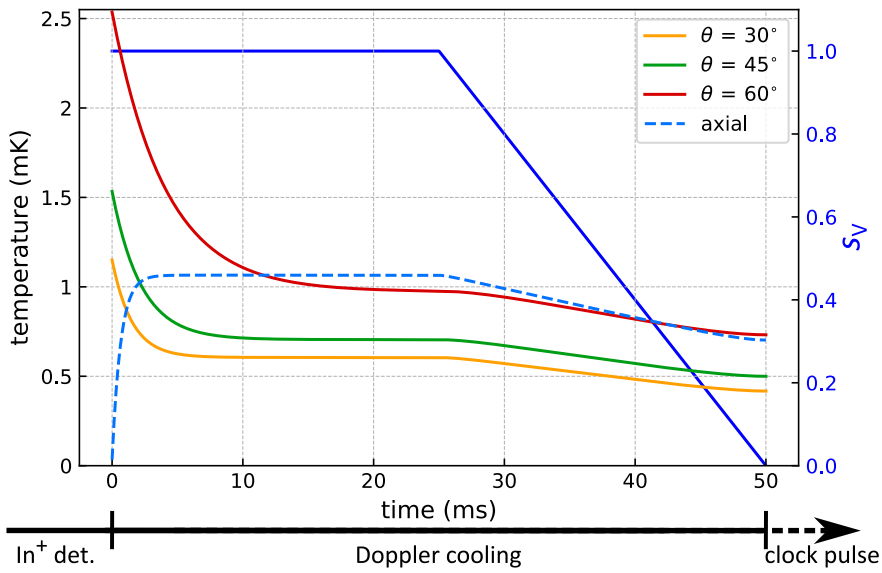

Figure 5.8 Simulation of the mode temperatures in the Doppler cooling phase assuming initial temperatures $T_{\text{ini}} = T_{\text{opt}}$. For optimal initial mode temperatures as shown in Tab. 10, all modes reach an equilibrium already within $t_{\text{const } s} \approx 15\,\text{ms}$. The end temperatures of Doppler cooling phase agree with the temperatures calculated for the worst case initial temperatures $T_{\text{ini}} = T_{\text{melt}}$ of the simulation shown in Fig. 5.4 (see also Tab. 8). The calculated mode temperatures of the constant s and ramped s phases as well as selected temperature differences are shown in Tab. 11

Table 11 Final temperatures T_{end} of the constant s and ramped s phases in the Doppler cooling phase assuming $T_{\text{ini}} = T_{\text{opt}}$ (see Fig. 5.8), temperatures in mK.

mode	30°	45°	60°	axial
$T_{\text{end,const } s}$	0.61	0.71	0.98	1.07
$T_{\text{eq,const } s}$	0.61	0.71	0.97	1.08
$T_{\text{end,const } s} - T_{\text{eq,const } s}$	0	0	0	0
T_{end}	0.42	0.50	0.73	0.70
$T_{\text{end,const } s} - T_{\text{end}}$	0.19	0.21	0.25	0.37

By comparing the temperatures in Tab. 11 with the temperatures determined for the same phase but with $T_{\text{ini}} = T_{\text{melt}}$ (see Tab. 8), one can see that the end temperatures of both phases (constant s and saturation ramp) agree with each other. Interestingly, the axial mode temperatures are $\leq T_{\text{eq,const } s}$ throughout the whole constant s phase. This shows that the Doppler cooling phase is rather a "Doppler heating" phase for the axial modes. After $t \approx 15\,\text{ms}$ cooling at constant s, there is no significant temperature change for all considered modes. This indicates, in case of $T_{\text{ini}} = T_{\text{opt}}$, that the constant s phase could reduced by $\approx 10\,\text{ms}$ without affecting the end temperatures.

5.2.2.5 Influence of cooling laser frequency and intensity fluctuations

Until now, all the simulations were done for fixed detunings $\Delta_{0,370}$ and $\Delta_{0,230}$ as well as fixed saturation coefficients $s_{\text{V/H1}}$ and s_{230}. Under real experimental conditions, the laser frequencies as well as powers (and hence saturation coefficients) fluctuate over time. To include such experimental imperfections in the temperature analysis of the cooling phase, frequency and intensity fluctuations of the 370 nm laser are analyzed in the following.
To take into account the influence of frequency fluctuations on the cooling phase, the 370 nm

laser is stabilized to the fixed detuning $\Delta_{0,370}$ relative to resonance frequency using a wavemeter lock. Here the resonance is determined from a line scan of the 370 nm transition. While locked, frequency data is logged over several hours to acquire a histogram. Afterwards, the data is fitted using a Gaussian normal distribution. The fit results in a standard deviation of $\sigma_f \approx 1.338\,\mathrm{MHz}$, the mean value is assumed to be 0, due to calibration of the frequency lock via a line scan. To investigate the impact of the frequency distribution on the Doppler cooling phase, final temperatures of the radial modes for $\theta = \{30°, 45°, 60°\}$ and the axial modes are calculated for different detunings Δ_f within the distribution, such that $\Delta_{0,370} \rightarrow \Delta_{0,370} + \Delta_f =: \Delta_{f\,\mathrm{fluct}}$. The simulation is done for the two discussed cases $T_{\mathrm{ini}} = T_{\mathrm{opt}}$ and $T_{\mathrm{ini}} = T_{\mathrm{melt}}$ and shown in Fig. 5.9.

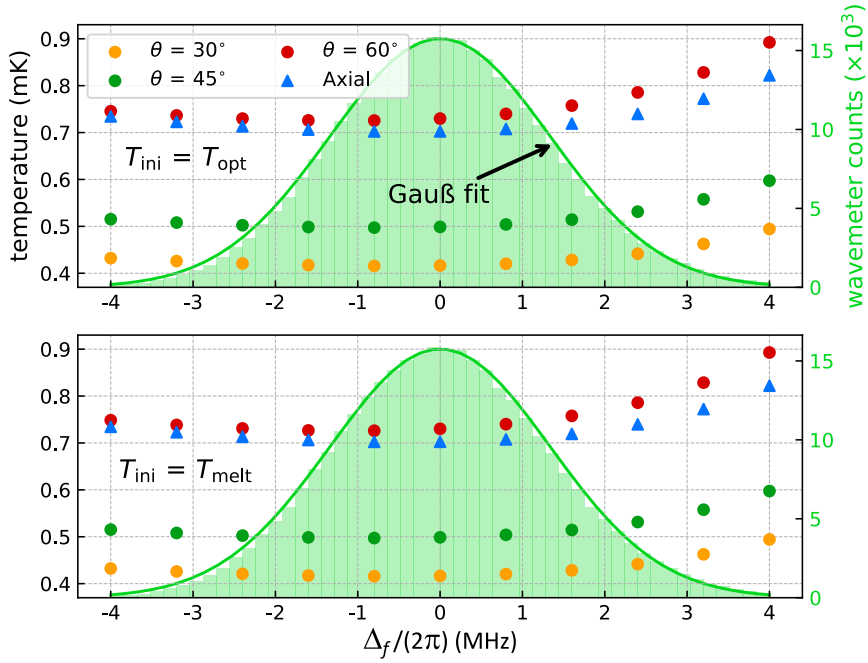

Figure 5.9 End temperatures of the Doppler cooling phase in the presence of frequency fluctuations. Wavemeter lock data is evaluated to investigate the influence of frequency fluctuations on the end temperatures of the Doppler cooling phase. The data is plotted as a histogram (light green) and fitted using a Gaussian distribution. The fit (solid green line) yields a standard deviation of $\sigma_f \approx 1.338\,\mathrm{MHz}$, the mean value $\mu_f \approx \Delta_{0,370}$ is set to 0. For detunings Δ_f within the distribution, radial and axial end temperatures are calculated assuming $T_{\mathrm{ini}} = T_{\mathrm{opt}}$ (top) and $T_{\mathrm{ini}} = T_{\mathrm{melt}}$ (bottom).

It can be observed that the end temperature of all modes are increasing for large detunings $|\Delta_f|$, the temperature increase is larger for $\Delta_f > 0$ than for $\Delta_f < 0$. Since for positive Δ_f, $|\Delta_{f\,\mathrm{fluct}}| < |\Delta_{0,370}|$, the friction coefficient ρ (Eq. 5.5) in the cooling coefficient c_1 is decreased, while the scattering rate $\Gamma_{\mathrm{sc},370}$ is increased. For negative Δ_f, $|\Delta_{f\,\mathrm{fluct}}| > |\Delta_{0,370}|$ which results in an increased friction coefficient ρ but a decreased scattering rate. These effects result in increased equilibrium temperatures. The minimum end temperatures are calculated for $\Delta_f \propto -2\mathrm{MHz}$, not for a vanishing Δ_f, which is a result of the saturation broadened linewidth [22] of the cooling transition due to the total saturation coefficient $s_{\mathrm{eff}} = s_{\mathrm{V}} + s_{\mathrm{H1}}$. Regarding the influence of both assumed initial temperatures $T_{\mathrm{ini}} = T_{\mathrm{opt}}$ and $T_{\mathrm{ini}} = T_{\mathrm{melt}}$, there are no significant differences in the end temperatures. For a quantitative analysis, the mean mode temperatures $\langle T_{\mathrm{end},f\,\mathrm{fluct},T_{\mathrm{opt}}} \rangle$ and $\langle T_{\mathrm{end},f\,\mathrm{fluct},T_{\mathrm{melt}}} \rangle$ are calculated for both assumed initial temperatures using the fitted distribution. In addition, the mean mode temperatures for frequency fluctuations are determined under the assumption of a twice as broad frequency distribution ($\sigma = 2\sigma_f$). For the broader distribution, the mode temperatures are reevaluated for $\Delta_f/(2\pi) \in [-8, +8]\,\mathrm{MHz}$. This

calculation is done to investigate the impact of less ideal locking conditions which could lead to a broadening of the distribution. The resulting mean temperatures are shown in Tab. 12. In addition, the end temperatures calculated in Fig. 5.8 for optimal experimental conditions are given as reference temperatures $T_{\mathrm{end,ref}}$.

Table 12 Mean final temperatures $\langle T_{\mathrm{end}} \rangle$ of the cooling phase assuming $T_{\mathrm{ini}} = T_{\mathrm{opt}}$ and $T_{\mathrm{ini}} = T_{\mathrm{melt}}$ in the presence of frequency fluctuations Δ_f (see Fig. 5.9), temperatures in mK.

mode	30°	45°	60°	axial
$T_{\mathrm{end,ref}}$	0.42	0.50	0.73	0.70
$\langle T_{\mathrm{end},f\,\mathrm{fluct},T_{\mathrm{opt}}} \rangle$	0.42	0.51	0.74	0.71
$\langle T_{\mathrm{end},f\,\mathrm{fluct},T_{\mathrm{melt}}} \rangle$	0.42	0.51	0.74	0.71
$\langle T_{\mathrm{end},f\,\mathrm{fluct},2\sigma,T_{\mathrm{opt}}} \rangle$	0.44	0.53	0.78	0.74
$\langle T_{\mathrm{end},f\,\mathrm{fluct},2\sigma,T_{\mathrm{melt}}} \rangle$	0.44	0.53	0.78	0.74

Compared to the reference temperatures, the calculated mean temperatures are equal in case of a distribution with $\sigma = \sigma_f$ and $\approx 5\%$ higher for the worse case of $\sigma = 2\sigma_f$, while the calculated mean temperatures are the same for both assumed initial temperatures. This shows that the cooling phase is long enough to cover a large range of initial temperatures. In addition, due to the small deviations within a few percent, the presence of frequency fluctuations has no significant influence on the end temperatures of the cooling phase.
To investigate the influence of intensity-, and hence saturation fluctuations, the intensity I_{V} of the Beam V is stabilized to the saturation intensity $I_{\mathrm{sat,V}}$ (corresponding to the desired saturation $s_{\mathrm{V}} = 1$) and logged over several hours. The data is then normalized by $I_{\mathrm{sat,V}}$ to acquire a histogram of the s_{V} fluctuations. Here it is sufficient to log the saturation in V, since s_{V} and s_{H1} have a fixed ratio $s_{\mathrm{H1}}/s_{\mathrm{V}} \approx 0.3$. As for the intensity fluctuations, the histogram is fitted with a Gaussian distribution, where a standard deviation $\sigma_s \approx 0.02$ and a mean value $\mu_s = 0.975$ is obtained. Again, for saturation values s_{V} within the distribution, final mode temperatures of the Doppler cooling phase for $T_{\mathrm{ini}} = T_{\mathrm{opt}}$ and $T_{\mathrm{ini}} = T_{\mathrm{melt}}$ are calculated. Using these temperatures, the mean temperatures $\langle T_{\mathrm{end},s\,\mathrm{fluct},T_{\mathrm{opt}}} \rangle$ and $\langle T_{\mathrm{end},s\,\mathrm{fluct},T_{\mathrm{melt}}} \rangle$ are determined using the fitted distribution function. The results are shown in Fig. 5.10 and Tab. 13.

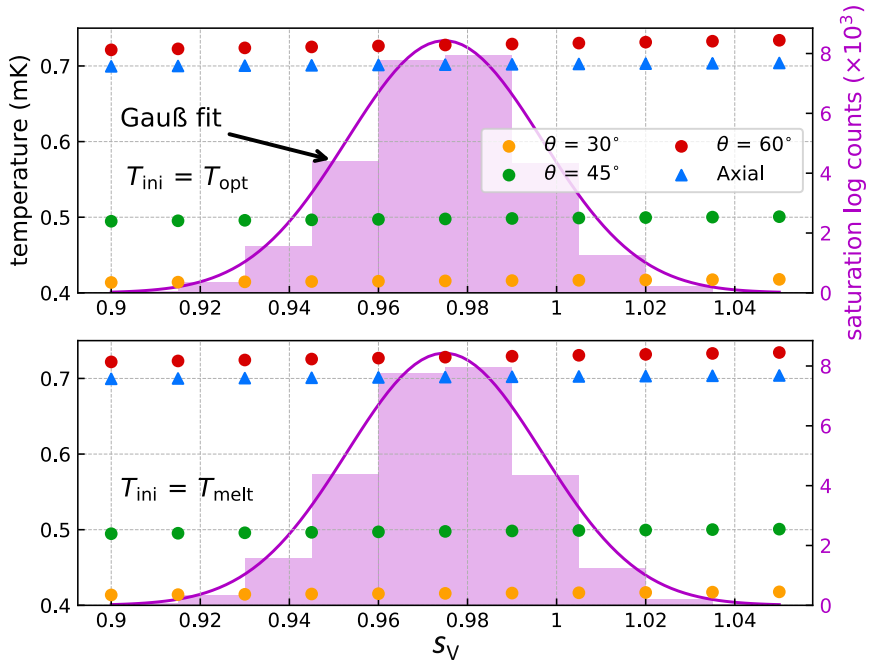

Figure 5.10 End temperatures of the Doppler cooling phase in the presence of 370 nm beam saturation fluctuations. By analogy with the analysis of frequency fluctuations in Fig. 5.9, the saturation s_V of the Doppler cooling beam V is logged over several hours. The resulting data is plotted as histogram (light violet) and fitted (solid violet line) using a Gaussian distribution. From fitting, a standard deviation $\sigma_s \approx 0.02$ and a mean value $\mu_s = 0.975$ is obtained. Using saturation values s_V within the distribution, end temperatures of the Doppler cooling phase are calculated for initial temperatures $T_{ini} = T_{opt}$ (top) and $T_{ini} = T_{melt}$ (bottom). With the fitted distribution, the mean temperatures for the radial and axial modes are calculated and shown in Tab. 13.

As can be seen, observed saturation fluctuations do not have an influence on the end temperatures of the cooling phase. The simulation yields a slight increase as a function of increasing saturation values, which can explained by a decreasing friction coefficient ρ which results in an increasing equilibrium temperature $T_{eq} \propto \rho^{-1}$ (see Eq. 5.14). The increase is on the order of $\approx 1 \ldots 2\,\mu$K and therefore negligible.

Table 13 Mean final temperatures $\langle T_{end} \rangle$ of the Doppler cooling phase assuming $T_{ini} = T_{opt}$ and $T_{ini} = T_{melt}$ in the presence of saturation fluctuations (see Fig. 5.10), temperatures in mK.

mode	30°	45°	60°	axial
$T_{end,ref}$	0.42	0.50	0.73	0.70
$\langle T_{end,s\,fluct,T_{opt}} \rangle$	0.42	0.50	0.73	0.70
$\langle T_{end,s\,fluct,T_{melt}} \rangle$	0.42	0.50	0.73	0.70

5.2.2.6 First comparison with experimental data

As presented in section 2.6, the radial temperatures of the indium ion during the clock pulse can be extracted from Rabi flops by comparison with a theoretical model describing the effect of thermal dephasing of Rabi oscillations. In Fig. 4.11 of 4.1.4, an experimentally acquired Rabi flop is used to determine the clock transition Rabi frequency $|\Omega_0|$ in the ac-Stark shift analysis by comparison with the aforementioned model. The radial temperatures used for the theoretical flops are chosen to be equal to the temperatures determined in this temperature analysis (see

Tab. 11). The theoretical flops show good agreement with the data. Although this first analysis is promising, more experiments are planned, to further verify the results and the validity of the simulation, once the clock is "ticking" again.

5.2.3 Summary

To summarize the results of the analysis, it can be concluded that the mode temperatures during the clock interrogation are completely determined by the cooling phase, regardless of the conditions at the beginning of the clock cycle. As shown in Tab. 8 and 11, the end temperatures barely differ for the worst case initial temperature $T_{\text{ini}} = T_{\text{melt}}$ and optimal conditions $T_{\text{ini}} = T_{\text{opt}}$. Also, when experimental imperfections such as frequency of intensity fluctuations of the 370 nm beams are considered, the resulting increase of the mean mode temperatures could be bound to $\leq 5\%$. It was also shown that the ytterbium and indium detection phases significantly affect the temperature dynamics of all modes, although the influences are different for the axial and radial modes. Especially the indium detection contributes to axial cooling, while the 230 nm fluorescence introduces a radial heating rate of $\approx 0.34\,\text{mK/ms}$. In the analysis of the whole branch 1, the temperatures of all modes could be bound to $\leq 2.5\,\text{mK}$ at the start of the Doppler cooling phase, assuming optimal experimental conditions. The analysis has also shown that the radial trap axes orientation with $\theta = 45°$ represents the best trade-off between the radial mode temperatures of both principle axes, and in addition, could allow to reduce the time $t_{\text{const}\,s}$ and hence the total cooling time of the Doppler cooling phase. A first comparison with experimentally acquired Rabi oscillations show good agreement with the determined radial mode temperatures in this analysis. To completely verify the results, further analysis of experimental data is necessary once the experiment is running again.
In the next section, possible optimizations of the clock cycle branch 1 are analyzed.

5.3 Optimization of sympathetic Doppler cooling

Besides the determination of the mode temperatures, the analysis of section 5.2 showed that the current sequence could be improved by an adjustment of experimental parameters. In the temperature analysis of the cooling phase in Fig. 5.8, it was observed that for the first constant s phase, all modes reach an equilibrium already after $\approx 15\,\text{ms}$. The temperatures remain unchanged for the following 10 ms of cooling time, until the saturation ramp starts after $t_{\text{const}\,s} = 25\,\text{ms}$. Hence, a possible optimization regarding cooling time could be done by reducing $t_{\text{const}\,s}$. On the other hand, instead of a reduction of the total cooling time, the end temperature could be further reduced by an increased time t_{ramp} while keeping the total cooling time of 50 ms. The analysis of the detection phases showed that the indium detection significantly contributed to heating of the radial modes via spontaneous emission. Here it would be interesting to find optimal saturation parameters for $s_{\text{V/H1}}$ to compensate radial heating due to the 230 nm fluorescence. These are examples of possible optimizations analyzed in this section which is structured as follows. At first, in 5.3.1, the indium detection phase is optimized via adjusted saturation parameters s of the 370 nm beams to compensate for radial heating. 5.3.2 presents the results of an optimization of cooling phase regarding minimum end temperatures for a fixed cooling time and afterwards regarding minimized cooling time for fixed end temperatures. Lastly, the influence of an exponential instead of a linear saturation ramp on the end temperatures of the cooling phase is analyzed in 5.3.3 followed by 5.3.4, which briefly summarizes the results of this section.

5.3.1 Compensation of radial heating during In^+ detection

Since the 230 beam is parallel to the trap axis, it contributes considerably to cooling of the axial modes, while the orthogonal radial modes are heated (see Fig. 5.7). This subsection aims for an optimization of the 370 nm saturation parameter s_V (and hence $s_{H1} = 0.3 s_V$) during the indium dectection to compensate for radial heating due to the 230 nm fluorescence. Fig. 5.11 shows the end temperatures of the radial modes in the indium detection phase for $\theta = \{30°, 45°, 60°\}$ as a function of s_V, assuming the end temperatures of the ytterbium detection T_{end,Yb^+det} in Tab. 10.

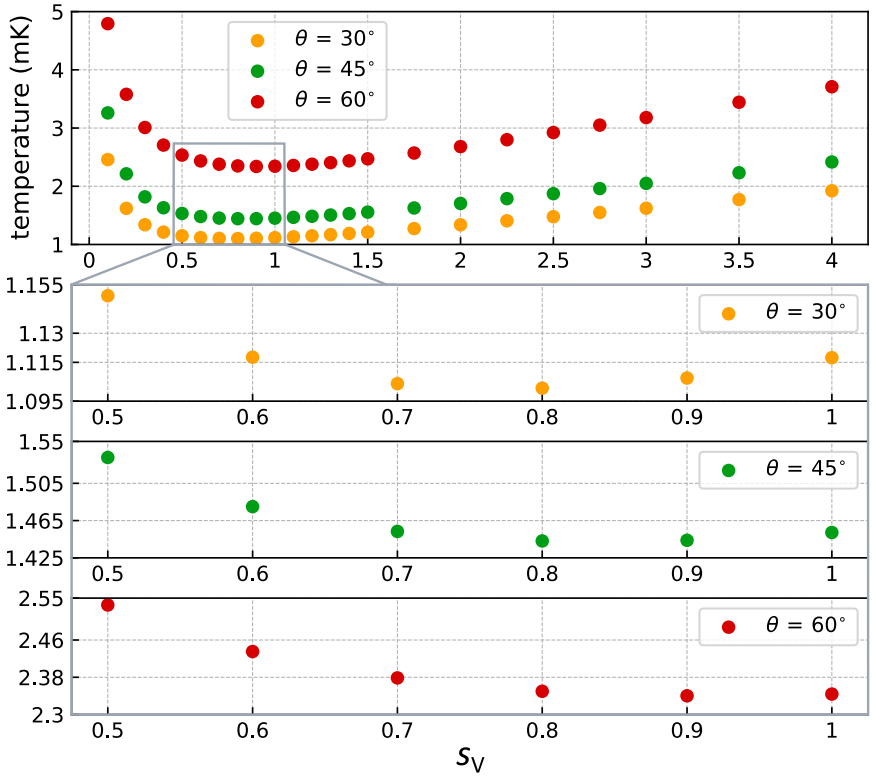

Figure 5.11 Radial end temperatures for the indium detection phase for varying saturation s_V. To counteract the effect of radial heating due to the indium fluorescence, the end temperatures of the radial modes are calculated for different values of s_V (and $s_{H1} \approx 0.3 s_V$). For a saturation of $s_V \approx 0.8 - 0.9$, a minimum of the calculated end temperatures can be observed, while the minimum is shifted to higher values s_V for larger angles θ and hence worse cooling efficiency.

For small ($s_V < 0.5$) and large ($s_V > 1.5$) values of s_V, the calculated end temperatures are rapidly increasing. For small values, the cooling rate due to both 370 nm beams V and H1 is too small to compensate for the heating rate due to the 230 nm fluorescence. This results in an increased equilibrium temperature $T_{eq} \propto 1/c_1$ since the cooling rate $c_1 \to 0$ for $s_{V/H1} \to 0$. For large values of s_V, heating due to the 230 nm fluorescence can be compensated, but now the increase of $s_{eff} = s_V + s_{H1}$ leads to an increase of $T_{eq} \propto \rho^{-1} \propto s_{eff}^2$. Between these extreme cases, an optimum can be found. For all three orientations θ, the end temperatures show minima around $s_V \approx 0.8 \ldots 0.9$, indicating that the saturation of $s_V = 0.5$ in the current clock sequence is not optimal. The minimum temperatures are reached at higher values s_V for increasing θ. This can be explained by the worse cooling efficiency for large values θ and hence worse projection onto the radial cooling beam V. The end temperatures of the radial modes for $s_V = 0.8$ are shown in Tab. 14 together with the corresponding temperatures for $s_V = 0.5$ as calculated in Tab. 10.

Table 14 Radial and axial end temperatures for $s_V = 0.5$ and the optimized value $s_V = 0.8$ as well as resulting end temperature differences, temperatures in mK.

mode	30°	45°	60°	axial
$T_{\mathrm{end,In^+det}}$ ($s_V = 0.5$)	1.15	1.53	2.53	0.03
$T_{\mathrm{end,In^+det}}$ ($s_V = 0.8$)	1.10	1.44	2.35	0.05
$\Delta T_{\mathrm{end,In^+det}}$	0.05	0.09	0.18	−0.02

The optimization yields a possible decrease of the radial end temperatures by $\Delta T_{\mathrm{end,Yb^+det}}$ on the order of 4 . . . 8%. Note that changing s_V to 0.8 results in a slight increase of the axial temperature by 0.02 mK as a result of the increased axial heating coefficient $c_{0,\mathrm{ax},370}$ (see Eq. 5.43). As discussed in the previous section, this temperature is still far below the resulting axial end temperatures of the following cooling phase. Therefore, the increase in the axial end temperature is considered negligible.

To conclude the results, an increase of the saturation s_V can decrease the radial end temperatures of the indium detection and hence the initial temperatures of the cooling phase by $\approx 5\%$. Although this is just a small optimization regarding the end temperatures of the indium detection, the increase of s_{eff} also leads to an increase of the cooling rate $c_{1,370}$. Therefore, increasing s_{eff} during the indium detection also improves the temperature stability of the whole sequence branch 1.

Here it is mentioned, that the experimentally observed 230 nm fluorescence drops for large 370 nm saturations ($s_V \gg 0.5$). This could be explained by an increased heating rate due to 370 nm fluorescence and hence increased axial temperatures. The resulting 1st order Doppler shift of the indium ions then leads to a decreased scattering rate and to a transition between Yb^+ and In^+ dominated axial temperature regimes. To verify this hypothesis, further investigation is necessary as well as a more sophisticated model.

5.3.2 Optimization of the cooling phase

This subsection presents the results of the optimization for the Doppler cooling phase. In general, there are two quantities to be optimized, which have a direct impact on the performance of an atomic clock, the total cooling time and the reached end temperatures. Longer cooling phases reduce the duty cycle and hence increase the statistical uncertainty. Lower ion temperatures yield a higher contrast and a reduced 2nd order Doppler shift. Therefore, it is important to find a good compromise between short cooling times and temperature.

The optimization needs to take into account a large quantity of variables, such as the radial trap axes orientation described by θ, the cooling beam saturation parameters s or the secular frequencies, which affect the coefficients C_α. To reduce the amount of free parameters, some are kept fixed in this analysis. Since the used 370 nm saturation coefficients of $s_V = 1$ and $s_{H1} \approx 0.3$ yield a contrast of 90% for 10 ms clock pulses (see Fig. 4.1.4), and in general led to an overall good performance of the clock during the spring clock campaign, both parameters will be fixed throughout this subsection. Also, the secular frequencies will not be changed to be able to compare the results to the analysis of the previous section. As indicated in the previous section (see e.g. Fig. 5.8), adjusting the ratio of the cooling times $t_{\mathrm{const}\,s}$ and t_{ramp} could either decrease the end temperature of the 50 ms cooling phase or allow a reduction of the total cooling time $t_{\mathrm{cool}} = t_{\mathrm{const}\,s} + t_{\mathrm{ramp}}$ at constant end temperatures. Therefore, the optimization presented in the following uses $t_{\mathrm{const}\,s}$ and t_{ramp} as variable parameters. The analysis of possible optimizations is done for the radial angles $\theta = \{30°, 60°\}$, as these orientations were used during the spring clock campaign, as well as for $\theta = 45°$, which showed the best compromise both radial axes end temperatures. Moreover, since in general the axial modes showed faster cooling dynamics compared to the radial modes, an optimization for the radial mode temperatures will also result in an improvement for the axial modes. Since the axial modes do not contribute to

the temperature dependent loss of contrast (see section 2.6) due to a missing projection on the clock laser, the optimization is focused on the radial mode temperatures.
At first, end temperatures are calculated while the total cooling time $t_{\mathrm{cool}} = t_{\mathrm{const}\,s} + t_{\mathrm{ramp}} = 50\,\mathrm{ms}$ is kept constant. Figure 5.12 shows the end temperatures for different saturation ramp times t_{ramp} between 0 ms and 50 ms, assuming initial temperatures $T_{\mathrm{ini}} = T_{\mathrm{opt}}$. Note that $t_{\mathrm{ramp}} = 0\,\mathrm{ms}$ refers to a cooling phase where $s_{\mathrm{V/H1}}$ are kept constant, while for $t_{\mathrm{ramp}} = 50\,\mathrm{ms}$ both saturation parameters are ramped down throughout the whole cooling phase.

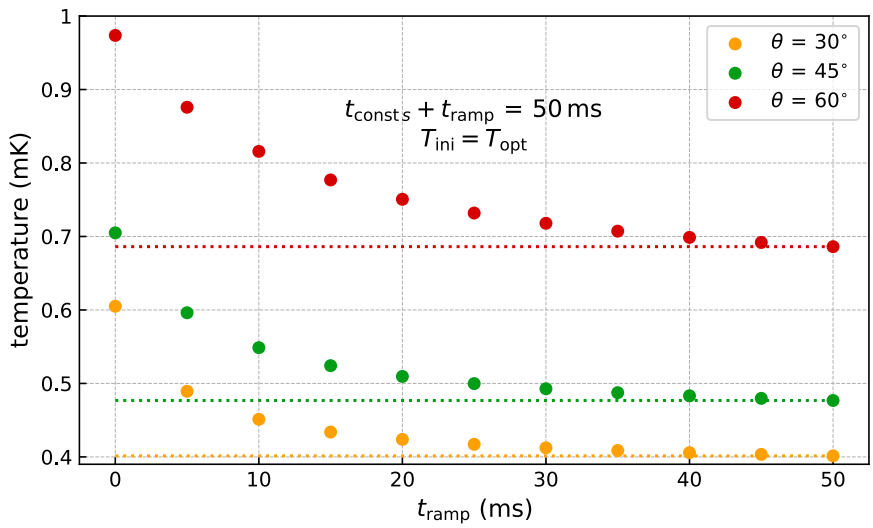

Figure 5.12 Radial end temperatures of the Doppler cooling phase for a fixed cooling time $t_{\mathrm{cool}} = 50\,\mathrm{ms}$ assuming $T_{\mathrm{ini}} = T_{\mathrm{opt}}$. The radial end temperatures of the Doppler cooling phase are calculated for varying $t_{\mathrm{const}\,s}$ and t_{ramp}, such that $t_{\mathrm{cool}} = t_{\mathrm{const}\,s} + t_{\mathrm{ramp}} = 50\,\mathrm{ms}$. The corresponding minima for $\theta = \{30°, 45°, 60°\}$ are highlighted by dotted lines and shown in Tab. 15.

For the radial end temperatures, a monotonic decrease for increasing ramp times t_{ramp} can be observed, with a minimum at $t_{\mathrm{ramp}} = 50\,\mathrm{ms}$, as highlighted by the dotted lines. In general, there are two competing quantities, namely the cooling rate and the equilibrium temperature, which are both functions of the 370 nm saturation. A high cooling rate for large saturations results in fast cooling but high equilibrium temperatures. Once equilibrium is reached, only a decrease of the saturation within ramped s phase can further reduce the mode temperatures. On the other hand, smaller saturations, which decrease the equilibrium temperature, also yield a decreased cooling rate. That the end temperatures are minimized for long ramp times shows that the slower the decrease of the cooling coefficient c_1 due to the saturation ramp is, the better the mode temperatures can follow the decreasing equilibrium temperatures. Note that the decrease of the saturation due to the saturation ramp is inversely proportional to t_{ramp}, since the ramp slope is defined by $a = t_{\mathrm{ramp}}^{-1}$ (see Eq. 5.92). Hence, the longest ramp time yields the smallest saturation decrease per unit time. In a second simulation assuming the worst case initial temperatures $T_{\mathrm{ini}} = T_{\mathrm{melt}}$, the radial end temperatures are the same as for optimal initial temperatures. This shows that an increased ramp time t_{ramp} is not only advantageous regarding the final temperatures of the cooling process, but also results in a similar robustness against high initial temperatures. To compare the currently used Doppler cooling phase and the optimized phase, consisting of $t_{\mathrm{ramp}} = 50\,\mathrm{ms}$, the respective end temperatures are shown in Tab. 15.

Table 15 Minimum radial end temperatures for the current parameters and the optimized setting of $t_{\mathrm{ramp}} = 50\,\mathrm{ms}$ (see Fig. 5.12), temperatures in mK.

mode	30°	45°	60°
T_{end} ($t_{\text{const}\,s} = t_{\text{ramp}} = 25\,\text{ms}$)	0.42	0.50	0.73
T_{end} ($t_{\text{const}\,s} = 0\,\text{ms}$, $t_{\text{ramp}} = 50\,\text{ms}$)	0.40	0.48	0.69
ΔT_{end}	0.02	0.02	0.04

The reduction in the final temperature is on the order of 5%. This indicates that a further decrease of the end temperatures of the cooling phase without an increase of the total cooling time t_{cool} is not possible with the currently used linear ramp.
To investigate a possible further decrease of the mode temperatures, end temperatures are calculated for long saturation ramp without a constant s cooling phase ($t_{\text{const}\,s} = 0$), assuming $T_{\text{ini}} = T_{\text{opt}}$. The resulting temperatures, together with calculated theoretical limits T_{lim}(dashed lines) for $t_{\text{ramp}} \to \infty$, are shown in Fig. 5.13. In Tab. 16, T_{lim} as well as calculated temperatures for $t_{\text{ramp}} = \{50, 100, 200, 300, 800\}$ ms are shown.

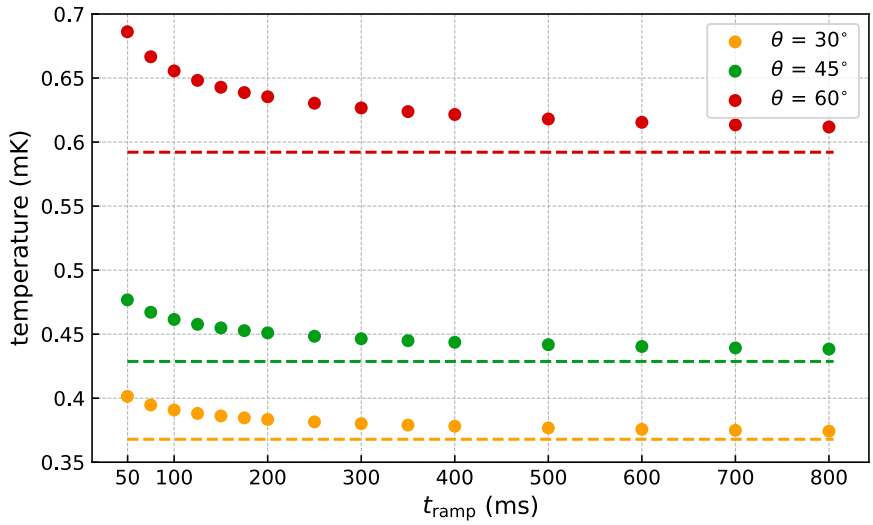

Figure 5.13 Radial end temperatures for long ramp times. Radial end temperatures of the Doppler cooling phase are calculated assuming $t_{\text{const}\,s} = 0$.

As can be seen, the temperatures converge to the limit temperatures shown as dashed lines. For a ramp time of $t_{\text{ramp}} = 50\,\text{ms}$, the reached end temperatures are within $\approx 8\ldots17\%$ of T_{lim}. Doubling the ramp time to $t_{\text{ramp}} = 100\,\text{ms}$ results in a further decrease of the radial end temperatures of $\approx 3\ldots5\%$, while a 16-fold increase to $t_{\text{ramp}} = 800\,\text{ms}$ only yields a reduction of $\approx 8\ldots12\%$ (see Tab. 16). Note that the simulation assumes the absence of external sources of heat.

Table 16 Radial end temperatures for long ramp times t_{ramp} and limit temperatures T_{lim} (see Fig. 5.13), temperatures in mK.

mode	30°	45°	60°
T_{end} ($t_{\text{ramp}} = 50\,\text{ms}$)	0.40	0.48	0.69
T_{end} ($t_{\text{ramp}} = 100\,\text{ms}$)	0.39	0.46	0.66
T_{end} ($t_{\text{ramp}} = 200\,\text{ms}$)	0.38	0.45	0.64
T_{end} ($t_{\text{ramp}} = 300\,\text{ms}$)	0.38	0.45	0.63
T_{end} ($t_{\text{ramp}} = 800\,\text{ms}$)	0.37	0.44	0.61
T_{lim} ($t_{\text{ramp}} \to \infty$)	0.37	0.43	0.59

Here it is mentioned that the temperature limit of the axial modes is calculated to be $T_{\mathrm{lim,ax}} = 0.65\,\mathrm{mk}$. Using this, the mean limit temperature $\langle T \rangle_{\mathrm{lim}}$ over all three principal axis is calculated to be

$$\langle T \rangle_{\mathrm{lim}} = \frac{T_{\mathrm{lim,ax}} + T_{\mathrm{lim},\theta=30^\circ} + T_{\mathrm{lim},\theta=60^\circ}}{3} \approx 0.54\,\mathrm{mK}, \tag{5.96}$$

while in case of $\theta = 45^\circ$ for both radial axes, $\langle T \rangle_{\mathrm{lim}} \approx 0.5\,\mathrm{mK}$. As expected from Doppler cooling, the determined mean temperatures $\langle T \rangle_{\mathrm{lim}}$ are on the order of the ytterbium Doppler limit $T_{\mathrm{D,Yb}} \approx 0.47\,\mathrm{mK}$. It can be seen that mode temperatures $T_\alpha < T_{D,\mathrm{Yb}}$ along one principal axis always result in $T_\alpha > T_{D,\mathrm{Yb}}$ for at least one other axis such that $\langle T \rangle_{\mathrm{lim}} \geq T_{\mathrm{D,Yb}}$ holds.
At this point, a further increase of the cooling time does not seem sensible. Therefore, in the next step, the cooling phase is optimized regarding the total cooling time t_{cool}.

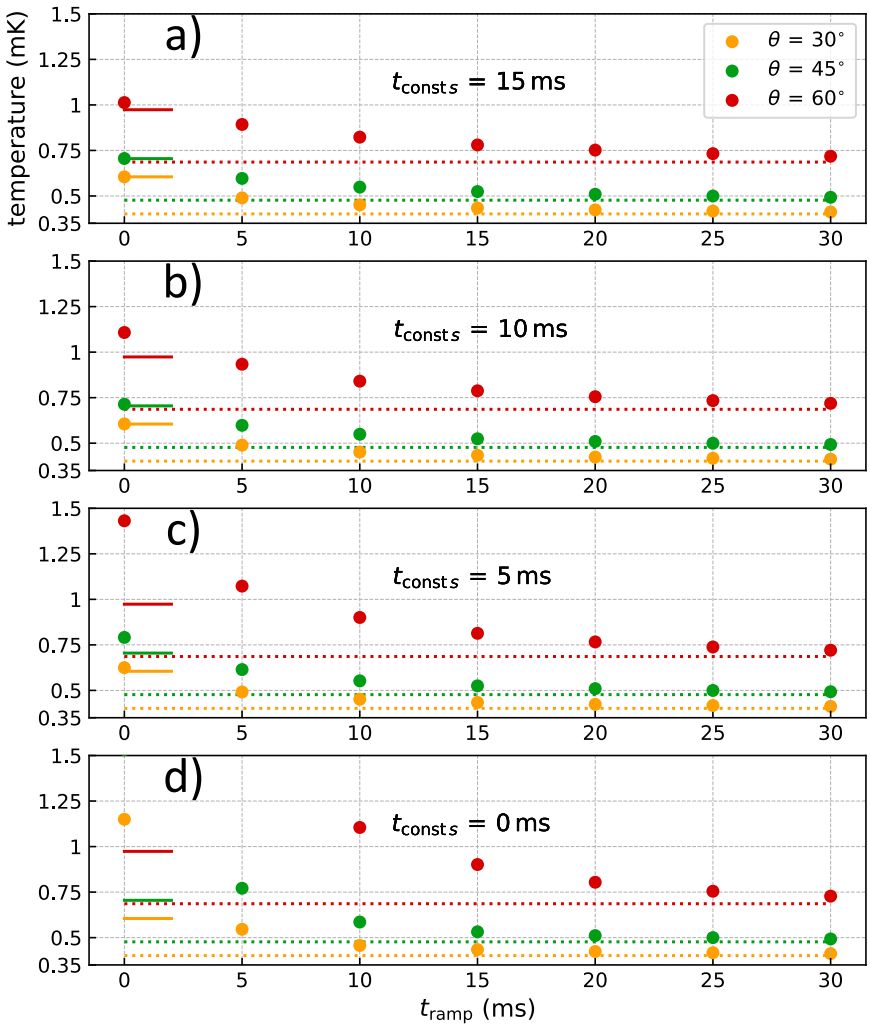

Figure 5.14 Radial end temperatures of the a Doppler cooling phase for different combinations of $t_{\mathrm{const}\,s}$ and t_{ramp}. a), b), c) and d) show radial end temperatures of the Doppler cooling phase assuming fixed constant s phases with $t_{\mathrm{const}\,s} = \{15, 10, 5, 0\}$ ms and varying ramped s times t_{ramp} between 0 ms and 30 ms, assuming $T_{\mathrm{ini}} = T_{\mathrm{opt}}$. To find a compromise between low end temperatures and short total cooling times $t_{\mathrm{cool}} = t_{\mathrm{const}\,s} + t_{\mathrm{ramp}}$, the end temperatures for $t_{\mathrm{cool}} = t_{\mathrm{ramp}} = 50$ ms (dotted lines) are used as benchmarks. The solid lines show the equilibrium temperature of the constant s phase.

The goal of this optimization is to reach comparable end temperatures as for $t_{\mathrm{cool}} = 50$ ms for a reduced total cooling time. Here the minimum temperatures obtained for a 50 ms ramp

highlighted by dotted lines in Fig. 5.12 are used as benchmarks. For the optimization, radial end temperatures are calculated for ramp times t_{ramp} between $0 \ldots 30\,\mathrm{ms}$ and for different constant s times $t_{\mathrm{const}\,s}$ assuming initial temperatures $T_{\mathrm{ini}} = T_{\mathrm{opt}}$ and $T_{\mathrm{ini}} = T_{\mathrm{melt}}$ (see figures 5.14 and 5.15) where again the total cooling time is $t_{\mathrm{cool}} = t_{\mathrm{ramp}} + t_{\mathrm{const}\,s}$. The solid lines at a ramp time of 0 ms show the equilibrium temperatures $T_{\mathrm{eq,const}\,s}$ of the constant s phase. At first, the cooling phase is optimized for optimal initial temperatures $T_{\mathrm{ini}} = T_{\mathrm{opt}}$, leading to the most time efficient cooling phase. Afterwards, an optimization is presented for the worst case $T_{\mathrm{ini}} = T_{\mathrm{melt}}$. For optimal initial temperatures $T_{\mathrm{ini}} = T_{\mathrm{opt}}$, the radial mode temperatures of all projections θ are already close to equilibrium after $t_{\mathrm{const}\,s} = 10\,\mathrm{ms}$, as can be seen by comparison with the solid lines in Fig. 5.14 a) and b) for $t_{\mathrm{ramp}} = 0$. While for small ramp times $t_{\mathrm{ramp}} \leq 15\,\mathrm{ms}$ the end temperatures show significant differences depending on the constant s phase and hence $t_{\mathrm{const}\,s}$, for longer ramp times $t_{\mathrm{ramp}} \geq 20\,\mathrm{ms}$, the differences become negligible. This shows that for long ramp times (and hence small ramp slopes $a = t_{\mathrm{ramp}}^{-1}$), the cooling coefficient c_1 is still high enough to enable fast cooling, while at the end, the scattering rate is sufficiently small to reach low temperatures. Here the advantage of the saturation ramp becomes obvious. In the beginning of the cooling phase, a high scattering rate is needed to quickly decrease the initial temperatures. Since for long cooling ramps ($t_{\mathrm{ramp}} \geq 25\,\mathrm{ms}$) the decrease of the scattering rate is slow, the overall temperature decrease in the beginning is comparable to the constant s phase. After a few ms of cooling time, cooling with constant s is limited by the respective equilibrium temperature, and the temperature decrease per unit time is decreased exponetially (since $\dot{T}_\alpha(t) \propto \exp(-c_1 t)$). For the saturation ramp, the equilibrium temperature is a function of time. Therefore, the scattering rate and the equilibrium temperature are continuously adjusted, leading to an almost linear temperature decrease as can be seen in e.g. Fig. 5.8. In addition, it can be seen that the benchmark temperatures for a cooling phase with $t_{\mathrm{ramp}} = 50\,\mathrm{ms}$ are already approximately reached after a ramp time of $t_{\mathrm{ramp}} = 30\,\mathrm{ms}$ (see 5.14 d)). This verifies the observation in Fig. 5.13, that towards the end of the ramp time, the temperature decrease is extremely slow and time consuming. Therefore, in case of the combination $\theta = \{30°, 60°\}$[8] and for optimal initial temperatures T_{opt}, the cooling phase could be decreased to $t_{\mathrm{cool}} = t_{\mathrm{ramp}} = 30\,\mathrm{ms}$ (see Fig. 5.14 d)), or, to improve the robustness against high initial temperatures, to $t_{\mathrm{cool}} = 35\,\mathrm{ms}$ with a 5 ms constant s phase (Fig. 5.14 c)). In case of a trap axis orientation $\theta = 45°$ where the modes of both radial axes are equal, the cooling phase could be further reduced by 10 ms. Here again two options are proposed for the same reasoning, $t_{\mathrm{cool}} = t_{\mathrm{ramp}} = 20\,\mathrm{ms}$ and $t_{\mathrm{cool}} = 25\,\mathrm{ms}$ with a 5 ms constant s cooling time. To quantitatively compare these optimizations, the respective end temperatures, benchmark temperatures and end temperatures of the currently used cooling phase are shown in Tab. 17. The end temperatures of the proposed options for the trap axes orientations $\theta = \{30°, 60°\}$ and for $\theta = 45°$ are highlighted by square brackets.

Table 17 Possible optimizations for $t_{\mathrm{const}\,s}$ and t_{ramp}, with respective radial end temperatures for $\theta = \{30°, 60°\}$ and $\theta = 45°$ (see values in square brackets) assuming $T_{\mathrm{ini}} = T_{\mathrm{opt}}$, temperatures in mK.

mode	30°	45°	60°
T_{end} ($t_{\mathrm{const}\,s} = t_{\mathrm{ramp}} = 25\,\mathrm{ms}$)	0.42	0.50	0.73
T_{end} ($t_{\mathrm{const}\,s} = 0\,\mathrm{ms}$, $t_{\mathrm{ramp}} = 50\,\mathrm{ms}$)	0.40	0.48	0.69
T_{end} ($t_{\mathrm{const}\,s} = 5$, $t_{\mathrm{ramp}} = 30\,\mathrm{ms}$)	[0.41]	0.49	[0.72]
T_{end} ($t_{\mathrm{const}\,s} = 0$, $t_{\mathrm{ramp}} = 30\,\mathrm{ms}$)	[0.41]	0.49	[0.73]
T_{end} ($t_{\mathrm{const}\,s} = 5$, $t_{\mathrm{ramp}} = 20\,\mathrm{ms}$)	0.42	[0.51]	0.77
T_{end} ($t_{\mathrm{const}\,s} = 0$, $t_{\mathrm{ramp}} = 20\,\mathrm{ms}$)	0.42	[0.51]	0.80

For $\theta = \{30°, 60°\}$, the total cooling time can be decreased by $30 \ldots 40\%$ while reducing the

[8] Remember that since both radial trap axes are orthogonal, an angle of $\theta = 30°$ for one trap axis results in $\theta = 90° - 30° = 60°$ for the other axis, as can be seen in Fig. 5.1.

end temperatures by $\approx 1\%$ compared to the cooling phase used in the spring clock campaign ($t_{\text{const}\,s} = t_{\text{ramp}} = 25\,\text{ms}$). Compared to the benchmark temperatures for $t_{\text{cool}} = t_{\text{ramp}} = 50\,\text{ms}$, reducing the cooling time results in $2\ldots5\%$ higher end temperatures. For $\theta = 45°$ the cooling time could be further reduced to $40\ldots50\%$ while the corresponding end temperature increase is $\approx 2\%$ relative to the cooling phase in the clock sequence or $\approx 7\%$ relative to the 50 ms ramp. Since the temperature differences between the proposed options with and without a 5 ms constant s phase are on the order of μK, it could be neglected for optimal initial Temperatures $T_{\text{ini}} = T_{\text{opt}}$.
For the worst case initial temperatures $T_{\text{ini}} = T_{\text{melt}}$, the situation is different. As can be seen in Fig. 5.15, the higher initial temperatures result in the need of longer cooling times at constant saturation.

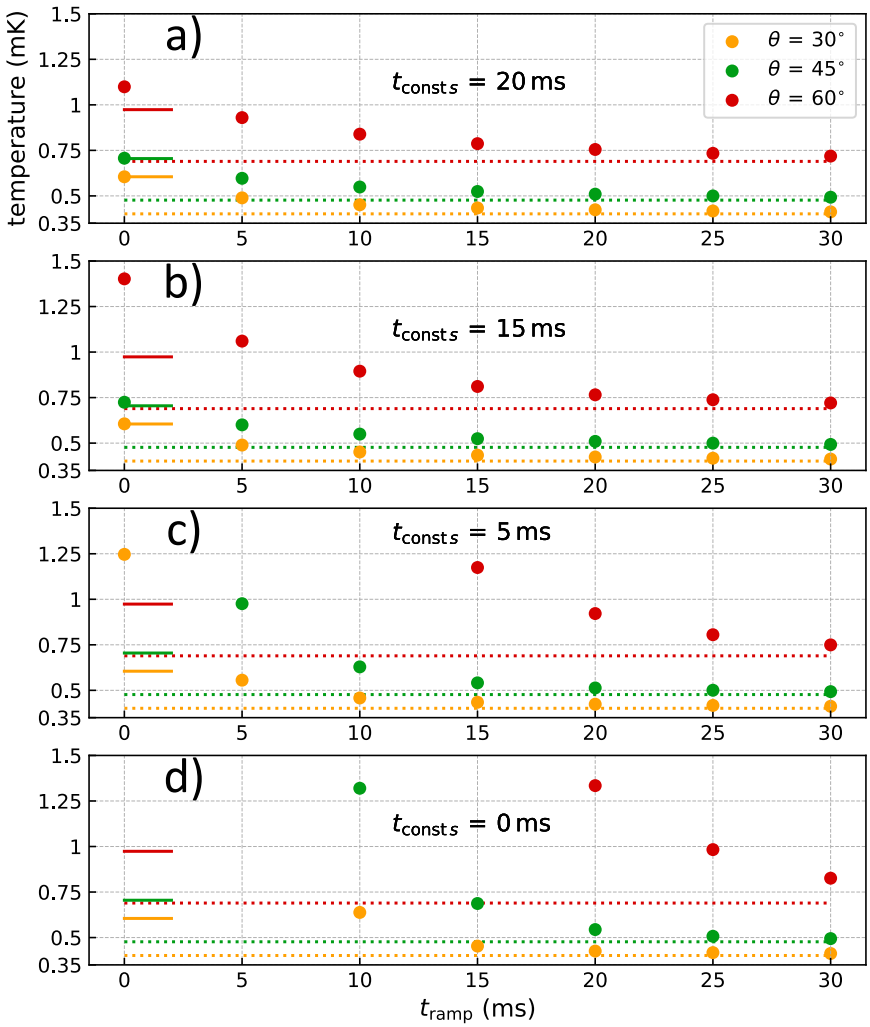

Figure 5.15 Radial end temperatures of the Doppler cooling phase for different combinations of $t_{\text{const}\,s}$ and t_{ramp} and for worst case initial conditions $T_{\text{ini}} = T_{\text{melt}}$. a), b), c) and d) show radial end temperatures of the Doppler cooling phase assuming fixed constant s phases with $t_{\text{const}\,s} = \{20, 15, 5, 0\}$ ms and varying ramped s times t_{ramp} between 0 ms and 30 ms.

Here $t_{\text{const}\,s} = 15\,\text{ms}$ is necessary to get close to equilibrium for all radial modes (see Fig. 5.15 b), solid lines at 0 ms ramp time). While the temperatures for $T_{\text{ini}} = T_{\text{opt}}$ and for long ramp times $t_{\text{ramp}} \leq 20\,\text{ms}$ show just a small dependence on the length of the constant s phase, for $T_{\text{ini}} = T_{\text{melt}}$ the calculated end temperatures differ significantly depending on $t_{\text{const}\,s}$, especially for the worst cooled modes at $\theta = 60°$ (compare Fig. 5.15 b) and d)). This shows the importance

of the constant s phase when a broad range of initial temperatures needs to be covered. To keep comparable end temperatures as for the options given in Tab. 17, for $\theta = \{30°, 60°\}$, a cooling phase with a constant s phase of $t_{\text{const}\,s} = 5\,\text{ms}$ and a ramp time of $t_{\text{ramp}} = 30\,\text{ms}$ is proposed. For $\theta = 45°$, the dependence of the end temperatures on the length of the constant s is negligible for ramp times $t_{\text{ramp}} \geq 25\,\text{ms}$ (see Fig. 5.15 d)). Therefore, for this trap axes configuration, a cooling phase $t_{\text{cool}} = t_{\text{ramp}} = 25\,\text{ms}$ is a good compromise between the reduction of the total cooling time and reaching low end temperatures. The respective end temperatures are shown in Tab. 18.

Table 18 Possible optima (square brackets) for $t_{\text{const}\,s}$ and t_{ramp} with respective radial end temperatures for $\theta = \{30°, 60°\}$ and $\theta = 45°$ assuming $T_{\text{ini}} = T_{\text{melt}}$, temperatures in mK.

mode	30°	45°	60°
T_{end} ($t_{\text{const}\,s} = t_{\text{ramp}} = 25\,\text{ms}$)	0.42	0.50	0.73
T_{end} ($t_{\text{const}\,s} = 0\,\text{ms}$, $t_{\text{ramp}} = 50\,\text{ms}$)	0.40	0.48	0.69
T_{end} ($t_{\text{const}\,s} = 5\,t_{\text{ramp}} = 30\,\text{ms}$)	[0.41]	0.49	[0.75]
T_{end} ($t_{\text{const}\,s} = 0\,t_{\text{ramp}} = 25\,\text{ms}$)	0.42	[0.51]	0.98

For the worst case initial temperatures $T_{\text{ini}} = T_{\text{melt}}$, the cooling phase for $\theta = \{30°, 60°\}$ could be reduced by 30% while obtaining comparable temperatures as for $t_{\text{const}\,s} = t_{\text{ramp}} = 25\,\text{ms}$ (within $\approx 3\%$ deviation). For $\theta = 45°$ a reduction of 50% is possible while the temperature increase is $\approx 2\%$. Compared to the benchmark temperatures for $t_{\text{cool}} = t_{\text{ramp}} = 50\,\text{ms}$, the proposed optimizations yield an end temperature increase between $3 \ldots 9\%$ for $\theta = \{30°, 60°\}$ and $\approx 6\%$ for $\theta = 45°$. Here it becomes clear that a reduction of the cooling time also results in a decreased robustness against high initial temperatures. Regarding the fact that the assumed initial temperatures $T_{\text{ini}} = T_{\text{melt}}$ describe the worst case scenario, accepting a possible maximum end temperature increase of $\approx 10\%$ while decreasing the total cooling time by 40% might be a considerable trade-off.
After the cooling phase was optimized for the currently used linear saturation ramp, in the next subsection, the temperature analysis of the cooling phase is carried out under use of an exponential ramp.

5.3.3 Analysis of an exponential saturation ramp

For the analysis, the linear ramp function in Eq. 5.92 is replaced with an exponential function of the form

$$\exp(t) = e^{-a_{\text{exp}} t}, \tag{5.97}$$

where a_{exp} is an additional parameter in the model. For the linear ramp, the slope $a = t_{\text{ramp}}$ is determined by the ramp time t_{ramp}. The parameter a_{exp} now allows to shape the saturation ramp for fixed t_{ramp}. Here the idea is to investigate whether a faster decrease of the saturation in the beginning of the cooling phase, and hence a faster decrease of the equilibrium temperatures could be advantageous compared to the above analyzed linear saturation decrease. To illustrate the cooling dynamics of an exponential compared to a linear ramp function independent of a constant s phase, end temperatures for $t_{\text{ramp}} = 250\,\text{ms}$ are calculated, assuming $T_{\text{ini}} = T_{\text{opt}}$. Since there is now an additional free parameter a_{exp}, the end temperatures are calculated for different $1/e$ times $t_{\text{exp}} = a_{\text{exp}}^{-1}$. Fig. 5.16 shows the resulting temperatures, together with the theoretical limits T_{lim} for $t_{\text{ramp}} \to \infty$ and the corresponding end temperatures of a linear saturation ramp with $t_{\text{ramp}} = 250\,\text{ms}$.

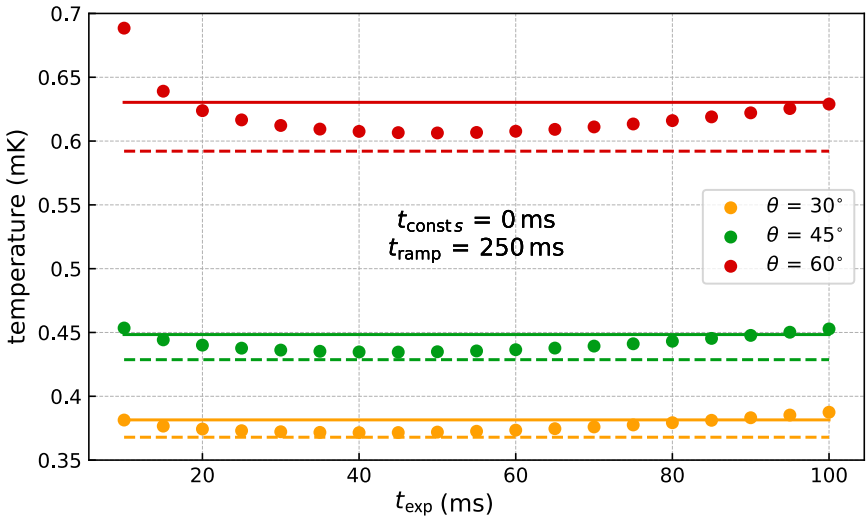

Figure 5.16 Radial end temperatures for an exponential saturation ramp. Radial end temperatures for a fixed ramp time of $t_{\text{ramp}} = 250\,\text{ms}$ are calculated for varying $1/e$ times $t_{\text{exp}} = a_{\text{exp}}^{-1}$. End temperatures for a linear saturation ramp for $t_{\text{ramp}} = 250\,\text{ms}$ are plotted as solid lines. The end temperature limits T_{lim} for $t_{\text{ramp}} \to \infty$ are shown as dashed lines for comparison. For the exponential ramp and for each θ, a minimum can be observed for $1/e$ times around $t_{\text{exp,opt}} \approx 45\,\text{ms}$ (see Tab. 19).

For all angles θ and for $1/e$ times t_{exp} between $20 - 80\,\text{ms}$, the calculated end temperatures for the exponential ramp are lower than the corresponding temperatures of a linear ramp. In addition, an optimal $1/e$ time can be found for every θ where the calculated end temperatures reach a minimum. This can be explained by investigating the limits of the exponential for $t_{\text{exp}} \to 0$ and $t_{\text{exp}} \to \infty$. For $t_{\text{exp}} \to 0$, the exponential ramp becomes constant such that the final temperatures are limited by the equilibrium temperatures for the high s phase $t_{\text{eq,const}\,s}$ (see e.g. Tab. 11). For $t_{\text{exp}} \to \infty$, the exponential becomes a step function which results in an instantaneous drop of the 370 nm saturation to 0 and hence a stop of the cooling dynamic. In between, as shown in Fig. 5.16, there is an optimum $t_{\text{exp,opt}}$ for which the end temperatures are minimized. This optimum is increasing for increasing angles θ. Smaller $1/e$ times lead to a faster decrease of the equilibrium temperature. The extent to which the radial mode temperatures are able to follow the decreasing equilibrium depends on the cooling coefficient c1 which depends on θ via the projection $k_{\text{rad,V}} \propto \cos(\theta)$ (Eqs. 5.24 and 5.40). Hence, small angles θ result in small times $t_{\text{exp,opt}}$. For a quantitative analysis, the minimum end temperatures for the optimal 1/e times $t_{\text{exp,opt}} \approx 45\,\text{ms}$, limit temperatures T_{lim} and end temperatures for a linear ramp with $t_{\text{ramp}} = 250\,\text{ms}$ are shown in Tab. 19.

Table 19 Minimum radial end temperatures for an exponential ($t_{\text{exp,opt}} \approx 45\,\text{ms}$) and a linear saturation ramp of length $t_{\text{ramp}} = 250\,\text{ms}$ as well as limit temperatures (see Fig. 5.16), temperatures in mK.

mode	30°	45°	60°
T_{lim} ($t_{\text{ramp}} \to \infty$)	0.37	0.43	0.59
T_{end} ($t_{\text{ramp}} = 250\,\text{ms}$)	0.38	0.45	0.63
T_{end} ($t_{\text{exp,opt}} \approx 45\,\text{ms}$)	0.37	0.43	0.61

As can be seen, the resulting minimum end temperatures for $\theta = \{30°, 45°, 60°\}$ (at $t_{\text{exp,opt}} \approx 45\,\text{ms}$ for the exponential ramp are close to the limit temperature T_{lim}. The temperature differences are on the order of $\approx 1\%$. On the other hand, the end temperatures using the exponential

ramp are about 5% smaller compared to the linear ramp. This shows that when t_{exp} is properly chosen, the exponential ramp can further decrease the end temperatures for a fixed cooling time. As a next step, the exponential ramp is investigated using total cooling times $t_{\mathrm{cool}} = t_{\mathrm{const}\,s} + t_{\mathrm{ramp}} = 35\,\mathrm{ms}$ as proposed for $\theta = \{30°, 60°\}$ in the previous optimization of cooling phase. Here the end temperatures are again calculated for $T_{\mathrm{ini}} = T_{\mathrm{opt}}$ and for different constant s times (see Fig. 5.17). The end temperatures $T_{\mathrm{end,ref}}$ of the optimized cooling phase ($t_{\mathrm{const}\,s} = 5\,\mathrm{ms}$ and $t_{\mathrm{ramp}} = 30\,\mathrm{ms}$) under use of a linear ramp serve as reference (shown as solid lines). In addition, the temperature limits T_{lim} are again plotted as dashed lines.

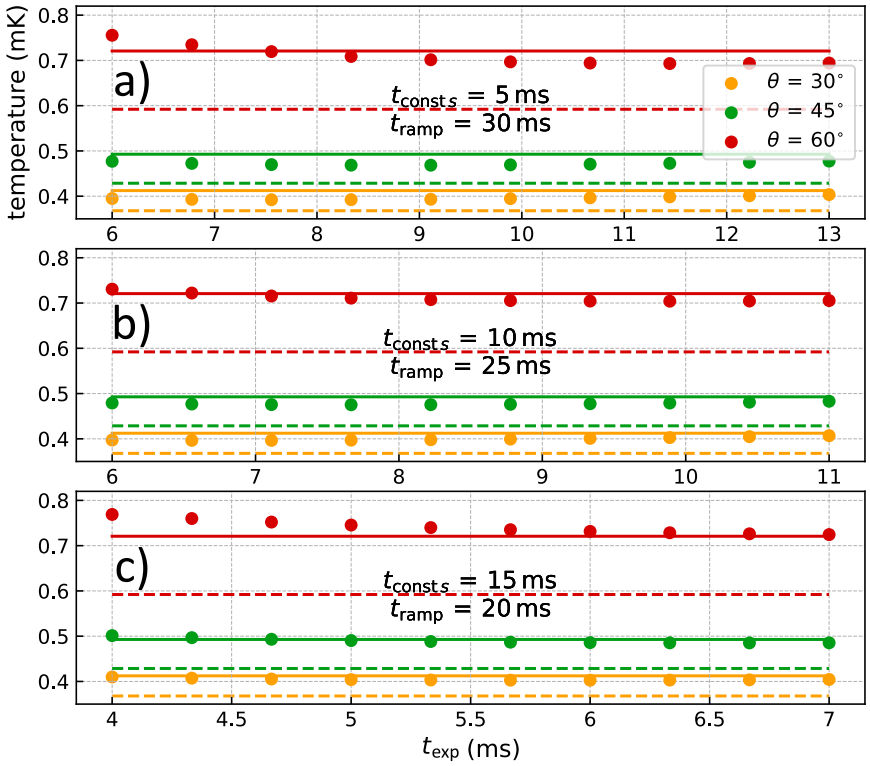

Figure 5.17 Radial end temperatures of cooling phase for $t_{\mathrm{cool}} = 35\,\mathrm{ms}$ under use of an exponential ramp assuming $T_{\mathrm{ini}} = T_{\mathrm{opt}}$. End temperatures for cooling phases with combinations $t_{\mathrm{const}\,s} = 5\,\mathrm{ms}$ and $t_{\mathrm{ramp}} = 30\,\mathrm{ms}$ (a), $t_{\mathrm{const}\,s} = 10\,\mathrm{ms}$ and $t_{\mathrm{ramp}} = 25\,\mathrm{ms}$ (b) as well as $t_{\mathrm{const}\,s} = 15\,\mathrm{ms}$ and $t_{\mathrm{ramp}} = 20\,\mathrm{ms}$ (c) are calculated for varying $1/e$ times t_{exp}. For each combination, the x-axis is adjusted to show the minimal end temperatures. Solid lines show the reference temperatures $T_{\mathrm{end,ref}}$, dashed lines the limit temperatures T_{lim}.

For optimal initial temperatures, the use of an exponential ramp results in an overall end temperature decrease compared to the cooling phase under use of a linear ramp. Just for the shortest ramp time $t_{\mathrm{ramp}} = 20\,\mathrm{ms}$ in Fig. 5.17 c), a temperature increase can be observed for the worst cooled radial modes with $\theta = 60°$. In general, the same trend of decreasing end temperatures for increasing ramp time t_{ramp} can be observed as it was the case for the linear ramp. This shows that although the saturation decrease in the beginning of the ramped s phase is steeper for the exponential ramp, the corresponding scattering rate is still large enough to yield a fast temperature decrease in the beginning of the ramped s phase. Here the exponential ramp gains from the resulting lower equilibrium temperatures, which counteract the smaller cooling coefficient c_1. The lowest temperatures are reached for a cooling phase with constant s phase of $t_{\mathrm{const\,s}} = 5\,\mathrm{ms}$, a ramp time of $t_{\mathrm{ramp}} = 30\,\mathrm{ms}$ (same as for the linear ramp) and for $t_{\mathrm{exp,opt}} \approx 10\,\mathrm{ms}$. Again, the optimal $1/e$ time shows slight differences for the three angles θ. When the modes of the radial axes are not equally cooled, as it is the case for $\theta \neq 45°$, it is

necessary to find a compromise for the end temperatures of both radial axes. The resulting minimum temperatures for $t_{\mathrm{exp,opt}} \approx 10\,\mathrm{ms}$ are shown in Tab. 20.

Table 20 Minimum radial end temperatures obtained for a fixed cooling time $t_{\mathrm{cool}} = 35\,\mathrm{ms}$, an exponential saturation ramp and for $T_{\mathrm{ini}} = T_{\mathrm{opt}}$, temperatures in mK.

mode	30°	45°	60°
T_{lim} ($t_{\mathrm{ramp}} \to \infty$)	0.37	0.43	0.59
$T_{\mathrm{end,ref}}$ ($t_{\mathrm{const}\,s} = 5\,\mathrm{ms}$, $t_{\mathrm{ramp}} = 30\,\mathrm{ms}$)	0.41	0.49	0.72
T_{end} ($t_{\mathrm{const}\,s} = 5\,\mathrm{ms}$, $t_{\mathrm{ramp}} = 30\,\mathrm{ms}$, $t_{\mathrm{exp,opt}} \approx 10\,\mathrm{ms}$)	0.40	0.47	0.70

As can be seen, the use of an exponential ramp results in a further decrease of the end temperatures T_{end} by $\approx 4\%$ compared to the same cooling phase under use of a linear ramp ($T_{\mathrm{end,ref}}$). The temperature difference to the temperature limits T_{lim} are on the order of 8% for the best cooled radial modes at $\theta = 30°$ and $\approx 16\%$ for the worst cooled modes at $\theta = 60°$.
Lastly, the robustness against high initial temperatures is analyzed. For the analysis, the end temperatures are again calculated, but now under the assumption of $T_{\mathrm{ini}} = T_{\mathrm{melt}}$ (Fig. 5.18).

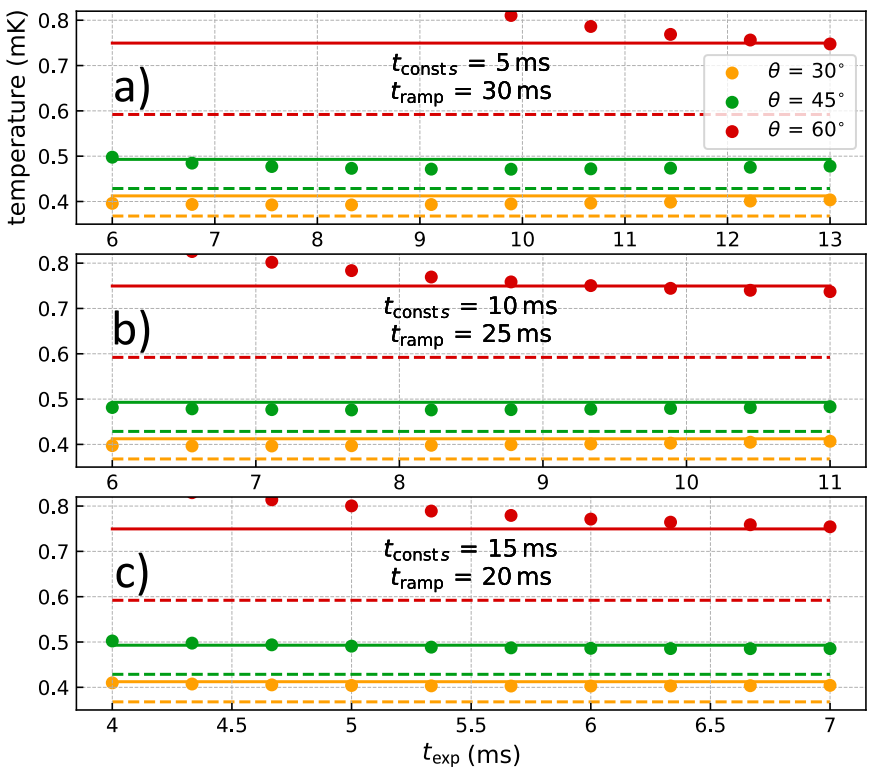

Figure 5.18 Radial end temperatures of the cooling phase for $t_{\mathrm{cool}} = 35\,\mathrm{ms}$ under use of an exponential ramp assuming $T_{\mathrm{ini}} = T_{\mathrm{melt}}$.

Again, the lowest temperatures are obtained for $\theta = \{30°, 45°\}$ using a cooling phase with $t_{\mathrm{const}\,s} = 5\,\mathrm{ms}$ and $t_{\mathrm{ramp}} = 30\,\mathrm{ms}$ (see Fig. 5.18 a)). The situation is different for the worst cooled modes at $\theta = 60°$. Here the constant s phase is not long enough to sufficiently reduce the higher initial temperatures before the exponential ramp starts. Due to the resulting higher temperatures present at the beginning of the ramped s phase, the faster decrease of the cooling coefficient c_1 is disadvantageous. To reach comparable end temperatures as for the linear ramp, it is necessary to increase the constant s phase to $t_{\mathrm{const}\,s} = 10\,\mathrm{ms}$ (see Fig. 5.18 b)). On the other hand, a further increase to $t_{\mathrm{const}\,s} = 15\,\mathrm{ms}$, as shown in Fig. 5.18 c) again results in an

increase of the end temperatures. For every total cooling time t_{cool}, there exists an optimal ratio between $t_{\mathrm{const}\,s}$ and t_{ramp}. In case of the used $t_{\mathrm{cool}} = 35\,\mathrm{ms}$, two cooling phases are proposed. The first uses a short constant s phase of $t_{\mathrm{const}\,s} = 5\,\mathrm{ms}$ and ramp phase of $t_{\mathrm{ramp}} = 30\,\mathrm{ms}$ with $t_{\mathrm{exp,opt}} \approx 10\,\mathrm{ms}$, which results in lower temperatures for optimal initial temperatures, but a decreased robustness against $T_{\mathrm{ini}} = T_{\mathrm{melt}}$ (compare figures 5.17 a) and 5.18 a)). The second combination yields an improved robustness due to a longer constant s phase of $t_{\mathrm{const}\,s} = 10\,\mathrm{ms}$ but higher end temperatures for optimal initial temperatures due do a shorter ramp phase with $t_{\mathrm{ramp}} = 25\,\mathrm{ms}$ and $t_{\mathrm{exp,opt}} \approx 9\,\mathrm{ms}$. The end temperatures of the proposed cooling phases for $T_{\mathrm{ini}} = T_{\mathrm{melt}}$ are shown in Tab. 21.

Table 21 Radial end temperatures for two proposed optimized cooling phases under use of an exponential ramp and assuming $T_{\mathrm{ini}} = T_{\mathrm{melt}}$, temperatures in mK.

mode	30°	45°	60°
T_{lim} ($t_{\mathrm{ramp}} \to \infty$)	0.37	0.43	0.59
$T_{\mathrm{end,ref}}$ ($t_{\mathrm{const}\,s} = 5\,\mathrm{ms}$, $t_{\mathrm{ramp}} = 30\,\mathrm{ms}$)	0.41	0.49	0.75
T_{end} ($t_{\mathrm{const}\,s} = 5\,\mathrm{ms}$, $t_{\mathrm{ramp}} = 30\,\mathrm{ms}$, $t_{\mathrm{exp,opt}} \approx 10\,\mathrm{ms}$)	0.40	0.47	0.79
T_{end} ($t_{\mathrm{const}\,s} = 10\,\mathrm{ms}$, $t_{\mathrm{ramp}} = 25\,\mathrm{ms}$, $t_{\mathrm{exp,opt}} \approx 9\,\mathrm{ms}$)	0.40	0.48	0.76

Both proposed options lead to lower temperatures for $\theta = \{30°, 45°\}$ compared to the cooling phase under use of a linear ramp and therefore a good robustness against high initial temperatures. The end temperatures are increased for $\theta = 60°$. This shows that modes with small θ, and hence with a large cooling coefficient c_1 rather gain from an exponential ramp than worse cooled modes (such as for $\theta = 60°$). This also indicates that an equal projection of $\theta = 45°$ of the cooling beam V onto both radial trap axes' modes is a sensible choice in combination with an exponential ramp.

5.3.4 Summary

This section presented possible optimizations of the phases in clock sequence branch 1 (see Fig. 3.3). Based on the results of the previous temperature analysis in 5.2, the indium detection phase as well as the Doppler cooling phase were further investigated. For the indium detection phase it was shown that the currently used saturation coefficients $s_{\mathrm{V}} = 0.5$ and $s_{\mathrm{H1}} \approx 0.3 s_{\mathrm{V}}$ of the ytterbium Doppler cooling beams V and H1 are too small to compensate the radial heating rate due to the 230 nm fluorescence on the indium detection transition. An optimal value of $s_{\mathrm{V}} \approx 0.8 \ldots 0.9$ depending on the trap axes orientation θ was found, for which the end temperatures of the indium detection phase could be reduced by $4 \ldots 8\%$. Due to the experimentally observed drop of the 230 nm fluorescence for $s_{\mathrm{V}} \gg 0.5$, further experiments are planned to investigate whether s_{V} can be further increased to ≈ 0.9.
Regarding the Doppler cooling phase, it was shown that for a fixed cooling time of $t_{\mathrm{cool}} = 50\,\mathrm{ms}$, the constant s phase can be completely neglected. The lowest temperatures are reached for $t_{\mathrm{cool}} = t_{\mathrm{ramp}} = 50\,\mathrm{ms}$, while keeping the cooling phase robust against high initial temperatures $T_{\mathrm{ini}} = T_{\mathrm{melt}}$. The optimization yields an improvement of the end temperatures of $\approx 4\%$ relative to the currently used $t_{\mathrm{const}\,s} = t_{\mathrm{ramp}} = 25\,\mathrm{ms}$. The analysis has also shown that a further decrease of the end temperatures on the order 10% is only possible for cooling times $\gg 100\,\mathrm{ms}$. Next, the cooling phase was optimized regarding the total cooling time. For axes orientations $\theta = \{30°, 60°\}$, t_{cool} could be reduced by $\approx 30 \ldots 40\%$ while obtaining comparable radial end temperatures as for the Doppler cooling phase used in the clock campaign. In case of a trap axis $\theta = 60°$, it is necessary to keep a short constant s phase of $t_{\mathrm{const}\,s} = 5\,\mathrm{ms}$ to cover a sufficient range of initial temperatures. For equal projections on both trap axes, $\theta = 45°$, the cooling phase could be reduced even further to $t_{\mathrm{cool}} = t_{\mathrm{ramp}} = 25\,\mathrm{ms}$.

The analysis of the exponential ramp has shown that the use of an exponential instead of a linear ramp could reduce the end temperatures further by $\approx 4\%$ for the proposed total cooling time of $t_{\mathrm{cool}} = 35\,\mathrm{ms}$. Here the $1/e$ time t_{exp} introduces a new parameter in the optimization. While these optimum $1/e$ times $t_{\mathrm{exp,opt}}$ are approximately the same for all investigated axis orientations θ in case of optimal initial temperatures, it is not possible to find a shared optimum for all angles in case of $T_{\mathrm{ini}} = T_{\mathrm{melt}}$. Here a compromise needs to be found between the two orientations $\theta = \{30°, 60°\}$. This trade-off can be avoided by using equal projections on both radial trap axes (i.e. $\theta = 45°$). For this orientation, the exponential saturation ramp leads to lower radial end temperatures compared to a linear ramp independent of the chosen initial temperatures.
In summary, the chapter has shown that the currently reached end temperatures are already close to the limit temperatures T_{lim} for $t_{\mathrm{cool}} \to \infty$. Therefore, the largest potential for possible optimizations is rather given by a reduction of the total Doppler cooling time, than a further reduction of the end temperatures.

6 Summary and outlook

In spring 2022, the $^{115}In^+$ clock at PTB attended an international clock campaign [16] for the first time. Its contribution to the campaign resulted in various new frequency ratios and an improvement of the only previously reported optical frequency ratio value $^{87}Sr/^{115}In^+$ [17]. For the uncertainty evaluation of these ratios, frequency shifts need to be thoroughly analyzed. This work presented the evaluation of the probe field induced ac-Stark of the indium clock, as well as a temperature analysis of the clock ion temperature throughout the spectroscopic sequence based on a theoretical model for sympathetic normal mode cooling.

The probe field induced ac-Stark shift results from the interaction of the probe field with the electric dipole operator. There are two contributions to the shift, the ellipticity induced shift as presented by Yudin et al. [18] and the ac-Stark shift by far off-resonant transitions.
The ellipticity induced shift is a yet unconsidered contribution in clocks based on the highly forbidden $^1S_0 \rightarrow {}^3P_0$ transition. It originates from experimental imperfections, namely an unwanted ellipticity of the probe field and a misorientation of the bias magnetic field described by the angular parameters ϵ and ξ. The analysis of the literature has shown that under typical conditions in atomic clock experiments, experimental imperfections can be estimated by $|\epsilon\xi|_{\text{est}} \approx 2 \times 10^{-3}$. Using this, a first estimate of the order of magnitude of the shift was determined for different clock species. The resulting shifts are in the low to mid 10^{-21} region and it was shown that $^{115}In^+$ is a favorable species, since it features an intrinsically low shift sensitivity. A further analysis of the experimental imperfections ϵ and ξ in the indium clock setup at PTB, which was based on clock spectroscopy of all relevant transitions, resulted in an upper bound of $|\epsilon\xi|_{\text{max}} \leq (2.7 \pm 1.9) \times 10^{-4}$. Using the results of the evaluated line scans, the ellipticity induced shift for the $^{115}In^+$ clock could be evaluated at a fractional value of $(0 \pm 4) \times 10^{-22}$. The evaluation of the transition scans showed the possibility that under the assumption of worst case frequency drifts, two relevant transitions could be shifted out of the covered scanning range throughout the process of acquiring the scans. The experiment could not be repeated throughout this thesis and a repetition is planned in the near future to verify the presented results.
The ac-Stark shift by far off-resonant transitions was evaluated in a theoretical analysis. Here the probe electric field strength was determined from the clock transition Rabi frequency present during clock interrogation and the respective dipole matrix element. A further analysis of various dipole matrix elements of far off-resonant transitions in $^{115}In^+$ allowed to determine the shift at a value of $(-2 \pm 5) \times 10^{-22}$. Using both contributions, the total probe field induced shift was determined to be $(-2 \pm 6) \times 10^{-22}$.
The analysis has shown that the probe field induced ac-Stark shift is a minor contribution to the total uncertainty of the indium clock. The written scripts for the evaluation of both contributions also allows an easy evaluation of the shift in future clock operation.

A major contribution to the uncertainty of the $^{115}In^+$ clock originates from the thermal time dilation shift which results from the residual thermal motion of the clock ion in the trapping potential. The motion also affects the instability of the clock via the temperature dependent loss of contrast and hence a reduction of the signal to noise ratio. To reduce the thermal influence on the clock performance, the $^{115}In^+$ ions are trapped in a linear mixed species Coulomb crystal together with $^{172}Yb^+$ which serve as the cooling species. Due to the coupled motion resulting from the Coulomb interaction, Doppler cooling of the ytterbium ions sympathetically cools the indium ions.
To gain a deeper understanding of the temperature dynamics throughout the whole spectroscopy sequence, a model for sympathetic mode cooling described by Keller et al. [21] was extended to fit the experimental conditions during the spring 2022 clock campaign. Using the model, the spectroscopy sequence and especially the Doppler cooling phase were extensively analyzed using

scripts written in Python. Without external disturbances such as collisions with background gas particles, the model predicts mode temperatures of all three principal trap axes $\leq 2.5\,\mathrm{mK}$ throughout the whole sequence and $< 0.8\,\mathrm{mK}$ during the clock interrogation. It also provides a lower bound of $\approx 0.7\,\mathrm{mK}$ for the temperature of the axial motion which could yet not be determined directly experimentally. Even the inclusion of cooling laser intensity and frequency fluctuations did not result in a temperature increase $> 5\%$ for all considered modes. The analysis also showed that the indium and ytterbium detection phases, which are necessary for state preparation and readout, contribute considerably to cooling and the robustness of the sequence against external heating sources. An interesting observation could be made for the radial and axial mode temperatures during the indium detection. The fluorescence of the indium ion resulted in axial mode temperatures $\ll T_{\mathrm{D,Yb}} \approx 0.47\,\mathrm{mK}$, while the radial modes were heated to $\approx 5T_{\mathrm{D,Yb}}$. Although the used model can not fully describe the cooling dynamics resulting from the narrow indium detection transition, by analyzing experimentally observed scattering rates, it was shown that axial temperatures on the order of $100\,\mu\mathrm{K}$ are plausible.
Possible improvements of the clock sequence were identified. The indium detection phase was optimized to reduce the effect of radial heating due to the indium fluorescence. Here optimal saturation parameters $s_{\mathrm{V}} = 0.8\ldots0.9$ and $s_{\mathrm{H1}} = 0.3s_{\mathrm{V}}$ of the ytterbium Doppler cooling beams V and H1 were found which minimize the radial mode temperatures during the detection. Whether these parameters can be applied in the experiment needs experimental verification. It was observed that the indium fluorescence drops for large cooling beam saturation parameters. This could be explained by a transition between indium and ytterbium cooling dominated axial temperature regimes. To verify this hypothesis, further experimental investigation is necessary. A first comparison with experimental data showed overall good agreement with the theoretically determined radial temperatures. To completely verify the results, additional experiments are planned.
Next, the Doppler cooling phase was optimized, which consists of two equally long sub-phases, one at constant cooling laser saturation followed by a phase where the saturation is linearly ramped to 0. It was shown that the currently reached radial and axial mode temperatures are within $8\ldots17\%$ of their respective theoretical temperature limits. A further temperature reduction would make total cooling times $\gg 100\,\mathrm{ms}$ necessary which are not sensible regarding the resulting decreased duty cycle. While keeping the currently used $50\,\mathrm{ms}$ total Doppler cooling time, the end temperatures could be decreased by $\approx 5\%$ by removing the constant s phase in favor of a longer saturation ramp.
To improve on duty cycle, the cooling phase was optimized regarding a decrease of the total cooling time. Here a reduction of $30\ldots40\%$ was possible by shifting cooling time from the constant s to the ramped s phase. The presented optimizations reached comparable end temperatures as for the currently used cooling settings while keeping the sequence robust against a broad range of initial temperatures. It was also shown that an equal projection of the vertical cooling beam V onto the two radial trap axes (instead of the currently assumed $30°/60°$) results in the best compromise between the respective end temperatures.
Also, the influence of a different ramp function was investigated. The linear ramp was compared to an exponential which introduced the corresponding $1/e$ time as new parameter in the optimization. It was shown that the exponential ramp can further reduce the end temperature of the Doppler cooling phase by $\approx 4\%$ compared to the proposed optimized phase under use of a linear ramp. On the other hand, the exponential ramp decreased the robustness against higher initial temperatures in case of unequal V projections onto the radial axes. The robustness could be increased by using equal projections. This, in combination with an exponential saturation ramp, could be a reasonable choice for future clock operation.
Overall, the theoretical temperature analysis allows a better understanding of the ion temperature dynamics throughout the clock spectroscopy sequence. The extension of the model for sympathetic mode cooling, its application to the experimental conditions during the spring 2022

clock campaign as well as its implementation in Python allows to easily simulate the impact of possible changes in the spectroscopy sequence. The presented optimizations should therefore be seen as the starting point for the theoretical analysis of future cooling routines.

References

[1] L. Essen and J. V. L. Parry. "An Atomic Standard of Frequency and Time Interval: A Cæsium Resonator". In: *Nature* 176.4476 (1955), pp. 280–282. ISSN: 1476-4687. URL: https://doi.org/10.1038/176280a0 (cit. on p. 1).

[2] S. M. Brewer et al. "$^{27}Al^{+}$ Quantum-Logic Clock with a Systematic Uncertainty below 10^{-18}". In: *PRL* 123.3 (2019), p. 033201. URL: https://link.aps.org/doi/10.1103/PhysRevLett.123.033201 (cit. on pp. 1, 29, 30).

[3] Tobias Bothwell et al. "JILA SrI optical lattice clock with uncertainty of 2.0×10^{-18}". In: *Metrologia* 56.6 (2019), p. 065004. ISSN: 1681-7575. URL: http://dx.doi.org/10.1088/1681-7575/ab4089 (cit. on pp. 1, 29, 30).

[4] W. F. McGrew et al. "Atomic clock performance enabling geodesy below the centimetre level". In: *Nature* 564.7734 (2018), pp. 87–90. ISSN: 1476-4687. URL: https://doi.org/10.1038/s41586-018-0738-2 (cit. on pp. 1, 29, 30).

[5] N. Huntemann et al. "Single-Ion Atomic Clock with 3×10^{-18} Systematic Uncertainty". In: *PRL* 116.6 (2016), p. 063001. URL: https://link.aps.org/doi/10.1103/PhysRevLett.116.063001 (cit. on p. 1).

[6] Tanja E. Mehlstäubler et al. "Atomic clocks for geodesy". In: *Reports on Progress in Physics* 81.6 (2018), p. 064401. ISSN: 1361-6633. URL: http://dx.doi.org/10.1088/1361-6633/aab409 (cit. on p. 1).

[7] M. S. Safronova et al. "Search for new physics with atoms and molecules". In: *RMP* 90.2 (2018), p. 025008. URL: https://link.aps.org/doi/10.1103/RevModPhys.90.025008 (cit. on p. 1).

[8] Andreas Bauch. "Caesium atomic clocks: function, performance and applications". In: *Measurement Science and Technology* 14.8 (2003), pp. 1159–1173. ISSN: 1361-6501. URL: http://dx.doi.org/10.1088/0957-0233/14/8/301 (cit. on p. 1).

[9] S. Weyers et al. "Advances in the accuracy, stability, and reliability of the PTB primary fountain clocks". In: *Metrologia* 55.6 (2018), pp. 789–805. ISSN: 1681-7575. URL: http://dx.doi.org/10.1088/1681-7575/aae008 (cit. on p. 1).

[10] NIST website, opended 25.09.2022. URL: https://www.nist.gov/si-redefinition/second-past (cit. on p. 1).

[11] Fritz Riehle. "Towards a Re-definition of the Second Based on Optical Atomic Clocks". In: (2015). URL: https://arxiv.org/abs/1501.02068 (cit. on p. 1).

[12] Fritz Riehle et al. "The CIPM list of recommended frequency standard values: guidelines and procedures". In: *Metrologia* 55.2 (2018), pp. 188–200. ISSN: 1681-7575. URL: http://dx.doi.org/10.1088/1681-7575/aaa302 (cit. on p. 1).

[13] Andrew D. Ludlow et al. "Optical atomic clocks". In: *RMP* 87.2 (2015), pp. 637–701. URL: https://link.aps.org/doi/10.1103/RevModPhys.87.637 (cit. on pp. 1, 3, 4).

[14] H. G. Dehmelt. "Monoion oscillator as potential ultimate laser frequency standard". In: *IEEE Transactions on Instrumentation and Measurement* IM-31.2 (1982), pp. 83–87. ISSN: 1557-9662. URL: https://ieeexplore.ieee.org/document/6312526 (cit. on p. 1).

[15] N. Herschbach et al. "Linear Paul trap design for an optical clock with Coulomb crystals". In: *Applied Physics B* 107.4 (2012), pp. 891–906. ISSN: 1432-0649. URL: https://doi.org/10.1007/s00340-011-4790-y (cit. on p. 1).

[16] European Metrology project 18SIB05 ROCIT: Robust optical clocks for international timescales. URL: http://empir.npl.co.uk/rocit/ (cit. on pp. 1, 85).

[17] Nozomi Ohtsubo et al. “Frequency ratio of an 115In+ ion clock and a 87Sr optical lattice clock”. In: *Opt. Lett.* 45.21 (2020), pp. 5950–5953. URL: http://opg.optica.org/ol/abstract.cfm?URI=ol-45-21-5950 (cit. on pp. 1, 85).

[18] V.I. Yudin et al. "Probe field ellipticity-induced shift in an atomic clock", submitted. 2022 (cit. on pp. 1, 21, 22, 24, 25, 28, 30, 31, 37, 44, 85).

[19] J. Keller et al. “Controlling systematic frequency uncertainties at the 10^{-19} level in linear Coulomb crystals”. In: *PRA* 99.1 (2019), p. 013405. URL: https://link.aps.org/doi/10.1103/PhysRevA.99.013405 (cit. on pp. 2, 4, 45, 47, 52).

[20] W. M. Itano et al. “Quantum projection noise: Population fluctuations in two-level systems”. In: *PRA* 47.5 (1993), pp. 3554–3570. URL: https://link.aps.org/doi/10.1103/PhysRevA.47.3554 (cit. on p. 3).

[21] J. Keller. “Spectroscopic characterization of ion motion for an optical clock based on Coulomb crystals”. PhD thesis. 2015. URL: https://www.repo.uni-hannover.de/handle/123456789/8541 (cit. on pp. 3, 7, 13, 15, 16, 85).

[22] C.J. Foot. *Atomic Physics*. Oxford Master Series in Physics. OUP Oxford, 2005. ISBN: 9780198506959. URL: https://books.google.de/books/about/Atomic_Physics.html?id=_CoSDAAAQBAJ&redir_esc=y (cit. on pp. 4, 5, 10, 11, 38, 68).

[23] I. Lizuain, J. G. Muga, and J. Eschner. “Motional frequency shifts of trapped ions in the Lamb-Dicke regime”. In: *PRA* 76.3 (2007), p. 033808. URL: https://link.aps.org/doi/10.1103/PhysRevA.76.033808 (cit. on p. 4).

[24] D. J. Berkeland et al. “Minimization of ion micromotion in a Paul trap”. In: *Journal of Applied Physics* 83.10 (1998), pp. 5025–5033. URL: https://doi.org/10.1063/1.367318 (cit. on p. 4).

[25] D. A. Steck. "Quantum and Atom Optics", (revision0.13.15, 28 July 2022). 2007. URL: https://atomoptics.uoregon.edu/~dsteck/teaching/ (cit. on pp. 5, 12, 21, 39–41, 55).

[26] S. Earnshaw. “On the Nature of the Molecular Forces which Regulate the Constitution of the Luminiferous Ether”. In: *Transactions of the Cambridge Philosophical Society* 7 (1848), p. 97. URL: https://ui.adsabs.harvard.edu/abs/1848TCaPS...7...97E (cit. on p. 6).

[27] W Jones. “Earnshaw’s theorem and the stability of matter”. In: *European Journal of Physics* 1.2 (1980), p. 85. URL: https://iopscience.iop.org/article/10.1088/0143-0807/1/2/004 (cit. on p. 6).

[28] M. Kretzschmar. “Particle motion in a Penning trap”. In: *European Journal of Physics* 12.5 (1991), pp. 240–246. ISSN: 1361-6404. URL: http://dx.doi.org/10.1088/0143-0807/12/5/010 (cit. on p. 6).

[29] Wolfgang Paul. “Electromagnetic traps for charged and neutral particles”. In: *RMP* 62.3 (1990), pp. 531–540. URL: https://link.aps.org/doi/10.1103/RevModPhys.62.531 (cit. on p. 6).

[30] F. G. Major, V. N. Gheorge, and G. Werth. *Charged Particle Traps*. Springer-Verlag, 2005. URL: https://doi.org/10.1007/b137836 (cit. on p. 7).

[31] D. Leibfried et al. “Quantum dynamics of single trapped ions”. In: *RMP* 75.1 (2003), pp. 281–324. URL: https://link.aps.org/doi/10.1103/RevModPhys.75.281 (cit. on pp. 7, 11, 13, 46, 47, 64).

[32] P. O. Schmidt et al. “Spectroscopy Using Quantum Logic”. In: *Science* 309.5735 (2005), pp. 749–752. URL: https://doi.org/10.1126/science.1114375 (cit. on p. 8).

[33] Colin D. Bruzewicz et al. "Trapped-ion quantum computing: Progress and challenges". In: *Applied Physics Reviews* 6.2 (2019), p. 021314. URL: https://doi.org/10.1063/1.5088164 (cit. on p. 8).

[34] Giovanna Morigi and H. Walther. "Two-species Coulomb chains for quantum information". In: *The European Physical Journal D* 13 (2001), pp. 261–269. URL: https://doi.org/10.1007/s100530170275 (cit. on pp. 8, 9).

[35] A. Steane. "The ion trap quantum information processor". In: *Applied Physics B: Lasers and Optics* 64.6 (1997), pp. 623–643. URL: https://doi.org/10.1007/s003400050225 (cit. on p. 8).

[36] R. H. Dicke. "The Effect of Collisions upon the Doppler Width of Spectral Lines". In: *PR* 89.2 (1953), pp. 472–473. URL: https://link.aps.org/doi/10.1103/PhysRev.89.472 (cit. on p. 13).

[37] R. Loudon. *The Quantum Theory of Light*. OUP Oxford, 1983. ISBN: 9780191589782. URL: https://books.google.de/books?id=AEkfajgqldoC (cit. on p. 13).

[38] Th. Becker et al. "High-resolution spectroscopy of a single In^+ ion: Progress towards an optical frequency standard". In: *Phys. Rev. A* 63 (5 2001), p. 051802. URL: https://link.aps.org/doi/10.1103/PhysRevA.63.051802 (cit. on pp. 15, 30, 32, 33, 35, 37, 40).

[39] R. H. Garstang. "Hyperfine Structure and Intercombination Line Intensities in the Spectra of Magnesium, Zinc, Cadmium, and Mercury*". In: *J. Opt. Soc. Am.* 52.8 (1962), pp. 845–851. URL: http://opg.optica.org/abstract.cfm?URI=josa-52-8-845 (cit. on p. 15).

[40] Warren Nagourney, Jon Sandberg, and Hans Dehmelt. "Shelved optical electron amplifier: Observation of quantum jumps". In: *PRL* 56.26 (1986), pp. 2797–2799. URL: https://link.aps.org/doi/10.1103/PhysRevLett.56.2797 (cit. on p. 16).

[41] T. Burgermeister. "Development and characterization of a linear ion trap for an improved optical clock performance". PhD thesis. 2019. URL: https://www.repo.uni-hannover.de/handle/123456789/5207 (cit. on p. 16).

[42] L. Schomburg. "Controlling mixed-species ion Coulomb crystals for optimal cooling and mitigating micromotion induced non-thermal heating". MA thesis. 2021. URL: https://www.quantummetrology.de/fileadmin/user_upload/Masterarbeit_Leon_Schomburg_3054480.pdf (cit. on pp. 16, 19, 58).

[43] H.N. Hausser. "Bereitstellung von UV-Laserlicht zur direkten Kühlung und Detektion von 115In+ in einer Multi-Ionen-Uhr". MA thesis. 2019. URL: https://www.quantummetrology.de/fileadmin/quest/multi_ion_clocks/Publications/2019_Masterarbeit_Hartmut_Nimrod_Hausser_upload_version.pdf (cit. on pp. 16, 17).

[44] T. Nordmann. In preparation. 2022 (cit. on pp. 16, 18, 54).

[45] T. Nordmann. PhD thesis, in preparation. 2022 (cit. on p. 16).

[46] Alexandre Didier et al. "946-nm Nd:YAG digital-locked laser at 1.1×10^{-16} in 1 s and transfer-locked to a cryogenic silicon cavity". In: *Opt. Lett.* 44.7 (2019), pp. 1781–1784. URL: http://opg.optica.org/ol/abstract.cfm?URI=ol-44-7-1781 (cit. on p. 17).

[47] D. G. Matei et al. "1.5 μm Lasers with Sub-10 mHz Linewidth". In: *PRL* 118.26 (2017), p. 263202. URL: https://link.aps.org/doi/10.1103/PhysRevLett.118.263202 (cit. on pp. 17, 34).

[48] L. Podlecki et al. "Radiation pressure on a two-level atom: an exact analytical approach". In: *J. Opt. Soc. Am. B* 35.1 (2018), pp. 127–132. URL: http://opg.optica.org/josab/abstract.cfm?URI=josab-35-1-127 (cit. on pp. 17, 47, 49, 50).

[49] T. Nordmann. Private communication. 2022 (cit. on pp. 17, 26, 35, 58).

[50] T. Nordmann. In preparation. 2022 (cit. on p. 19).

[51] R. Lange et al. "Coherent Suppression of Tensor Frequency Shifts through Magnetic Field Rotation". In: *PRL* 125.14 (2020), p. 143201. URL: https://link.aps.org/doi/10.1103/PhysRevLett.125.143201 (cit. on pp. 27, 29).

[52] T. R. Tan et al. "Suppressing Inhomogeneous Broadening in a Lutetium Multi-ion Optical Clock". In: *PRL* 123.6 (2019), p. 063201. URL: https://link.aps.org/doi/10.1103/PhysRevLett.123.063201 (cit. on pp. 27, 29).

[53] Nils Nemitz et al. "Modeling light shifts in optical lattice clocks". In: *PRA* 99.3 (2019), p. 033424. URL: https://link.aps.org/doi/10.1103/PhysRevA.99.033424 (cit. on p. 29).

[54] T. Rosenband et al. "Observation of the $^1S_0 \rightarrow {}^3P_0$ Clock Transition in $^{27}Al^+$". In: *Phys. Rev. Lett.* 98 (22 2007), p. 220801. URL: https://link.aps.org/doi/10.1103/PhysRevLett.98.220801 (cit. on p. 30).

[55] Ben-quan Lu et al. "Experimental Determination of the Landé g-Factors for $5s^2\ {}^1S$ and $5s5p\ {}^3P$ States of the ^{87}Sr Atom". In: *Chinese Physics Letters* 35.4 (2018), p. 043203. ISSN: 1741-3540. URL: http://dx.doi.org/10.1088/0256-307X/35/4/043203 (cit. on p. 30).

[56] Sergey G. Porsev, Andrei Derevianko, and E. N. Fortson. "Possibility of an optical clock using the $6^1S_0 \rightarrow 6^3P_0^o$ transition in ^{171,173}Yb atoms held in an optical lattice". In: *PRA* 69.2 (2004), p. 021403. URL: https://link.aps.org/doi/10.1103/PhysRevA.69.021403 (cit. on p. 30).

[57] Ekkehard Peik. "Laserspektroskopie an gespeicherten Indium-Ionen". PhD thesis. 1993. URL: https://www.mpq.mpg.de/4464435/mpq_reports (cit. on p. 41).

[58] W. Opęchowski. "Zur Theorie der verbotenen Quecksilberlinie 2655,8 Å (63P0-61S0)". In: *Zeitschrift für Physik* 109.7 (1938), pp. 485–490. ISSN: 0044-3328. URL: https://doi.org/10.1007/BF01340327 (cit. on p. 41).

[59] A. Kramida et al. NIST Atomic Spectra Database (ver. 5.9), [Online]. National Institute of Standards and Technology, Gaithersburg, MD. 2021. URL: https://physics.nist.gov/asd (cit. on pp. 41, 42).

[60] L. J. Curtis et al. "Predictive data-based exposition of $5s5p^{1,3}P_1$ lifetimes in the Cd isoelectronic sequence". In: *PRA* 62.5 (2000), p. 052513. URL: https://link.aps.org/doi/10.1103/PhysRevA.62.052513 (cit. on pp. 41, 42).

[61] H. Mineo et al. "Theoretical studies of high-harmonic generation based on the Keldysh-Faisal-Reiss theory". In: *Journal of Physics B: Atomic, Molecular and Optical Physics* 40.12 (2007), pp. 2435–2451. ISSN: 1361-6455. URL: http://dx.doi.org/10.1088/0953-4075/40/12/017 (cit. on p. 42).

[62] W. Ansbacher et al. "Cascade-corrected lifetime measurements for singly and doubly ionized indium". In: *Canadian Journal of Physics* 64.10 (1986), pp. 1365–1368. URL: https://cdnsciencepub.com/doi/10.1139/p86-242 (cit. on p. 42).

[63] Stig Stenholm. "The semiclassical theory of laser cooling". In: *RMP* 58.3 (1986), pp. 699–739. URL: https://link.aps.org/doi/10.1103/RevModPhys.58.699 (cit. on pp. 47, 56).

[64] D. Kalincev et al. "Motional heating of spatially extended ion crystals". In: *Quantum Science and Technology* 6.3 (2021), p. 034003. ISSN: 2058-9565. URL: http://dx.doi.org/10.1088/2058-9565/abee99 (cit. on p. 52).

[65] D. Kielpinski et al. "Sympathetic cooling of trapped ions for quantum logic". In: *PRA* 61.3 (2000), p. 032310. URL: https://link.aps.org/doi/10.1103/PhysRevA.61.032310 (cit. on p. 53).

[66] L Rüffert. Private communication (cit. on pp. 53, 60).

[67] E. Peik et al. "Sideband cooling of ions in radio-frequency traps". In: *PRA* 60.1 (1999), pp. 439–449. URL: https://link.aps.org/doi/10.1103/PhysRevA.60.439 (cit. on p. 64).

Danksagung

Zuerst möchte ich Prof. Dr. Tanja E. Mehlstäubler für die Möglichkeit danken, dass ich im Rahmen dieser Masterarbeit am Fortschritt der $^{115}In^{+}$ Uhr teilhaben durfte. Das gewonnene Wissen und die gesammelte Erfahrung werden auf meinem weiteren Weg in der Wissenschaft sicher von Vorteil sein. Zudem gilt mein Dank Prof. Dr. Piet O. Schmidt für die Übernahme des Korreferats.
Besonders danken möchte ich Dr. Jonas Keller und Nimrod H. Hausser für die Betreuung der Arbeit sowie den großen Spielraum, der mir bei der Ausarbeitung gelassen wurde. Der gesamten QUEST FG 2 danke ich für die Unterstützung während meiner Zeit an der PTB, wobei ich hier Tabea Nordmann für die zur Verfügung gestellten experimentellen Daten, sowie Luca Rüffert für die Ergebnisse seiner Schmelzpunktanalyse hervorheben möchte. Auch Dr. André P. Kulosa möchte ich danken, ohne den mein Weg wahrscheinlich nicht an die PTB geführt hätte.
Meinen Kommilitonen Mahir Ertürk und Jannik Hertzberg gilt besonderer Dank und Anerkennung für die Zusammenarbeit in den letzten fünf Jahren, ohne die ich das Studium nicht hätte bewältigen können. Hier sind wertvolle Freundschaften entstanden.
Zuletzt danke ich meiner Verlobten sowie meiner Familie für den Rückhalt und die uneingeschränkte Unterstützung.